



KU LEUVEN

Arenberg Doctoral School of Science, Engineering & Technology
Faculty of Engineering
Department of Mechanical Engineering

Large eddy simulation of high Reynolds number wall-bounded flows

Peng WU

Dissertation presented in partial fulfillment of the requirements for the degree of Doctor in Engineering

November 2012

Large eddy simulation of high Reynolds number wall-bounded flows

Peng WU

Jury:

Prof. dr. ir. P. Moldenaers, chair

Prof. dr. ir. J. Meyers, supervisor

Prof. dr. ir. M. Baelmans

Prof. dr. ir. W. Desmet

Prof. dr. ir. H. Deconinck

(von Karman Institute for Fluid Dynamics)

Prof. dr. ir. B. Merci

(Universiteit Gent)

Prof. Dr. P. Sagaut

(Université Pierre et Marie Curie - Paris 6)

Dissertation presented in partial fulfillment of the requirements for the degree of Doctor in Engineering

November 2012

© Katholieke Universiteit Leuven – Faculty of Engineering
Celestijnenlaan 300A box 2421, B-3001 Heverlee (Belgium)

Alle rechten voorbehouden. Niets uit deze uitgave mag worden vermenigvuldigd en/of openbaar gemaakt worden door middel van druk, fotocopie, microfilm, elektronisch of op welke andere wijze ook zonder voorafgaande schriftelijke toestemming van de uitgever.

All rights reserved. No part of the publication may be reproduced in any form by print, photoprint, microfilm or any other means without written permission from the publisher.

D/2012/7515/131
ISBN 978-94-6018-597-7

Preface

First and foremost, my deepest appreciation goes to my supervisor Prof. Johan Meyers who patiently taught, helped, and guided me on my research during these years. He is supportive, considerate and easy-going. His hard-working, critical and down-to-earth attitude to research has been always an inspiration and encouragement to me. I will never forget our countless discussions and the efforts he spent correcting papers, presentations, and the thesis which I have written. My future career will benefit a lot from this. I would have not accomplished my PhD's study without his immense and consistent support.

I am grateful to my co-advisor, Prof. Tine Baelmans, for her confidence in my potential and my work, and for giving me the opportunity to pursue my doctoral research in TME.

I would like to extend my deep gratitude to the members of the examination committee, for their comments, interesting questions, and for their valuable suggestions on this work.

I thank those colleagues and friends, including Sara Delpoort, Vladimir Jovanovic, Shijie Cao, Asim Onder, Jay Goit, Wim De Roeck, Leen Peeters and Kristof Van Dyck for their friendship and for their advice and help on both scientific and personal matters. I would like to sincerely thank the TME secretaries, Kathleen Coenen and Frieda Decoster, for all the help I have got from you during these years. Countless other friends have made the past few years absolutely delightful. Special thanks to ir. Joris Coddé, who helped me to prepare the Dutch abstract of this thesis. I would also like to acknowledge TME for providing financial support during my final year of PhD. Thanks to the ICTS (the central IT office) of KU Leuven for providing computing power on the VIC and VIC3 clusters for me to conduct all the computations.

At this moment, I would like to have a word for Prof. Yu-Xin Ren, who introduced me to the world of CFD many years ago. Thank you for opening up this wonderful horizon for me.

Thanks to my wife Yan XU for her constant support, encouragement and taking care of our little one Siqu. Finally, I wish to give my special thanks to my parents, for your consistent love, support and incredible time and efforts you have put into raising and shaping me. The thesis is dedicated to you.

Peng Wu
Heverlee, November 2012

Abstract

This PhD study aims to develop an efficient and accurate large-eddy simulation (LES) method for compressible high-Reynolds-number wall-bounded flows. This work started from an in-house research code FLOWAVE, a second-order code with the capability of LES. However, this code suffered from several major drawbacks preventing it becoming a well suited tool to deal with high-Reynolds-number wall bounded flows. This study seeks to address these problems and provide a pragmatic and robust LES methodology for high-Reynolds-number wall bounded flows.

Within the context of LES of high-Reynolds-number wall-bounded flows, the first challenge is the undesired odd-even decoupling which contaminates the flow field. In this study, to suppress the odd-even decoupling, conservative boundary filters are constructed without changing flow structures and flow properties such as mass flow rate and momentum. The filters are used in combination with conventional high-order selective filters at the inner points to provide an effective means to solve the odd-even decoupling. The importance of conservative filtering is also proved to be important for the sub-grid stress (SGS) models, in which explicit filters are involved. The conservative filters are tested over a couple of channel flow test cases and a 2D cavity case to study the influence the filtering on noise prediction, yielding superior results compared with conventional non-conservative filters.

The next challenge is the excessive computational cost due to the resolved LES of high-Reynolds-number wall-bounded flows. In wall-bounded turbulent flows, the length scale of the viscous sub-layer will decrease as Reynolds number increases. As a result, for resolved large eddy simulation, the number of grid points which are needed to resolve the wall layer will increase exponentially. Nevertheless, large Reynolds number wall-bounded flow tends to be the rule in most engineering flows. Therefore for those cases wall-resolved LES would lead to prohibitive computational cost and become impractical. Therefore, hybrid methods, for instance, wall-stress models (WSM) are usually employed

for attached wall flows to prescribe the shear stress at wall, so that the first grid point can be put far away from the wall to reduce the computational cost.

However, conventional hybrid methods, including the WSM when used in combination with a standard Smagorinsky model, are prone to the so-called ‘log-layer mismatch’ problem, resulting in poor predictions of the mean velocity and its gradient. Many attempts have been made to address this problem; however, they are limited by either their inability to suppress the log-layer mismatch to an accepted level, or their complexity and uncertainty in real practice.

In view of this, in this work, a theoretical framework was developed in which the relationship between the mean velocity gradient and the turbulent kinetic energy budgets in the log-layer is expressed. In this framework, different factors which may influence the mean shear can be quantified and analyzed. The analysis is then extended to the wall-modeled LES. It is shown that over-dissipation does not necessarily lead over-prediction of the mean shear. Based on this framework, a self-adaptive Smagorinsky model was proposed in which the Smagorinsky coefficient is dynamically adjusted so that the problem of log-layer mismatch is effectively suppressed. The model has been validated for a channel flow with rough walls at high Reynolds number, yielding desired velocity profile. The model is extended to include the viscous effect and applied to a couple of smooth channel flow cases. The log profiles of the mean velocity are more accurately captured compared with the conventional Smagorinsky model.

Finally, the wall-model LES methodology is applied to a square duct using the both the conventional Smagorinsky model and the new self-adaptive Smagorinsky model. A modified log-law is proposed to give a better fit with the experimental results compared with classic log law. The self-adaptive Smagorinsky model captures the acceleration near the corner, while the Smagorinsky model fails to capture such phenomenon. In addition, the errors on the friction velocity of the self-adaptive Smagorinsky model are lower than those of the Smagorinsky model, and the modified log law yields more accurate skin frictions compared with the classic log law.

Beknopte samenvatting

Dit doctoraat heeft als doel de ontwikkeling van een efficiënte en accurate Large-Eddy-Simulatie (LES) methode voor samendrukbare wandbegrensdde stromingen met hoog Reynoldsgetal. Het startpunt van dit werk was een in-house onderzoekscode FLOWAVE; een tweede-ordecode met LES mogelijkheden. Deze code had echter verschillende belangrijke nadelen, waardoor ze niet meteen gebruikt kon worden voor wandbegrensdde stromingen bij hoge Reynoldsgetalen. Dit onderzoek verhelpt deze problemen en voorziet een pragmatische en robuuste LES methodologie voor wandbegrensdde stromingen bij een hoog Reynoldsgetal.

In de context van LES van wandbegrensdde stromingen met hoog Reynoldsgetal, is een eerste uitdaging de ongewenste roosteroscillaties die het stromingsveld aantasten. Om deze roosteroscillaties te onderdrukken, worden in deze studie wandfilters geconstrueerd, die de stromingsstructuren en eigenschappen zoals massadebiet en momentum onveranderd laten. Deze filters worden gebruikt in combinatie met conventionele hoge-orde selectieve filters op interne roosterpunten en voorzien zo een effectieve methode om de roosteroscillaties te onderdrukken. Er wordt ook aangetoond dat conservatief filteren belangrijk is voor de *sub-grid stress* (SGS) modellen waarin expliciete filters toegepast worden. De conservatieve filters worden getest voor een aantal simulaties van een kanaalstroming en daarnaast ook voor een 2D caviteit waarin de invloed van het filteren op geluidsvoorspelling bestudeerd wordt. Voor beide tests leveren conservatieve filters superieure resultaten t.o.v. conventionele niet-conservatieve filters.

De volgende uitdaging is de excessieve rekenkost gerelateerd met LES van wandbegrensdde stromingen bij hoge Reynoldsgetalen. In wandbegrensdde stromingen verkleint de lengteschaal van de viskeuze sublaag wanneer het Reynoldsgetal stijgt. Dit heeft als gevolg voor LES dat het aantal roosterpunten exponentieel stijgt met het Reynoldsgetal, terwijl dit net het regime is dat vaak voor komt in de ingenieurspraktijk. Daarom worden hybride methodes toegepast voor wandbegrensdde stromingen, bv. *wall-stress models* (WSM), die

de schuifspanning aan de wand voorschrijven. Op die manier kan het eerste roosterpunt ver van de wand geplaatst worden end de rekentijd verlaagd worden.

Conventionele hybride methodes, inclusief het WSM in combinatie met een standaard Smagorinskymodel, zijn echter vatbaar voor het zogenaamde ‘log-layer mismatch’ probleem. Dit resulteert in gebrekkige voorspelling van de gemiddelde snelheid en zijn gradiënt. Veel pogingen zijn al ondernomen om dit op te lossen; zij zijn echter gelimiteerd ofwel door hun onvermogen om de ‘log-layer mismatch’ te reduceren tot een aanvaardbaar niveau ofwel door hun complexiteit en onzekerheid in de praktijk.

Vanuit dit oogpunt werd een theoretisch raamwerk ontwikkeld, waarin de relatie tussen gemiddelde snelheidsgradiënt en turbulente kinetische energie budgetten in de log-laag wordt uitgedrukt. In dit raamwerk kunnen de verschillende factoren die de gemiddelde afschuiving beïnvloeden gekwantificeerd en geanalyseerd worden. Deze analyse wordt daarna uitgebreid naar *wall-modeled* LES. Het wordt aangetoond dat overdissipatie niet noodzakelijk tot overschatting leidt van de gemiddelde afschuiving. Gebaseerd op dit raamwerk werd een adaptief Smagorinskymodel voorgesteld, waarin de Smagorinskycoëfficiënt dynamisch wordt aangepast zodanig dat het probleem van de ‘log-layer mismatch’ effectief onderdrukt wordt. Het model wordt gevalideerd voor de kanaalstroming met ruwe wanden en hoog Reynoldsgetal, waarbij het gewenste snelheidsprofiel werd bekomen. Het model werd uitgebreid om het viskeus effect mee op te nemen en toegepast op een aantal cases van gladde kanaalstroming. De logaritmische profielen van de gemiddelde snelheid worden nauwkeuriger weergegeven dan door het conventionele Smagorinskymodel.

Tenslotte wordt de LES methodologie voor wanden onderzocht voor een vierkant kanaal, gebruik makende van zowel het conventionele Smagorinskymodel als het nieuwe adaptieve Smagorinskymodel. Een gemodificeerde logaritmische wet wordt voorgesteld om een betere fit te geven met de experimentele resultaten, in vergelijking met de klassieke wet. Het adaptieve Smagorinskymodel slaagt erin om de acceleratie bij de hoeken van het kanaal weer te geven, terwijl het klassieke Smagorinskymodel faalt om dit fenomeen te voorspellen. Daarenboven is de fout op de wrijvingsnelheid van het adaptieve Smagorinskymodel kleiner dan deze van het klassieke Smagorinskymodel, en brengt de gemodificeerde logaritmische wet een nauwkeurigere wandwrijving in vergelijking met de klassieke logaritmische wet.

List of Symbols

Abbreviations

BC	Boundary condition
CAA	Computational aeroacoustics
CFD	Computational fluid dynamics
CFL	Courant-Friedrichs-Lewy condition
CV	Control volume
DES	Detached eddy simulation
DNC	Direct noise computation
DNS	Direct numerical simulation
FVM	Finite volume method
LES	Large eddy simulation
ODE	Ordinary differential equations
RANS	Reynolds-averaged Navier-Stokes
SGS	Sub-grid scale
TLM	Two-layer model
VMS	Variational multi-scale
WSM	Wall stress model

Arabic symbols

\hat{E}	Total energy
-----------	--------------

\hat{q}_j	Component of heat flux vector
\mathcal{G}	Low-pass filtering operator
\mathcal{H}'	High-pass filtering operator
\mathbf{u}	Velocity vector
C	Kolmogorov constant
c	Speed of sound
c_p	Specific heat at constant pressure
$C_{s,\infty}$	Lilly Smagorinsky coefficient, 0.17
C_s	Smagorinsky coefficient
E	Turbulent kinetic energy
$E(k)$	Energy spectrum
f	Frequency
$G(k)$	Transfer function of low-pass filter
G_D	Function of modified wavenumber for a second-order discretization
h_x, h_y, h_z	Grid spacing in coordinate directions x_1, x_2 and x_3 .
j_τ	j -th grid point away from the wall, the position where the velocity components are taken to feed the wall-stress model.
k	Thermal conductivity
k	Wave number
$K_{\mathcal{H}'}$	High-pass filter kernel
K_G	Low-pass filter kernel
l_s	Mixing length in the eddy-viscosity models
M	Mach number
P	Production of subgrid energy
p	Pressure
Pr	Prandtl number

Pr_t	Turbulent Prandtl number
Re	Reynolds number
Re_τ	Reynolds number based on friction velocity
S	Symmetric part of the strain tensor
St	Strouhal number
t	Time
U_∞	Free stream velocity
u_τ	Friction velocity ($\sqrt{\tau_w/\rho}$)
x_i	Cartesian direction
y	Wall-normal direction
y^+	Distance from the wall normalized by the viscous length scale, δ_ν
y_0	Surface roughness of rough-wall channels
u_i	Component of velocity vector in coordinate direction x_i

Greek symbols

β	The ratio of the width of high-pass filter \mathcal{G} and the width of low-pass filter \mathcal{H}' , for the VMS model
Δ	Filter width
δ	Boundary layer thickness
δ_ν	Viscous length scale (ν/u_τ)
δ_{ij}	Kronecker delta
ϵ_t	Dissipation of subgrid energy
γ	Specific heat ratio
γ_0	A parameter to account for the shape of low-pass filter
γ_β	A parameter to account for the shape of high-pass filter
$\hat{\sigma}_{ij}$	Stress tensor
κ	von Kármán constant

$\langle \cdot \rangle$	Ensemble average
ξ	Vector in physical space
μ	Dynamic viscosity
ν	Kinematic velocity
ν_t	Eddy viscosity of the residual motions
Ω	Computational domain
$\Omega_{i,j,k}$	The volume of the control volume (CV)
$\phi(y)$	Normalized mean-velocity gradient, $(y\kappa/u_\tau) d\langle u \rangle / dy$
ρ	Density
σ_{max}	Strength of the sponge zone
τ	Width of first-order time filter
τ_{ij}^a	Sub-grid stress tensor
τ_{ij}	The deviatoric part of the SGS stress tensor
$\tau_{M,w}$	The mean sub-grid scale stress at the wall
θ	Boundary layer momentum thickness

Miscellaneous symbols

$\overline{(\cdot)}$	Filtered value
ϕ	Flow variable in general
$\tilde{(\cdot)}$	Favre filtered value
$(\cdot)''$	Fluctuating value (Corresponds to Favre filtered value), $\phi'' = \tilde{\phi} - \bar{\phi}$
$(\cdot)'$	Fluctuating value, $\phi' = \phi - \bar{\phi}$
$(\cdot)_r$	Reference value which is used for normalization

Contents

Abstract	iii
Contents	xi
List of Figures	xv
List of Tables	xxi
1 Introduction	1
1.1 Controlling odd-even decoupling	2
1.2 LES for high-Reynolds-number wall flows	3
1.2.1 Wall-modeled large eddy simulation	5
1.2.2 The challenge for WSM and the log-layer mismatch	6
1.3 Aims and objectives	7
1.4 Outline	8
2 Numerical approach	11
2.1 The filtered compressible Navier-Stokes equations	11
2.2 Sub-grid scale (SGS) models	14
2.2.1 Momentum equation	14
2.2.2 Energy equation	19

2.3	Spatial and time discretization schemes	20
2.3.1	Face integration	21
2.3.2	Time integration	23
2.4	Boundary conditions	24
2.4.1	Classical boundary conditions	24
2.4.2	The wall stress model	24
2.4.3	The Sponge zone technique	26
3	Conservative filtering	27
3.1	Conservation properties	27
3.2	Self-adjoint filters	29
3.3	Construction of high-order conservative boundary filters	30
3.4	Numerical results	34
3.4.1	Channel flow	34
3.4.2	2D cavity flow	41
3.5	Conclusion	49
4	A new self-adaptive Smagorinsky model: a solution to the log-layer mismatch	51
4.1	Introduction	52
4.2	Analysis of turbulent kinetic energy budgets and relation to mean shear	52
4.2.1	Relation between energy budgets and mean velocity gradients in direct numerical simulation	53
4.2.2	Relation between energy budgets and mean velocity gradients in large-eddy simulation	54
4.2.3	Evaluation of terms contributing to the normalized mean-velocity gradient in conventional wall-modeled Smagorinsky LES	56

4.3	A self-adaptive Smagorinsky model for LES of high-Re boundary layer flows	59
4.3.1	Derivation of the self-adaptive model	60
4.3.2	Discretization of energy balance and self-adaptive model in internal points	62
4.3.3	Discretization issues at boundary points	63
4.4	Wall-modeled LES using self-adaptive Smagorinsky length scales	65
4.4.1	Experiment with self-adaptive model for full channel height	66
4.4.2	Use of self-adaptive model in the logarithmic region ($y < 0.12\delta$)	67
4.4.3	Further discussion on the use of the self-adaptive model	70
4.5	Extension of the self-adaptive model to include viscous effect .	74
4.5.1	A Preliminary study of the channel flow with $Re_\tau = 2000$	74
4.5.2	The channel flow with $Re_\tau = 950$	80
4.6	Conclusion	80
5	The application of wall-modeled LES: square duct flows	82
5.1	Introduction	82
5.2	Methodology and numerical setup	85
5.3	Results	88
5.4	Conclusion	90
6	Conclusion and suggestions for future research	95
6.1	Conclusion	95
6.2	Suggestions for future research	97
A	Coefficients of conservative boundary filters	99
	Bibliography	103

Curriculum vitae 113

List of Publications 115

List of Figures

2.1	Interpolation arrangement for 2D finite volume method. The primitive variables are interpolated to the cell interface $i + 1/2$ where the gradient tensor of the variables is calculated over a staggered control volume, and the fluxes are reconstructed. . .	22
3.1	Dissipation of the 11-point matching conservative filters and Berland <i>et al.</i> 's [2] 11-point boundary filters. (a) The dissipation of the conservative boundary filters, and (b)-(f) the comparison of the dissipation of the conservative filters and Berland <i>et al.</i> 's filters at the first five points from the wall. Solid line: Berland <i>et al.</i> 's boundary filters; dashed line: conservative boundary filters.	35
3.2	The dissipation of the 9-point (left) and 13-point (right) matching conservative boundary filters	36

- 3.3 Mean stream-wise velocities of the channel-flow testing. (a) Obtained by applying various conservative or non-conservative top-hat filters in the VMS model. (—): DNS reference data [35]; (—○): no-model simulation on the coarse mesh; (—◇): no-model simulation on the fine mesh; (—□): LES simulation on the coarse mesh with filtering applied in wall-parallel directions; (—·△): LES simulation on the coarse mesh with conservative filtering applied in three directions; (—▽): LES simulation on the coarse mesh with non-conservative filtering applied in three directions; (—): LES simulation on the fine mesh with conservative filtering applied in three directions. (b) Obtained by applying various high-order filters to remove odd-even decoupling. (—): DNS reference data; (···): LES simulation on the coarse mesh without spatial filtering; (—): LES simulation on the coarse mesh with Berland *et al.*'s filters [2]; (—·◇): LES simulation on the coarse mesh with conservative filters; (···□): LES simulation on the fine mesh without spatial filtering; (—△): LES simulation on the fine mesh with Berland *et al.*'s filters; (—·): LES simulation on the fine mesh with conservative filters. 37
- 3.4 Second-order turbulent statistics obtained by applying various conservative or non-conservative top-hat filters in the VMS model: (a) $\langle u'u' \rangle^+$, (b) $\langle u'v' \rangle^+$, (c) $\langle v'v' \rangle^+$ and (d) $\langle w'w' \rangle^+$. (—): DNS reference data [35]; (—○): no-model simulation on the coarse mesh; (—□): LES simulation on the coarse mesh with filtering applied in wall-parallel directions; (—·△): LES simulation on the coarse mesh with conservative filtering applied in three directions; (—▽): LES simulation on the coarse mesh with non-conservative filtering applied in three directions; (—): LES simulation on the fine mesh with conservative filtering applied in three directions. 38
- 3.5 Second-order turbulent statistics obtained by applying various high-order filters to remove odd-even decoupling: (a) $\langle u'u' \rangle^+$, (b) $\langle u'v' \rangle^+$, (c) $\langle v'v' \rangle^+$ and (d) $\langle w'w' \rangle^+$. (—): DNS reference data; (···): LES simulation on the coarse mesh without spatial filtering; (—): LES simulation on the coarse mesh with Berland *et al.*'s filters [2]; (—·◇): LES simulation on the coarse mesh with conservative filters; (···□): LES simulation on the fine mesh without spatial filtering; (—△): LES simulation on the fine mesh with Berland *et al.*'s filters; (—·): LES simulation on the fine mesh with conservative filters. 39
- 3.6 Cavity configuration 42

- 3.7 Vorticity fields during one cycle of oscillation (first Rossiter mode) obtained by the 11-point conservative filters (left) and non-conservative filters (right) on the fine mesh. 44
- 3.8 Pressure contours during one cycle of oscillation (first Rossiter mode) obtained by the 11-point conservative filters (left) and non-conservative filters (right) on the fine mesh. 45
- 3.9 Time averaged streamlines on the fine mesh by the conservative filters (left) and Berland *et al.*'s filters (right). 46
- 3.10 Mean pressure coefficient along the cavity bottom wall obtained by (—): the fine mesh and conservative filters, (— □): the fine mesh and Berland *et al.*'s filters, (— ○): the coarse mesh and conservative filters, (— □): the coarse mesh and Berland *et al.*'s filters. 47
- 3.11 Power spectral density of fluctuating pressure versus the Strouhal number $St = fL/U_\infty$ at the position $(0.2D, 10D)$ by: fine mesh with conservative filters (a); fine mesh with Berland *et al.*'s filters (b); coarse mesh with conservative filters (c); coarse mesh with Berland *et al.*'s filters (d). 48
- 3.12 Mean velocity profile of the incoming boundary layer in a semi-logarithmic scale plot against the distance from the wall, obtained by the fine mesh and conservative filters (Δ), the fine mesh and Berland *et al.*'s filters (∇), the coarse mesh and conservative filters (—), the coarse mesh and Berland *et al.*'s filters (—). 49
- 4.1 The contributions to $\phi(y)$ according to Eq. (4.8) in DNS of full developed turbulent channel (database by Hoyas and Jiménez [30]), in inner scaling (left) and outer scaling (right). Symbols, (\circ): $Re_\tau = 2003$, (\diamond): $Re_\tau = 950$, (Δ): $Re_\tau = 550$. Lines, (—, black): $\phi(y)$. Further, all multiplied with $y\kappa/[u_\tau(u_\tau^2 - fy)]$, (— · —, blue): mean-flow viscous dissipation; (— · · —, green): total dissipation (mean-flow + turbulent); (— —, red): transport terms. 55

4.2 Mean velocity (left), and terms contributing to $\bar{\phi}(y)$ (right) for the standard Smagorinsky model with Mason & Thomson’s damping[54] near the wall. Symbols, (o): $C_s = 0.10$; (\square): $C_s = 0.166$. Lines in right figure, (—, black): $\bar{\phi}(y)$. Further, all multiplied with $y\kappa/[u_\tau(u_\tau^2 - fy)]$, (— · —, blue): mean-flow subgrid-model dissipation; (— · · —, green) sum of all subgrid contributions (dissipation + transport), (— —, red): resolved turbulent transport. 58

4.3 The mean velocity (left) and budgets for $\phi(y)$ (right) using the VMS model and the standard Smagorinsky model with $C_s = 0.11$ respectively. 59

4.4 Mean velocity (a), normalized velocity gradient (b), and Smagorinsky coefficient C_s (c) obtained from a RANS-like simulation (\square), and a large-eddy simulation (Δ), using l_s determined with a log profile up to the center. Both simulations use a $64 \times 36 \times 64$ mesh. 67

4.5 Stream-wise velocity profile in a semi-logarithmic scale (a), and normalized mean-velocity gradient $\phi(y) = (y\kappa/u_\tau)(d\langle u \rangle/dy)$ (b) for simulations with a self-adaptive model applied up to 12% of the channel height. Four cases are compared: $96 \times 54 \times 96$ (\square , and solid line), $96 \times 72 \times 64$ (Δ , and dotted line), $128 \times 96 \times 128$ (∇ , and dash-dot-dot line) and $192 \times 108 \times 192$ (\diamond , and dashed line). 69

4.6 Averaged Smagorinsky coefficient (a) and length scale l_s (b) from the simulations with the self-adaptive model applied up to 12% of the channel height. Four cases are compared: $96 \times 54 \times 96$ (solid line), $96 \times 72 \times 92$ (dotted line), $128 \times 96 \times 128$ (dash-dot-dot line) and $192 \times 108 \times 192$ (dashed line). 70

4.7 Normal Reynolds stresses $\langle u'u' \rangle/u_\tau^2$ (a), $\langle v'v' \rangle/u_\tau^2$ (b), and $\langle w'w' \rangle/u_\tau^2$ (c), from simulations with self-adaptive model applied up to 12% of the channel height, and comparison to conventional Smagorinsky result. Self-adaptive cases: $96 \times 54 \times 96$ (solid line), $96 \times 72 \times 92$ (dotted line), $128 \times 96 \times 128$ (dash-dot-dot line) and $192 \times 108 \times 192$ (dashed line). Conventional Smagorinsky model using $C_s = 0.17$, cf. Section 4.2.3 (\square —). 71

- 4.8 Stream-wise velocity profile in a semi-logarithmic scale (a), and normalized mean-velocity gradient $\phi(y) = (y\kappa/u_\tau)(d\langle u \rangle/dy)$ (b), for simulations with a self-adaptive model up to 30% of the channel height. Five cases are compared: $64 \times 48 \times 64$ (\square , and solid line), $128 \times 72 \times 128$ (Δ , and dotted line), $128 \times 96 \times 128$ (∇ , and dash-dot-dot line) and $192 \times 108 \times 192$ (\diamond , and dashed line). 72
- 4.9 The averaged Smagorinsky coefficient (a) and normal Reynolds stress component $\langle u'u' \rangle / u_\tau^2$ (b) from the simulations with the self-adaptive model applied up to 30% of the channel height. Four cases are compared: $64 \times 48 \times 64$ (solid line), $128 \times 72 \times 128$ (dotted line), $128 \times 96 \times 128$ (dash-dot-dot line) and $192 \times 108 \times 192$ (dash line). 73
- 4.10 The predicted normalized mean velocities ($Re_\tau = 2000$) in comparison with DNS results [30] and logarithmic profile (classic log law) with logarithmic x-axis representing y^+ . The factors which influence the prediction of normalized mean velocities are investigated and can be found respectively in: (a) the viscous terms, (b) the transport terms, (c) j_τ , the positions where the velocities are taken to computed wall stress and (d) the value of $\phi(y)$ 76
- 4.11 Normalized mean velocity gradient $\phi(y)$, calculated from the DNS data [30]. The read line indicates the empirical fit of $\phi(y)$, see Eq. (4.44). 78
- 4.12 The predicted normalized mean velocities ($Re_\tau = 2000$ and $Re_\tau = 950$) using conventional Smagorinsky model and self-adaptive model with Smagorinsky coefficient 0.17 and 0.25 respectively, in comparison with DNS results [30] and logarithmic profile (classic log law) with (a) $Re_\tau = 2000$ plotted against a logarithmic x-axis representing y^+ , (b) $Re_\tau = 2000$ plotted against a non-logarithmic x-axis, (c) $Re_\tau = 950$ plotted against a logarithmic x-axis representing y^+ and (d) $Re_\tau = 950$ plotted against a non-logarithmic x-axis. 79
- 5.1 The experimental mean velocities along wall bisector, normalized using bulk velocity, at Reynolds numbers respectively (a) 83000 [7] and (b) 250000 [22]. The theoretical velocity profiles calculated from classical log law and modified log law are plotted as references. 86

5.2	The numerical setup for the calculation of square duct flows using the self-adaptive model.	87
5.3	The predicted mean velocities based on the classical log law and normalized using bulk velocities, in comparison with experimental results [22] (a) along the wall bisector, and (b) along the corner bisector.	88
5.4	The predicted mean velocity contours based on the classical log law and normalized using bulk velocities, in comparison with experimental results (dash-dot lines) [22], using (a) Smagorinsky model, and (b) self-adaptive model.	89
5.5	The predicted mean velocities based on the modified log law and normalized using bulk velocities, in comparison with experimental results [22] (a) along the wall bisector, and (b) along the corner bisector.	90
5.6	The predicted mean velocity contours based on the modified log law and normalized using bulk velocities, in comparison with experimental results (dash-dot lines) [22], using (a) Smagorinsky model, and (b) self-adaptive model.	91
5.7	Mean secondary velocity vectors (a) obtained using the self-adaptive model in combination with the modified log law (b) the DNS results from Gavrilakis [18].	92
5.8	Reynolds stresses (a) $\langle u'u' \rangle$, (b) $\langle v'v' \rangle$, and (c) $-\langle u'v' \rangle$, from simulations obtained by: log law combined with Smagorinsky model ($-\square$), modified log law combined with self-adaptive model ($-\diamond$), log law combined with Smagorinsky model ($-\circ$) and modified log law combined with self-adaptive model ($-\triangle$). The experimental results are taken from reference [22], indicated by bold lines.	93

List of Tables

3.1	The constraints imposed in each boundary point of the 11-point matching conservative boundary filter	33
3.2	Overview of channel flow test cases used to test the filtering of the VMS model	36
3.3	Channel-flow cases used to test the use of spatial filters for removal of odd-even decoupling	40
3.4	Errors induced by use of conservative, and Berland <i>et al.</i> 's filters on stretched grids	40
4.1	Different cases for the testing of the self-adaptive model up to $y/\delta = 0.12$. All cases use equidistant meshes on a domain of $2\pi \times 1 \times \pi$, with wall roughness $y_0 = 10^{-4}\delta$	68
4.2	Different cases for the testing of the self-adaptive model up to $y/\delta = 0.3$. All cases use equidistant meshes on a domain of $2\pi \times 1 \times \pi$, with wall roughness $y_0 = 10^{-4}\delta$	72
4.3	Overview of channel flow test cases used to test the factors which influence the prediction of log velocity profile	77
4.4	Overview of channel flow test cases with $Re_\tau = 950$	80
5.1	Overview of some of previous studies on duct flows	84
5.2	Overview of square duct flow test cases of $Re_b = 250000$	87
A.1	The 9-point [3], 11-point [2] and 13-point [3] spatial filters for internal points, $g_{-j} = g_j$	99

A.2	The coefficients of the 9-point matching conservative boundary filters	99
A.3	The coefficients of the 11-point matching conservative boundary filters	100
A.4	The coefficients of the 13-point matching conservative boundary filters	101

Chapter 1

Introduction

This study was initiated under the frame of the SBO CAPRICON project (funded by IWT, Agency for Innovation by Science and Technology, Belgium) which is dedicated to computational aeroacoustics (CAA). One part of the project aimed at providing accurate sources using large eddy simulations for sound propagation emitted from a confined flow in hybrid CAA simulations. As part of this, a square muffler was built and tested to provide a reference for numerical simulations [86]. Both the flow field and acoustic field are measured. The Mach number is 0.1 and the Reynolds number based on the centerline velocity is around 1.7×10^5 . This flow regime falls in both the low-Mach-number and high-Reynolds-number flow categories.

Large eddy simulation (LES) was chosen as the tool to simulate the confined flow field in the square muffler to provide accurate sound sources. Before the LES technique can be applied to CAA problems, it is a prerequisite that the tool itself must be reliable and trustworthy. Therefore, we faced a major challenge in this study, which is to develop a robust and pragmatic tool for large eddy simulation of high-Reynolds-number wall bounded flows, and this is the main aim of this PhD research. Within this context, this work was started from FLOWAVE [73], a second-order finite-volume research code combined with the 4th-order explicit Runge-Kutta time scheme and LES capabilities. Though this is a good starting point for the aforementioned purpose, it suffered from several major drawbacks which need to be addressed.

The first is its lack of capability to deal with odd-even decoupling, which is a common problem in the numerical simulations of low-Mach-number compressible flows. The code employs a central second-order spatial discretization scheme which is known to be susceptible to odd-even decoupling (or so-called π -

modes) [48, 82]. This phenomenon is not physical, and may lead to unrealistic solutions or divergence of the simulations. Moreover, for CAA applications, the sound sources rely on the quality of the numerical solutions in the source region. The odd-even decoupling may contaminate the source region, therefore is not desirable.

Another major challenge is the excessive computational cost due to wall-resolved LES of high-Reynolds-number confined flows. As will be explained in section 1.2, the number of grid points which are needed to resolve the wall increases exponentially with the Reynolds number. Besides that, since only explicit Runge-Kutta time stepping method is implemented in FLOWAVE, the time step is constrained by the smallest cell in the computational domain and further by the low Mach number. Thus the wall-resolved LES is impractical for the flow regime which we are concerned about.

In the next sections, the current work is firstly situated in the state of art of large eddy simulations, with a focus on the techniques on removing odd-even decoupling and wall-model LES, in particular, the wall-stress model (WSM) and the so called ‘log-layer mismatch’ phenomenon. This phenomenon is a long-persisting problem for the wall-modeled LES, which leads to a wrong representation of the mean velocity profile near the wall. It will be further elaborated in section 1.2. Finally the aims and objectives are specified, followed by the outline of the thesis.

1.1 Controlling odd-even decoupling

The problem of odd-even decoupling is frequently encountered in simulations in which central finite difference schemes or their finite volume equivalents are employed. The spurious odd-even decoupling often leads to numerical instability and thus should be suppressed. The earliest effort to remove odd-even decoupling dates back to 1981 [36], where artificial dissipative terms were explicitly added to the governing equations. These terms are a blend of second-order and fourth-order terms with coefficients depending on the local pressure gradient. Visbal et al. [88] chose an alternative way and developed a 10th-order non-dispersive spatial filter, which has been shown to be superior to the added artificial dissipation in terms of both stability and accuracy on stretched curvilinear meshes. Other studies on eliminating odd-even decoupling through filtering can be found in [83, 81, 3, 2].

In order to efficiently remove odd-even decoupling with spatial filters, much attention is paid to local accuracy properties of these filters. In particular, it is important that the π -modes, which occur as oscillations at the smallest

resolvable scales on the grid, are removed without affecting large-scale noise and flow features. Tam et al. [83] proposed the artificial selective damping in a computation scheme which can effectively eliminate all spurious short waves in the numerical solution. Bogey and Bailly [3] further constructed selective filters accurate for waves down to four points per wavelength which are optimized by minimizing the numerical errors for the same range of wavenumbers. The corresponding non-centered boundary selective filters are then developed in a similar way [2].

Nevertheless not much attention has been paid to the global conservation properties of these high-order filters up till now. In the presence of non-periodic boundary conditions, and near wall boundaries, this may lead to incorrect flow predictions. From a theoretical point of view, Vreman [90] showed that a normalized filter is globally conservative if the filter is self-adjoint, requiring a filter operator which is symmetric in its arguments. In the current work, starting from theoretical study by Vreman, a set of high-order globally conservative filters are proposed to solve this issue.

In addition to the spatial filters which are used to suppress odd-even decoupling, attention also needs to be paid to the global conservation properties of the explicit filtering, which is often used in LES for the formulation of LES subgrid-scale models. One class of models, which have become popular recently, are the variational multi-scale (VMS) Smagorinsky models first introduced by Hughes *et al.* [33, 31]. These models explicitly employ high-pass filters, which restrict the models effect to small resolved scales, where turbulent energy needs to be removed from the flow. In recent years, development and testing of VMS models often relied on simple test cases such as channel flows with two homogeneous directions parallel to the walls, and filtering was only performed along wall-parallel directions [33, 89, 37, 60, 79]. For general applicability, the SGS model and associated high-pass filter should be fully three-dimensional in space. Stolz [79] was among the first to try a VMS Smagorinsky model in a channel flow simulation using three-dimensional high-pass filtering, hence including filtering in the wall normal direction. He constructed a high-pass filter by using a low-pass top-hat filter, subtracting it from the identity operator, but found errors of more than 30% on the flow predictions. At the time, Stolz [79] argued that higher-order filters are needed to guarantee accurate results.

1.2 LES for high-Reynolds-number wall flows

In recent years, with ever increasing computing power, LES becomes a more and more popular approach for turbulence modeling. In LES, the large

energy-containing motions are resolved while the smaller eddies are modeled, thus provides a better representation of turbulent flow field compared with the Reynolds-averaged Navier–Stokes (RANS) method, for which the whole turbulent field is modeled. Compared with DNS in which the turbulent flow field is fully resolved, down to the so-called Kolmogorov scale where the viscous dissipation happens, the LES is less computationally demanding. In reality, large Reynolds number wall-bounded flow tends to be the rule in most situations. For instance, the Reynolds number for the flow of air around a car is typically a few millions, while in atmospheric boundary layers, the Reynolds number is even several orders higher than this. For these situations, the boundary layer accounts for merely a tiny part of the flow domain, however, to properly resolve the boundary layer, adequate grid points should be placed in the boundary layer, typically 10-20 [28]. This not only results in a dramatic increase of the overall number of grid point, but also severely constrains the size of time step, leading to prohibitive computational costs. The excessive computational cost to resolve the boundary layer has been, and will continue to be a major challenge for LES of very high-Reynolds-number wall-bounded flows.

Cost estimation for wall-resolved LES can be found in various studies [11, 67]. They are based on the consideration that the integral length scales must be properly resolved in the LES. In the outer layer, the integral length scale is proportional to the size of the large eddies which is only weakly dependent on the Reynolds number. It was estimated that the resolution required for the outer layer for a boundary layer is proportional to $Re^{0.4}$, while for the wall layer (which in high-Reynolds-number applications accounts for only a tiny portion of the boundary layer) the Re-dependence of the resolution is much stronger. As the Reynolds number increases, the physical dimensions of near wall eddies decrease much more rapidly than the boundary layer thickness, resulting in more stringent resolution requirements. Chapman estimated the number of grid points needed to resolve the inner layer scales as $Re^{1.8}$ [11]. This makes application of LES to high-Reynolds-number flows impractical.

Moreover, the characteristics and objectives of CAA problems are significantly different from those commonly encountered in CFD [15]. One of most notable differences between aerodynamic and aeroacoustic phenomena is the disparity of the magnitudes of acoustic and aerodynamic perturbations. Acoustic motion generally occurs at a much smaller order of magnitude than the aerodynamic or turbulent motion. This disparity is more pronounced for lower Mach numbers and presents a severe challenge to direct CAA techniques. As a result, special care is needed to make sure that the numerical error is much smaller than the magnitude of the acoustic waves to avoid that the acoustic solution may be totally corrupted by computational noise and error. CAA methodologies should thus have a high-order of accuracy, which leads to higher computational cost.

1.2.1 Wall-modeled large eddy simulation

As previously mentioned, in high-Reynolds-number turbulent boundary layers, the ratio of turbulent length scales in the outer layer to length scales in the inner layer is very large, requiring excessively fine grids if inner-layer dynamics are to be correctly represented in wall-resolved LES. For smooth walls, the ratio of the boundary layer thickness δ to the viscous length scale δ_ν , corresponds with $Re_\tau \equiv u_\tau \delta / \nu$ (with u_τ the friction velocity, and ν the kinematic viscosity), illustrating the unfavorable scaling with Reynolds number.

This limitation was recognized from the earliest applications of LES, and various attempts have been made to bypass the inner layer and model its effects in a global sense. This spurs the development of models for the wall layer, also known as approximate boundary-conditions or wall-layer models. In the following, a review of the various approaches is carried out. This is followed by a more detailed review of the previous studies on the WSM and the challenges in WSM as well as the problem of log-layer mismatch.

The commonly used wall layer models can be summarized into three categories, which from easy to hard in terms of implementation, are, respectively: WSM, Zonal approaches and the hybrid RANS/LES methods.

- Wall-stress model (WSM)

To avoid the use of fine grids near the wall in high-Reynolds number LES, the near wall flow behavior is often represented with a wall-stress model (sometimes referred to as equilibrium-stress models as well), which relies on inner-layer similarity theory. In that case, the no-slip boundary condition used in a wall-resolved LES, is replaced by a wall-stress model in the first grid cell near the wall. This approach allows the first grid point to be located in the logarithmic layer ($y^+ > 40$) thus avoids the stringent resolution requirement of wall-resolved LES ($y^+ < 1$). Moreover, since the vortical structures in the viscous and buffer regions don't have to be resolved, it permits to use coarser meshes in other directions as well: $\Delta x \cong 100 \sim 600$, $\Delta z \cong 100 \sim 300$.

- Zonal approaches

Zonal approaches are based on the explicit solution of a different set of equations in the inner layer. The two-layer model (TLM) which was firstly proposed by Balaras and Benocci is the most representative one [1]. TLM solved the two-dimensional turbulent boundary-layer equations on an embedded grid between the first grid point and the wall. This approach is applied to rotating channel flow and flow in a square duct, and obtained improved agreement with the experimental data, compared

with the basic WSM. Cabot [8, 9] studied the performance of the WSM and TLM in plane channel flow and a backward-facing step, found that the basic WSM is sufficient for the plane channel flow, however fails for the backward-facing step where mass separation occurs.

- Hybrid RANS/LES methods

Recent development of wall layer models has centered on the hybrid methods, in which the RANS equations are solved in the inner layer, while the LES are employed away from the wall. The detached eddy simulation (DES) is most widely used hybrid approach. It was introduced by Spalart et al. [78] as a method to compute massively separated flows, which combines the solution of the RANS equations in the attached boundary layers with LES in the separated regions. A more comprehensive review on the hybrid RANS/LES methods can be found in [63].

1.2.2 The challenge for WSM and the log-layer mismatch

The problem of ‘log-layer mismatch’, characterized by an over-prediction of the normalized mean-velocity gradient in the inner layer which reaches levels of over 100%, has been a long-persistent problem for wall-modeled large eddy simulation. The problem is present for all the aforementioned approaches and was reported in numerous studies, for instance [68, 62, 64, 70, 6, 26]. In this study, the focus is on addressing the ‘log-layer mismatch’ in the wall-stress model. The combination of a wall-stress model in LES with conventional subgrid-scale models leads to the problem of ‘log-layer mismatch’, and this is particularly the case when a Smagorinsky model is used. Near the wall, in the inner layer, and up to roughly 20% of the boundary layer thickness, a logarithmic velocity profile is expected when the distance to the wall expressed in inner layer units exceeds $y^+ = 30$. In that case, the normalized mean-velocity gradient

$$\phi(y) \equiv \frac{y\kappa}{u_\tau} \frac{d\langle u \rangle}{dy} = 1, \quad (1.1)$$

with κ the von Kármán constant, y the wall-normal direction, and $\langle u \rangle$ the mean stream-wise velocity. However, when ‘log-layer mismatch’ happens, the value of $\phi(y)$ is higher than unity.

To solve this issue for rough-wall simulations, Mason and Thomson [54] proposed to use a simple algebraic damping of the Smagorinsky coefficient close to the wall, blending it to the expected near-wall RANS behavior of the eddy viscosity. This greatly improves the LES prediction when the blending parameters are properly tuned [56], but it does not fully resolve the issue of the overshoot of the normalized mean-velocity gradient. For smooth walls, similar damping functions

for the Smagorinsky coefficient are based on a Van-Driest-like damping (cf, e.g. Cabot [10] and Piomelli [65] for details).

Also when a dynamic Smagorinsky model is used, adaptations near the wall are required. Porte-Agel *et al.* [68] improved the standard dynamic Smagorinsky model by using a second test-filter level, such that the dependence of the Smagorinsky coefficient on the ratio of filter width to integral length scale close to the wall is better accounted for. Later this approach was reformulated into a Lagrangian framework by Bou-Zeid *et al.* [4]. Nevertheless, even in this double-filter dynamic procedure, overshoots of the normalized mean-velocity gradient in the order of 10% are observed [68]. Many other attempts have focussed on high-Reynolds-number near-wall modeling, often also aiming at more complex flow simulations. Templeton *et al.* [84] used tabulated eddy viscosity values of precursor wall-resolved LES to deduct the required eddy viscosity in wall-modeled simulations. Also in other approaches, such as DES, the issue of the log-layer mismatch in the simplest case of a high-Reynolds number boundary layer on a flat plate remains unresolved [77].

A challenge in the modeling of near-wall features on LES grids (which are only coarsely resolved with respect to inner-layer dynamics), is that numerical discretization errors often interfere with physical modeling attempts [10]. In a very involved approach, Templeton *et al.* [85] solved this by using optimal feed-back control for the near-wall closure, using a cost functional that measures the deviation from the mean-velocity profile from the target logarithmic profile. In recent work, Brasseur and Wei [5] tried to gain more insights into the complex interaction of errors near the wall for the standard Smagorinsky model, by systematically mapping the influence of the grid-stretching ratio, grid density, and the Smagorinsky coefficient on the overshoot of the velocity gradient. They defined a ‘high-accuracy’ zone in which the combination of the aforementioned elements effectively decrease the overshoot of the mean shear at the first grid point, but this improved gradient was at the cost of large errors on the predicted von Kármán constant.

1.3 Aims and objectives

As mentioned early in this chapter, it is impractical to conduct a wall-resolved LES of the square muffler. In this study, a pragmatic methodology was envisaged for the confined muffler flows: in the inlet and tail square ducts where the flow are almost attached, the WSM will be employed to circumvent the excessive computational cost of the wall-resolved LES; the expansion chamber, on the other hand, will be fully resolved, considering the mass separation and the fact

that the local Reynolds number is likely to be much lower than that in the ducts. However, the conventional WSM suffers from the ‘log-layer mismatch problem’ and are unable to capture the correct mean velocity profile near the wall. Therefore, the current study will firstly aim to improve the prediction of mean velocity for the WSM and validate the improved model over channel flows. The improved wall-modeled LES will be then applied to square duct flows and the results will be compared with existing experimental results. In this setup, the simulation of the flows in the ducts has considerable influence on the overall prediction of the turbulent flow field in the muffler and even the acoustic results in the far field.

This thesis aims to develop a pragmatic methodology for the simulation of high-Reynolds-number wall-bounded flows, more specifically, confined flows such as square muffler flows. However, as shown in the following chapters, the methodology is generic for wall-bounded flows and not limited to confined flows.

Based on these issues, the following objectives are formulated for the current study:

1. Solve the odd-even decoupling problem via filtering without altering main flow structures and validate it for different test cases.
2. First, implement the basic WSM; then improve the prediction of the mean velocity near the wall via setting up a framework in which the ‘log-layer mismatch’ problem can be analyzed and solved, thus provide a new methodology to improve the prediction of the mean velocity profile in high and moderate Reynolds number attached flows.
3. Apply the wall-modeled LES to the square duct flows and compare the results with experimental results.

1.4 Outline

In order to prepare for the large eddy simulation of turbulent flows, chapter 2, entitled ‘numerical methods’, starts with a description of governing equations of the compressible large-eddy simulation (section 2.1). In section 2.2, the Smagorinsky model and the VMS models are introduced, with a focus on the VMS model and its variants. Section 2.3 briefly discussed the WSM and its solution procedure. The spatial discretization and time stepping schemes are given in Section 2.4.

The issue of odd-even decoupling is addressed in chapter 3. First in section 3.1, the theory related to conservative low-pass filters is briefly reviewed. Next, the

construction of high-order conservative filters near hard boundaries is elaborated in section 3.2. Subsequently, the relevance of conservative filtering is illustrated in section 3.3 for a channel-flow test case, and a 2D cavity flow in section 3.4.

Chapter 4 starts with an analysis in which the relationship between mean shear and its budgets is elaborated for direct numerical simulations based on the DNS data of fully developed channel flow [30]. The analysis is extended to the case of LES of channel flow at high-Reynolds number in section 4.2. A few wall-modeled large eddy simulations are then conducted, using both the Smagorinsky model and VMS model. The budgets of mean velocity gradients are analyzed within the aforementioned framework. It is then shown that over-dissipation does not necessarily mean over-prediction of the mean velocity gradients, unlike the common perception.

Based on the analysis, in section 4.3, a self-adaptive Smagorinsky model for LES of high-Reynolds-number wall-bounded flows is proposed, in which the Smagorinsky coefficient is dynamically adjusted so that a logarithmic mean velocity distribution is captured. The model is then implemented in a second-order finite-volume code, taking into consideration of discretization errors, and applied to a infinite-Reynolds-number channel flow. The desired logarithmic mean velocity distribution is correctly predicted.

In section 4.4, the self-adaptive Smagorinsky model is extended to include the viscous effects. A couple of channel flow cases at moderate Reynolds numbers using the self-adaptive Smagorinsky model and conventional Smagorinsky model are conducted and compared with DNS data. The self-adaptive Smagorinsky model provides a better approximation of the mean velocity profiles compared with the conventional Smagorinsky model and proves to a pragmatic way of dealing with attached turbulent flows at moderate Reynolds numbers.

The turbulent flows in a square duct at high Reynolds number are studied in chapter 5, using the conventional Smagorinsky model and the self-adaptive Smagorinsky model. A literature review is given in section 5.1, followed by a discussion of the validity of classic log law in high-Reynolds number duct flows. A modified log law is then proposed in section 5.2, which provides a better match with the experimental data than the classic log law. The numerical setup is described in section 5.2 as well. The wall-modeled large eddy simulations are then conducted for the duct flows at a Reynolds number of 250000 in section 5.3. The results are compared with the experimental results. The modified log law results in a better prediction of the skin friction, while the self-adaptive Smagorinsky model provides a overall better prediction of both skin friction and the mean velocity profiles. The methodology developed in this chapter provides a pragmatic wall-modeled LES methodology for the simulation of a square duct at high Reynolds number. Finally, the conclusions are drawn in chapter 6.

Chapter 2

Numerical approach

This chapter provides a description of the basic numerical approach employed in this work and the research code FLOWAVE which has been developed as a collaborative effort for large eddy simulation and direct numerical simulation. Section 2.1 introduces the filtered compressible Navier-Stokes equations. The spatial discretization and time integration schemes are described in section 2.2. The SGS models used in the current work are described in section 2.4, with a focus on the VMS model. Finally in section 2.5, the boundary conditions particularly the conventional wall-stress model and the sponge zone technique which is used to damp out the spurious reflections is presented.

2.1 The filtered compressible Navier-Stokes equations

Any flow variable ϕ can be written as $\phi = \bar{\phi} + \phi'$, where $\bar{\phi}$ represents the low-frequency (or large-scale) part of the variable and ϕ' its high frequency (or small-scale) part. $\bar{\phi}$ is obtained via applying the following low-pass filter \mathcal{G} on the computational domain Ω

$$\bar{\phi}(\mathbf{x}, t) = \mathcal{G}\phi(\mathbf{x}, t) = \int_{\Omega} K_G(\mathbf{x} - \xi)\phi(\xi, t)d^3\xi. \quad (2.1)$$

where K_G is the kernel filter function satisfying the normalization relation.

For compressible flow, it is convenient to introduce the Favre filtering operator

$$\tilde{\phi} = \frac{\overline{\rho\phi}}{\bar{\rho}} \quad (2.2)$$

ϕ can be alternatively decomposed as $\phi = \tilde{\phi} + \phi''$ and now the double prime represents a residual or sub-grid scale (SGS) component.

In compressible LES, following the Favre filtering, the velocity $\mathbf{u}(x, t)$ is decomposed into a sum of a filtered (or resolved) component $\tilde{\mathbf{u}}$ and a SGS component $\mathbf{u}''(x, t)$. The filtered velocity field $\tilde{\mathbf{u}}(x, t)$ represents the three-dimensional and time-dependent motions of the large eddies.

The mathematical model for the description of compressible flow is the set of Navier–Stokes equations representing the conservation of mass, momentum and energy. Written in conservative form for the conservative variables (density ρ , momentum $\rho\tilde{u}_i$ and total energy E) and applying the aforementioned Favre filtering operator to the compressible Navier-Stokes equations, the filtered compressible non-dimensional Navier-Stokes equations can be written as [91]

$$\frac{\partial \bar{\rho}}{\partial t} + \frac{\partial \bar{\rho}\tilde{u}_j}{\partial x_j} = 0, \quad (2.3)$$

$$\frac{\partial \bar{\rho}\tilde{u}_i}{\partial t} + \frac{\partial \bar{\rho}\tilde{u}_i\tilde{u}_j}{\partial x_j} + \frac{\partial \bar{p}}{\partial x_i} - \frac{\partial \hat{\sigma}_{ij}}{\partial x_j} = -\frac{\partial \bar{\rho}\tau_{ij}^a}{\partial x_j} + \frac{\partial (\bar{\sigma}_{ij} - \hat{\sigma}_{ij})}{\partial x_j}, \quad (2.4)$$

$$\begin{aligned} \frac{\partial \hat{E}}{\partial t} + \frac{\partial}{\partial x_j} \left(\hat{E} + \bar{p} \right) \tilde{u}_j - \frac{\partial}{\partial x_j} (\hat{\sigma}_{ij}\tilde{u}_i) + \frac{\partial \hat{q}_j}{\partial x_j} = & -\alpha_1 - \alpha_2 - \alpha_3 \\ & + \alpha_4 + \alpha_5 - \alpha_6. \end{aligned} \quad (2.5)$$

The equations have been made dimensionless by introducing a reference length (L_r), velocity (u_r) and density (ρ_r). Non-dimensional parameters are the Mach number,

$$M = \frac{u_r}{c_r}, \quad (2.6)$$

the Reynolds number Re ,

$$Re = \frac{\rho_r u_r L_r}{\mu}, \quad (2.7)$$

and the Prandtl number Pr ,

$$Pr = \frac{c_p \mu}{k}, \quad (2.8)$$

where μ is the dynamic viscosity, k is the thermal conductivity. The Prandtl number Pr and the ratio of the specific heat c_p are set equal to 0.7 and 1.4 respectively (the admitted values for the air). t and x_i are the independent variables representing time and spatial coordinates respectively, while the density ρ , the pressure p and the temperature are linked by the equation of state for perfect gas,

$$\frac{p}{\rho} = \frac{T}{\gamma M^2}. \quad (2.9)$$

τ_{ij}^a , $\hat{\sigma}_{ij}$ and \hat{E} are sub-grid scale stress tensor, viscous stress tensor, and total energy, given respectively

$$\tau_{ij}^a = -\bar{\rho}(\widetilde{u_i u_j} - \tilde{u}_i \tilde{u}_j), \quad (2.10)$$

$$\hat{\sigma}_{ij} = \frac{1}{Re} \left(\frac{\partial \tilde{u}_j}{\partial x_i} + \frac{\partial \tilde{u}_i}{\partial x_j} - \frac{2}{3} \delta_{ij} \frac{\partial \tilde{u}_k}{\partial x_k} \right), \quad (2.11)$$

$$\hat{E} = \frac{\bar{p}}{\gamma - 1} + \frac{1}{2} \rho \tilde{u}_j \tilde{u}_j; \quad (2.12)$$

while the filtered heat flux is expressed as

$$\hat{q}_j = -\frac{1}{(\gamma - 1) Re Pr M^2} \frac{\partial \tilde{T}}{\partial x_j}. \quad (2.13)$$

The use of mass-weighted filtered variable \tilde{u} instead of the filtered velocity \bar{u} prevents the appearance of sub-grid terms in Eq. 2.3.

The six subgrid terms in the energy equation are defined as [91]

$$\begin{aligned} \alpha_1 &= -\tilde{u}_i \frac{\partial \bar{\rho} \tau_{ij}^a}{\partial x_j}, \alpha_2 = \frac{1}{\gamma - 1} \frac{\partial \overline{p u_j} - \bar{p} \tilde{u}_j}{\partial x_j}, \\ \alpha_3 &= \overline{p \frac{\partial u_k}{\partial x_k}} - \bar{p} \frac{\partial \tilde{u}_k}{\partial x_k}, \alpha_4 = \overline{\sigma_{ij} \frac{\partial u_i}{\partial x_j}} - \bar{\sigma}_{ij} \frac{\partial \tilde{u}_i}{\partial x_j}, \\ \alpha_5 &= \frac{\partial (\bar{\sigma}_{ij} \tilde{u}_i - \hat{\sigma}_{ij} \tilde{u}_i)}{\partial x_j}, \alpha_6 = \frac{\partial (\bar{q}_j - \hat{q}_j)}{\partial x_j} \end{aligned} \quad (2.14)$$

It is important to notice that no hypothesis has been made up to this point and no term has been neglected. The nonlinear subgrid terms on the right hand side of the filtered momentum and energy equations arise due to filtering operation. These terms are not closed and can not be computed from the flow variables, thus should be modeled. In the next section, it will be shown how these terms are treated and modeled.

2.2 Sub-grid scale (SGS) models

The terms on the right hand side of Eq. 2.4 and Eq. 2.5 reflect the effects of unresolved scales of motion on large scales and need to be modeled. The SGS models for the unclosed terms for both the momentum and energy equation are detailed in subsections 2.2.1 and 2.2.2 respectively.

2.2.1 Momentum equation

A priori test by Vreman [91] showed the SGS term $\partial(\bar{\sigma}_{ij} - \hat{\sigma}_{ij})/\partial x_j$ to be one order smaller than the term $\partial\bar{\rho}\tau_{ij}^a/\partial x_j$ so that it is typically neglected. Two SGS models, i.e., the Smagorinsky model and the variational multi-scale (VMS) model which are employed in current work are described.

The Smagorinsky model

The most common SGS model is the Smagorinsky model [91]. The Smagorinsky model falls into the category of eddy viscosity models, which assume the subgrid stress tensor to be proportional to the resolved strain rate. The deviatoric part of the SGS stress tensor is modeled by the eddy viscosity model

$$\tau_{ij} = \tau_{ij}^a - \frac{1}{3}\tau_{kk} = -\nu_t \tilde{S}_{ij}, \quad (2.15)$$

where

$$\tilde{S}_{ij} = \frac{1}{2} \left(\frac{\partial \tilde{u}_i}{\partial x_j} + \frac{\partial \tilde{u}_j}{\partial x_i} - \frac{2}{3} \delta_{ij} \frac{\partial \tilde{u}_k}{\partial x_k} \right) \quad (2.16)$$

is the resolved strain rate and ν_t is the eddy viscosity of the residual motions. By analogy to the mixing-length hypothesis, the eddy viscosity is modeled as

$$\nu_t = l_s^2 |\tilde{S}| = (C_s \Delta)^2 |\tilde{S}|, \quad (2.17)$$

where $|\tilde{S}|$ is the short for $\left(2\tilde{S}_{ij}\tilde{S}_{ij}\right)^{1/2}$. Thus, the Smagorinsky model reads

$$\tau_{ij} = -2C_s^2 \Delta^2 |\tilde{S}| \tilde{S}_{ij}, \quad (2.18)$$

with C_s the Smagorinsky coefficient and Δ the filter width, a length scale which is assumed to be related to the grid cutoff, and it is common practice to take

$$\Delta = (h_x h_y h_z)^{1/3} \quad (2.19)$$

with h_x , h_y , and h_z the local grid spacing in x , y , and z directions. In principle, C_s is assumed to be a universal constant. In the literature, different values of this constant are reported for different flow regimes. As is shown later on, the value of C_s is not a constant, but influenced by many factors such as numerical errors introduced by discretization, viscous effects, the existence of scale separation (which is a precondition for the LES, though is not satisfied near the wall for wall-bounded flows), whether the grid cut-off scale is in the inertial sub-range and finally the shape of the filtering operator. As a result, the optimal value of C_s is not only different from case to case, but also varies in different regions of the same flow regime. Thus in this thesis, the C_s is referred to as the Smagorinsky coefficient instead of the Smagorinsky constant.

Assuming infinite Reynolds number and neglecting turbulent dissipation, the production of turbulent subgrid kinetic energy balances the dissipation of subgrid energy ϵ_t . The production of subgrid energy is given by

$$P = -\tau_{ij}\tilde{S}_{ij} = 2\nu_t\tilde{S}_{ij}\tilde{S}_{ij} = \nu_t|\tilde{S}|^2, \quad (2.20)$$

which represents the transfer of energy from resolved motions to the residual motions. Thus one obtains [59]

$$\epsilon_t \approx 2\langle\nu_t\rangle \int_0^\infty k^2 E(k) dk \quad (2.21)$$

and

$$\nu_t \approx (C_s\Delta)^2 \left(\int_0^\infty k^2 E(k) dk \right)^{1/2}, \quad (2.22)$$

where k is the wavenumber. Lilly [50] assumed a sharp cut-off filter with cut off $k_c = \pi/\Delta$ and further an inertial range spectrum to obtain the result

$$C_s = \frac{l_s}{\Delta} = \frac{1}{\pi} \left(\frac{2}{3C} \right)^{3/4} \approx 0.17, \quad (2.23)$$

where $C = 1.6$ is the Kolmogorov constant.

However, one must note, several assumptions have been made during the derivation of the value of C_s . First, the viscous effect has been neglected, i.e., infinite Reynolds number is assumed. Second, the filter cut-off should situate in the inertial subrange so that the $-5/3$ law is valid, this in turn requires the Reynolds number should be high enough to ensure that the scale separation happens and the inertial subrange exists. In low Reynolds number applications, an inertial sub-range does not or almost not exist, the validity of the aforementioned coefficient is questionable. Even in some high-Reynolds-number applications, such as wall-bounded flows, the scale separation does not

exist near the wall. The investigation of the Reynolds number dependency of the Smagorinsky coefficient is thus relevant. Third, the filter is assumed to be a sharp cut-off filter. However, explicit filtering might be involved in some SGS models, such as the dynamic Smagorinsky model [19] and VMS model [33]. In those cases the influence of the shape of the explicit filters on the Smagorinsky coefficient should be taken into account. Finally, discretization errors will result in an energy spectrum $\overline{E}(k)$ which is different from the desired $-5/3$ law.

More systematic and detailed discussions on how to determine the value of C_s and error assessment of LES can be found in [59, 57, 60, 58, 56, 13]. In [59], the dependency of C_s on two important parameters is addressed, i.e. the ratio of the LES-filter width Δ and the Kolmogorov scale η on the one hand, and the ratio of the integral length scale L and the LES-filter width Δ on the other hand. The viscous effect is incorporated into the total dissipation, and a new parameter γ_0 is introduced to account for the shape of the low-pass filter [59]

$$\gamma_0 = \frac{\left(\frac{4}{3} \int_0^\infty k^{1/3} (G(k))^2 dk\right)^{3/4}}{\pi/\Delta}, \quad (2.24)$$

where $G(k)$ is the transfer function of the filter, for sharp cut-off filter $G(k) = 1$. A modified eddy viscosity is finally proposed, corresponds to

$$\nu_t^* = \sqrt{(C_{s,\infty} \Delta / \gamma_0)^4 \langle 2\tilde{S}_{ij}\tilde{S}_{ij} \rangle + \nu^2} - \nu, \quad (2.25)$$

to account for low-Reynolds-number effects and the shape of the low-pass filter.

The VMS model

Hughes et al. [31], in the context of a VMS framework for LES, presented the hypothesis that the Smagorinsky model applied to a small-scale extraction of the turbulent field, delivers superior results compared to a standard Smagorinsky model. Furthermore, the VMS method separates the scales a priori. And most importantly, it assumes the interaction happens mainly between the smallest resolved scales and sub-grid scales. The effect of the unresolved scales is modeled through relating the SGS stress to the smaller resolved scales instead of the larger scales. Consequently, in the VMS model, energy is extracted from the fine resolved-scales via an explicit high-pass filtering operation, and no energy is directly extracted from the large structures in the flow. For this reason, the VMS model is less dissipative near walls and in the presence of large coherent structures. Hence, for wall-bounded flows, the VMS model does not need any damping function near the wall to reduce the SGS dissipation.

In later studies, this was further validated by a series of studies, for instance, Hughes et al. [32] for homogeneous isotropic turbulence and Hughes et al. [33] for a channel flow.

In their various articles, Hughes et al. present several different versions of the VMS Smagorinsky model, i.e. the large–small, the all–small, and the small–small formulations. A variant of small–small formulation [60] is employed in the current work.

First, the small-scale extraction of a property $f(\mathbf{x})$ is defined as

$$f'(\mathbf{x}) = \mathcal{H}' f = \int_{\Omega} K_{\mathcal{H}'}(\mathbf{x} - \xi) \phi(\xi, t) d^3\xi, \quad (2.26)$$

where \mathcal{H}' is a high-pass filter, introduced to restrict the interaction of the subgrid-model with the LES solution to the small resolved scales only. In contrast to the low-pass filter \mathcal{G} , the application of \mathcal{H}' to a constant function yields $\mathcal{H}' c = 0$. The original small–small formulation is then formulated as

$$\tau_{ij} = -[2C_s^2 \Delta^2 |\tilde{S}'| \tilde{S}'_{ij}]', \quad (2.27)$$

where $|\tilde{S}'| = \left(2\tilde{S}'_{ij}\tilde{S}'_{ij}\right)^{1/2}$. Meyers and Sagaut [59, 60] calibrated the Smagorinsky coefficient in the small–small VMS model via taking into account the influence of finite Reynolds number and shape of the explicit filters. This variant of the small–small VMS model together with the conventional Smagorinsky model and the newly developed self-adaptive Smagorinsky model (see chapter 4) are employed as SGS models in this work. More details on this variant of the small–small VMS model will be given in following paragraphs.

The aforementioned analysis on Smagorinsky coefficient is extended to the VMS model in [59]. Three variants of the small–small VMS model are proposed and validated over a couple of channel flow test cases [60], among which the so-called ‘Model C’ is theoretically most complete and yields superior results over the other two, and is thus chosen in the current work. The formulation of this model reads [60]

$$\boldsymbol{\tau} = -2 \left[\frac{(\gamma_0/\gamma_\beta)^{4/3}}{1 - \beta^{4/3}} \times \left(\sqrt{\left(\frac{C_{s,\infty}\Delta}{\gamma_0}\right)^4 \frac{(\gamma_0/\gamma_\beta)^{4/3} |\tilde{S}'|^2}{1 - \beta^{4/3}} + \nu^2 - \nu} \right) \tilde{\mathbf{S}}' \right]', \quad (2.28)$$

the coefficients β , γ_0 and γ_β , and are related to the shape of the filters. $\beta = \Delta/\Delta'$ is the ratio of the \mathcal{G} -filter width to the \mathcal{H}' -filter width. The factor $(1 - \beta^{4/3})^{-3/4}$ accounts for the difference between the standard Smagorinsky formulation, which employs all resolved LES scales, and the small–small model, which uses

a small-scale part of the resolved field in its formulation. γ_β is defined as follows [60]

$$\gamma_\beta = \left(\frac{1}{3\pi} \frac{\int_{-\pi/h_x}^{\pi/h_x} \int_{-\pi/h_y}^{\pi/h_y} \int_{-\pi/h_z}^{\pi/h_z} k^{-5/3} [H'((k))G((k))]^2 dk_x dk_y dk_z}{(\pi/\Delta)^{4/3} (1 - \beta^{4/3})} \right)^{3/4}, \quad (2.29)$$

and used to account for the shape of \mathcal{G} and \mathcal{H} . Finally molecular viscosity ν appears in Eq. 2.28, accounting for finite-Reynolds-number effects. The high-pass filter used here is constructed by using a top-hat filter, discretized using a trapezoidal integration rule. The six components of the velocity strain rates and turbulent stress are filtered consecutively on six faces in three directions. More information concerning the explicit high-pass filters employed in the VMS formulation can be found in chapter 3.

Error analysis of LES

An assessment of LES errors was made for a variety of central finite-volume discretizations in [57], and the author concluded that it is advisable to use the same order of accuracy of discretization for convective and dissipative terms. Winckelmans and his coworkers provided a convenient fit for the C_s/C_∞ in homogeneous isotropic turbulence as a function of Δ/η [13], where C_∞ is the asymptotic coefficient.

The error-landscape approach is used for the evaluation of the Smagorinsky model in [58, 56], and an optimal combination of model parameter and resolution is decided based on the numerical results. The authors clarified that using a pseudo-spectral discretization, the asymptotic Smagorinsky coefficient converges at fine mesh resolutions to the high-Re theoretical Lilly prediction for the Smagorinsky coefficient. Using modified wavenumbers in the same spectral code, the asymptotic value based on LES with ‘‘second-order’’ discretization errors is also presented. Though the wavenumber is modified, the main difference from an actual second-order scheme is that the analysis is based on a ‘known’ $k^{-5/3}$ spectrum, while in reality not only the effective wavenumber deviates from the actual one, but also the spectrum is no longer the $k^{-5/3}$ spectrum. Hence, in this analysis the only discretization effect entering into the analysis is the discrete representation of $|S|$ and S_{ij} . Nevertheless, the analysis sheds some light on the relationship of the spatial discretization errors and the Smagorinsky coefficient. The previously introduced correction factor γ_0 is then replaced with

$$\gamma_D = \frac{\left(\frac{4}{3} \int_0^\infty k^{1/3} (G(k))^2 G_D(k) dk \right)^{3/4}}{\pi/\Delta}, \quad (2.30)$$

with $G_D(k)$ being the filter induced by the discretization of $|S|$. Using the modified wavenumbers for a second-order discretization, $G_D(k)$ corresponds to [58]

$$G_D(k) = 2 \frac{\sum_{i=1}^3 [1 - \cos(k_i \Delta)]}{(k\Delta)^2}. \quad (2.31)$$

Integration of Eq. (2.30) using this filter leads to $\gamma_D = 1.005$, while for a pseudo-spectral discretization, $\gamma = 1.21$. For the isotropic turbulence at high Reynolds numbers, assuming a cubical sharp cut-off filter, the Smagorinsky coefficient for the pseudo-spectral discretization and ‘second-order’ discretization are then given as

$$C_s = \frac{C_{s,\infty}}{\gamma_0} \approx 0.165, \quad (2.32)$$

$$C_{s,D} = \frac{C_{s,\infty}}{\gamma_D} \approx 0.135. \quad (2.33)$$

Thus the ‘second-order’ discretization leads to higher value of the Smagorinsky coefficient.

2.2.2 Energy equation

In section 2.2.1, the unclosed SGS term in the momentum equation is addressed. However, as shown in Eq. (2.5) and Eq. (2.14), six SGS terms arise due to Favre average. Not much attention has been paid to this topic, especially for compressible LES. Vreman conducted numerical experiments in a compressible mixing layer [91], and confirmed the relative importance of α_1 and α_2 compared with other SGS terms. He also found the SGS terms in the energy equation have a very small impact on the velocity components. The cases studied in this thesis are all low-Mach-number cases without large temperature gradients and Vreman’s practice is followed here, with all the other terms neglected except for α_1 and α_2 .

The model for α_1 is straightforward: the aforementioned models for SGS stress τ_{ij} are directly applied here. α_2 is modeled in the same spirit as the SGS term in the momentum equation and is given by

$$\alpha_2 = \frac{\nu_t c_p}{Pr_t} \nabla T, \quad (2.34)$$

where Pr_t is the turbulent Prandtl number, prescribed as a constant value 0.7 in this thesis.

2.3 Spatial and time discretization schemes

In this section, a description of the spatial discretization and time integration technique is given. In section 2.3.1, the flux reconstruction and face integration for convective fluxes are firstly described, followed by the 4th-order Runge-Kutta time integration scheme. The governing equations are discretized using a finite-volume method on a collocated grid. The Navier-Stokes equations in the integral form read [92]

$$\int_{\Omega_{i,j,k}} \frac{\partial \mathbf{Q}}{\partial t} dx dy dz + \int_{\Omega_{i,j,k}} \mathbf{I} \cdot \mathbf{n} ds = 0 \quad (2.35)$$

where

$$\mathbf{Q} = \begin{bmatrix} \bar{\rho} \\ \bar{\rho} \tilde{u} \\ \bar{\rho} \tilde{v} \\ \bar{\rho} \tilde{w} \\ \bar{\rho} \hat{E} \end{bmatrix} \quad (2.36)$$

are the conservative variables, $\Omega_{i,j,k}$ is the volume of the control volume (CV) and

$$\mathbf{I} \cdot \mathbf{n} = \mathbf{I}_c \cdot \mathbf{n} - \mathbf{I}_d \cdot \mathbf{n} + \mathbf{I}_t \cdot \mathbf{n}. \quad (2.37)$$

\mathbf{I}_c , \mathbf{I}_d and \mathbf{I}_t represent the convective, viscous and SGS terms respectively and given by

$$\mathbf{I}_c \cdot \mathbf{n} = \begin{bmatrix} \bar{\rho} \tilde{\mathbf{u}} \cdot \mathbf{n} \\ \bar{\rho} \tilde{u} \tilde{\mathbf{u}} \cdot \mathbf{n} + \bar{p} n_1 \\ \bar{\rho} \tilde{v} \tilde{\mathbf{u}} \cdot \mathbf{n} + \bar{p} n_2 \\ \bar{\rho} \tilde{w} \tilde{\mathbf{u}} \cdot \mathbf{n} + \bar{p} n_3 \\ \bar{\rho} \hat{E} \tilde{\mathbf{u}} \cdot \mathbf{n} + \bar{p} \mathbf{u} \cdot \mathbf{n} \end{bmatrix}, \mathbf{I}_d \cdot \mathbf{n} = \begin{bmatrix} 0 \\ \rho(\mathbf{i}\hat{\sigma}_{11} + \mathbf{j}\hat{\sigma}_{12} + \mathbf{k}\hat{\sigma}_{13}) \cdot \mathbf{n} \\ \rho(\mathbf{i}\hat{\sigma}_{12} + \mathbf{j}\hat{\sigma}_{22} + \mathbf{k}\hat{\sigma}_{23}) \cdot \mathbf{n} \\ \rho(\mathbf{i}\hat{\sigma}_{13} + \mathbf{j}\hat{\sigma}_{23} + \mathbf{k}\hat{\sigma}_{33}) \cdot \mathbf{n} \\ \rho(\mathbf{i}\alpha_1 + \mathbf{j}\alpha_2 + \mathbf{k}\alpha_3) \cdot \mathbf{n} \end{bmatrix}, \quad (2.38)$$

and

$$\mathbf{I}_t \cdot \mathbf{n} = \begin{bmatrix} 0 \\ \rho(\mathbf{i}\tau_{11} + \mathbf{j}\tau_{12} + \mathbf{k}\tau_{13}) \cdot \mathbf{n} \\ \rho(\mathbf{i}\tau_{12} + \mathbf{j}\tau_{22} + \mathbf{k}\tau_{23}) \cdot \mathbf{n} \\ \rho(\mathbf{i}\tau_{13} + \mathbf{j}\tau_{23} + \mathbf{k}\tau_{33}) \cdot \mathbf{n} \\ \rho(\mathbf{i}\beta_1 + \mathbf{j}\beta_2 + \mathbf{k}\beta_3) \cdot \mathbf{n} \end{bmatrix}, \quad (2.39)$$

where α_i and β_i are defined as $\tilde{u}_j \hat{\sigma}_{ij} - q_i$ and $\tilde{u}_j \tau_{ij}$ respectively, \mathbf{i} , \mathbf{j} and \mathbf{k} are the unit vectors co-directional with the x, y, and z axes in the three dimensional Cartesian coordinate system, \mathbf{n} is the surface normal vector. The surface integrals in Eq. (2.35) may be splitted into six face integrals for a 3-D CV.

2.3.1 Face integration

The face integrals can be approximated by either assuming that the value of a quantity at CV face center represents the mean value over the face (mid-point rule approximation) or more accurately, evaluating the fluxes at more locations.

Second order

The simplest approximation to the integral is the midpoint rule, where the integral is approximated as a product of the flux vectors and the area of the surface. For instance, for the face $i + 1/2, j, k$, the face integral can be approximated as

$$F_{i+\frac{1}{2},j,k} = \int_{S_{i+\frac{1}{2},j,k}} Ids \approx I_{i+\frac{1}{2},j,k} S_{i+\frac{1}{2},j,k}, \quad (2.40)$$

which has a second-order accuracy.

Fourth order

Higher-order approximations of the integrals have to be evaluated at more locations. For the case of 2D, the surfaces become lines, as shown in Fig. 2.1. For the line $i + 1/2, j$, following Simpson's rule, a fourth-order approximation estimates the integral over a surface as

$$F_{i+\frac{1}{2},j} = \int_{S_{i+\frac{1}{2},j}} Ids \approx \frac{S_{i+\frac{1}{2},j}}{6} (I_{i+\frac{1}{2},j+\frac{1}{2}} + 4I_{i+\frac{1}{2},j} + I_{i+\frac{1}{2},j-\frac{1}{2}}), \quad (2.41)$$

whereas for 3D, the fourth-order approximation of the integral over the faces reads

$$F_{i+\frac{1}{2},j,k} = \int_{S_{i+\frac{1}{2},j,k}} Ids \approx \frac{S_{i+\frac{1}{2},j,k}}{36} (16I_{i+\frac{1}{2},j,k} + 4(I_{i+\frac{1}{2},j-\frac{1}{2},k} + I_{i+\frac{1}{2},j+\frac{1}{2},k} + I_{i-\frac{1}{2},j,k-\frac{1}{2}} + I_{i-\frac{1}{2},j,k+\frac{1}{2}}) + I_{i+\frac{1}{2},j-\frac{1}{2},k-\frac{1}{2}} + I_{i+\frac{1}{2},j+\frac{1}{2},k-\frac{1}{2}} + I_{i-\frac{1}{2},j-\frac{1}{2},k+\frac{1}{2}} + I_{i-\frac{1}{2},j+\frac{1}{2},k+\frac{1}{2}}) \quad (2.42)$$

Fourth-order face integration is only available for the convective fluxes while second-order face integration is available for both the convective and viscous fluxes.

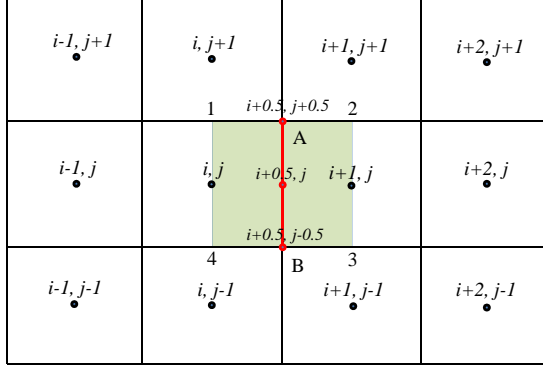


Figure 2.1: Interpolation arrangement for 2D finite volume method. The primitive variables are interpolated to the cell interface $i + 1/2$ where the gradient tensor of the variables is calculated over a staggered control volume, and the fluxes are reconstructed.

In previous section, one notices that the flux vectors which are used to compute the face integrals are defined on the faces of the CV. Since the variables are collocated and cell-centered, the convective flux vectors defined on the faces have to be calculated from the primitive variables which are interpolated from cell centers. In FLOWAVE, central interpolation schemes are employed to avoid artificial dissipation. To reconstruct the convective flux, the primitive variables are interpolated to the faces of the CV using Lagrangian interpolation

$$\phi(x) = \sum_{k=i-\frac{n}{2}}^{i+\frac{n}{2}} \phi(x_{k+\frac{1}{2}}) \prod_{l=i-\frac{n}{2}, l \neq k}^{i+\frac{n}{2}} \frac{(x - x_{l+\frac{1}{2}})}{(x_{l+\frac{1}{2}} - x_{k+\frac{1}{2}})}, \quad (2.43)$$

where ϕ can be any of the primitive variables (ρ, u, v, w, p) .

For the computation of viscous fluxes and SGS fluxes, the velocity gradient tensor has to be calculated at the faces using a staggered control volume. Fig. 2.1 shows the 2D equidistant grid topology, where the gradient on line A-B (corresponding to $i - 1/2, j$) is computed as

$$\begin{aligned} \nabla \phi_{AB} &= \frac{1}{V_{1234}} \int_{1234} \nabla \phi dV = \frac{1}{V_{1234}} (\phi_{i+\frac{1}{2}, j+\frac{1}{2}} S_{i+\frac{1}{2}, j+\frac{1}{2}} + \\ &\quad \phi_{i, j} S_{i, j} + \phi_{i+1, j} S_{i+1, j} + \phi_{i+\frac{1}{2}, j-\frac{1}{2}} S_{i+\frac{1}{2}, j-\frac{1}{2}}), \end{aligned} \quad (2.44)$$

where $\phi_{i+\frac{1}{2}, j+\frac{1}{2}}$ and $\phi_{i+\frac{1}{2}, j-\frac{1}{2}}$ are interpolated from neighboring grid points.

2.3.2 Time integration

After the spatial derivatives of the filtered Navier-Stokes equations have been discretized using the finite volume method, the integral of the temporal term in Eq. (2.35) also has to be evaluated over the control volume. For a second order approximation of the volume integral, it reads:

$$\int_{\Omega_{i,j,k}} \frac{\partial \mathbf{Q}}{\partial t} dx dy dz = \frac{d}{dt} \int_{\Omega_{i,j,k}} \mathbf{Q} dx dy dz \approx \frac{d\mathbf{Q}}{dt} \Omega_{i,j,k}. \quad (2.45)$$

In a more compact form, Eq. (2.35) can be written in a compact form as

$$\frac{d\mathbf{Q}}{dt} \Omega_{i,j,k} = R, \quad (2.46)$$

where R represents the residual, i.e. discretized spatial terms, defined as

$$R = - \sum_{f=1}^6 \mathbf{I}_c S_f + \sum_{f=1}^6 \mathbf{I}_d S_f - \sum_{f=1}^6 \mathbf{I}_t S_f. \quad (2.47)$$

Eq. (2.46) then becomes a set of ordinary differential equations (ODEs) representing an initial value problem where starting from an initial condition, the solution can be advanced by integrating in time. In this work, the 4th-order Runge-Kutta scheme has been chosen as the time integration scheme, due to its high accuracy and bigger stability region compared with conventional 2nd-order Euler method. The scheme is given by [28].

$$\begin{aligned} Q^{(1)} &= Q^n \\ Q^{(2)} &= Q^n + \frac{1}{2} \Delta t_* R^{(1)} \\ Q^{(3)} &= Q^n + \frac{1}{2} \Delta t_* R^{(2)} \\ Q^{(4)} &= Q^n + \Delta t_* R^{(3)} \\ Q^{n+1} &= Q^n + \frac{\Delta t_*}{6} (R^{(1)} + 2R^{(2)} + 2R^{(3)} + R^{(4)}). \end{aligned} \quad (2.48)$$

Runge-Kutta scheme is an explicit time-stepping scheme, where the time step is determined at every CV to satisfy the stability requirement and the smallest one is taken as the global time step for the whole computational domain. The CFL number is normally set as a low value such as 1 during the transient period to avoid numerical instability, and then slowly increased to a value up to 3 after the flow gets stabilized.

2.4 Boundary conditions

Three types of boundary conditions are used in this work, the classical CFD boundary conditions, the wall-stress model and the sponge zone technique, which is used to damp out the spurious reflection at the boundaries for CAA calculations.

2.4.1 Classical boundary conditions

- Inlet. Three velocity components and static temperature are imposed.
- Outlet. Static temperature is imposed.
- Isothermal wall. Static temperature is imposed. Either slip wall or non-slip wall boundary condition is employed, depending on whether the wall is modeled or not. If the WSM is used, the slip wall is chosen, otherwise, the non-slip wall boundary condition is imposed.
- Periodic boundaries.
- Free boundary condition. Values of primitive variables are prescribed at the boundary.

These boundary conditions are well known and can be found in any classical CFD textbooks such as [17] or [28].

2.4.2 The wall stress model

As mentioned in chapter 1, the wall-stress model is used in combination with SGS models to prescribe the wall stress at the wall without resolving the wall. The premise is that the mean velocity, normalized by inner-layer scale, follows a logarithmic distribution against the normalized wall distance:

$$\frac{U_R}{u_\tau} = \frac{1}{\kappa} \log\left(\frac{y_w u_\tau}{\nu}\right) + B \quad (2.49)$$

where y_w is the distance from the nearest wall, u_τ is the friction velocity and related to the shear stress at the wall via

$$\langle \tau_w \rangle = u_\tau^2 \rho, \quad (2.50)$$

and U_R is the mean velocity at the first grid point from the wall

$$U_R = (\langle \widetilde{u_1} \rangle^2 + \langle \widetilde{u_2} \rangle^2)^{0.5}. \quad (2.51)$$

Eq. (2.49) yields an implicit relation for u_τ , depending on the von Kármán constant $\kappa = 0.41$, the constant $B = 5.2$ (details on κ , and B , and a discussion on their universality may be found in Marusic [53]). u_1 and u_2 correspond to the wall-parallel velocity components. The eventual stress components in x_1 and x_3 directions are then obtained using $\tau_{w,i} = \tau_w \tilde{u}_i$ ($i = 1, 2$). The ‘ $\langle \rangle$ ’ represents ensemble average, which is replaced by a local formulation in present work. As pointed out in [4], imposing the wall stress in a local formulation leads to increased average stresses for a given near-wall velocity. They found a time-filtered formulation gives better results. Thus first order time filtering for the wall-parallel velocity components which are used to prescribe the wall stress is introduced and takes the following form

$$\tilde{\tilde{u}}_{i,n+1} = (1 - r)\tilde{\tilde{u}}_{i,n} + r\tilde{u}_{i,n+1}, i = 1, 2. \quad (2.52)$$

where

$$r = \frac{\Delta T}{\Delta T + \tau} \quad (2.53)$$

with ΔT size of time step and τ width of the time filter.

Eq. (2.49) is an implicit equation for u_τ and will be solved using an iterative Newton method at every point and at every Runge-Kutta stage. We write the following equation

$$f(x) = -\frac{a}{x} + b \log(cx) + d = 0 \quad (2.54)$$

where x represents the friction velocity u_τ , a , b , c and d are either known as a prior or calculated from the flow field and given as (in the case of dimensionless calculation):

$$a = U_R, b = \frac{1}{\kappa}, c = \frac{y_w}{\gamma} = y_w Re, d = B \quad (2.55)$$

The algorithm will take this form:

$$x_{n+1} = x_n - \frac{f(x_n)}{f'(x_n)} = x_n - \frac{dx^2 - ax + bx^2 \log(cx)}{a + \frac{b}{\ln c} x} \quad (2.56)$$

The convergence criteria will be

$$\frac{|x_{n+1} - x_n|}{|x_n|} \leq 10^{-5} \quad (2.57)$$

During the transient period, the number of the Newton iterations is high, as the flow gets developed, normally only one or two Newton iterations are needed.

Also for rough walls, where $\delta_\nu \ll y_0$ ($\ll \delta$), with y_0 the surface roughness, prescribed as the inner-layer scale, stress-boundary conditions are often used. Resolving the geometrical roughness details of the wall is impractical, and instead, a stress-model based on Monin–Obhukov similarity theory for rough walls yields [61]

$$\tau_{w,i} = \left[\frac{\kappa}{\log(y/y_0)} \right]^2 (\bar{u}_1^2 + \bar{u}_2^2)^{1/2} \bar{u}_i \quad (i = 1, 2), \quad (2.58)$$

which is an explicit equation and y_0 is known a priori.

2.4.3 The Sponge zone technique

To minimize the spurious reflection generated by acoustic waves at the boundaries and to avoid vortical structures hitting the outlet, a sponge zone technique [14] is used and a buffer layer is added to the computational domain. In this zone, acoustic waves and vortical structures are damped by an additional term appearing on the right hand side of the momentum equations:

$$\frac{\partial \mathbf{Q}}{\partial t} + \dots = -\frac{c}{\Delta x_i} \sigma_{max} \left(\frac{x_i - x_0}{x_{i,max} - x_{i,0}} \right)^2 (\mathbf{Q} - \mathbf{Q}^*), \quad (2.59)$$

where c is the local speed of sound, σ_{max} is a buffer parameter, normally set to a value of 0.25, $x_{i,0}$ and $x_{i,max}$ are coordinates, indicating the beginning and end of the buffer zone, and \mathbf{Q}^* is the target state, equal to the free-stream conditions.

Chapter 3

Conservative filtering

In this chapter, the globally conservative high-order accurate filters are described, which combine traditional selective filters at the internal points with one-sided conservative filters near the wall boundary. Firstly, theory related to conservative low-pass filters is briefly reviewed, followed by the construction of high-order conservative filters near hard boundaries. In Section 3.4, the importance of using conservative filters for the formulation of the VMS Smagorinsky model is illustrated for the channel flow test case. The globally conservative filters are then applied to remove odd-even decoupling both in a channel flow case and in a 2D cavity flow. It is shown that the use of a non-conservative filter leads to erroneous predictions of the skin friction in channel flows up to 30%. In the cavity flow simulations, the use of non-conservative filters to remove odd-even decoupling leads to important shifts in the Strouhal number of the dominant mode, and a change of the flow pattern inside the cavity. In all cases, the use of conservative high-order filter formulations to remove odd-even decoupling leads to very satisfactory results. Finally, a tentative analysis of the effect of the incoming boundary layer on the flow patterns is briefly discussed. The work discussed in this chapter is published in [93] and [94].

3.1 Conservation properties

It is well documented that the LES equations (2.3–2.5) follow from basic conservation of mass, momentum, and energy. Also in numerical implementations, these properties are best retained in the formulations. As discussed in previous section, this is not always the case when, e.g., high-order selective filters are

used to remove odd-even decoupling. To further clarify this point, we focus here on the conservation of momentum (Eq. 2.4). Integrating this equation over the whole computational domain Ω , and presuming for sake of argument that the system is in statistical equilibrium, we obtain

$$\begin{aligned} \int_{\Omega} \frac{\partial \rho \mathbf{v}}{\partial t} \, d\mathbf{x} &\approx 0 \approx - \int_{\delta\Omega} (\rho \mathbf{v} \otimes \mathbf{v}) \cdot \mathbf{n} \, d\mathbf{x} - \int_{\delta\Omega} p \mathbf{n} \, d\mathbf{x} \\ &+ \int_{\delta\Omega} \hat{\boldsymbol{\sigma}} \cdot \mathbf{n} \, d\mathbf{x} - \int_{\delta\Omega} \boldsymbol{\tau} \cdot \mathbf{n} \, d\mathbf{x}, \end{aligned} \quad (3.1)$$

where we used Gauss' theorem to reformulate some of the volume integrals into integrals over the boundaries $\delta\Omega$ of the computational domain, and \mathbf{n} is the normal on that boundary. We further elaborate this by means of a practical example, which will also be one of the test cases in the current work. Consider a channel flow between two flat parallel plates with a distance of H . The computational domain is a box with fully developed inflow and outflow conditions in x , walls in y , and periodic boundary conditions in z directions. The length of the domain is L . For this case, Eq. (3.1) further simplifies to

$$H \Delta p = -2(\tau_w + \tau_{M,w})L, \quad (3.2)$$

yielding the classical relation between pressure drop and friction losses at the wall (with τ_w , and $\tau_{M,w}$, respectively the mean wall stress, and the mean subgrid-scale stress at the wall).

In compressible-flow simulations at low Mach number using higher-order discretization schemes, simulations can be susceptible to odd-even decoupling (or so-called π -modes), which are not physical, and may lead to unrealistic solutions or divergence of the simulations. In order to control this in aeroacoustics simulations, high-order filters which remove odd-even decoupling, can be employed. For instance, to remove π -modes, the velocity field \mathbf{v} may be filtered every n time steps (with, e.g., $n = 5$ or $n = 1$ depending on the computational grid and the case [52]). In case such a filter is conservative, we have for any function $f(\mathbf{x})$ in the domain Ω , and using \bar{f} to denote the filtered function, that

$$\int_{\Omega} \bar{f}(\mathbf{x}) \, d\mathbf{x} = \int_{\Omega} f(\mathbf{x}) \, d\mathbf{x}. \quad (3.3)$$

In Section 3.2, it is demonstrated that the construction of a conservative high-order filter is non-trivial, and requires special treatment of the filter coefficients near the boundaries of the computational domain. In case the filter is non-conservative, the filtering of the velocity field \mathbf{v} every n time steps will lead to

$$\int_{\Omega} \left. \frac{\partial \rho \mathbf{v}}{\partial t} \right|_{t=n\Delta t} \, d\mathbf{x} \neq 0, \quad (3.4)$$

which results in the introduction of an artificial force into the momentum balance expressed in Eq. (3.1) and Eq. (3.2). In Section 3.4, it is further illustrated that this can lead to large simulation errors both in classical LES and in aero-acoustics simulations.

Finally, in Eq. (3.2) the subgrid-scale stresses at the wall $\tau_{M,w}$ play a role in the overall force balance of the channel-flow example. In wall-resolved LES, it is well documented that $\tau_{M,w} = 0$ is required (cf. e.g., Refs. [67, 74]). However, the use of non-conservative filters for the formulation of the VMS Smagorinsky model (cf. Eq. 2.28) can lead to $\tau_{M,w} \neq 0$, which also introduces parasite forces in the global momentum balance. In Section 3.4, we will illustrate this for the VMS model, using either a conservative or a non-conservative top-hat filter for the construction of the VMS high-pass filter used in the model.

3.2 Self-adjoint filters

An important theoretical background on conservation properties of filters for use in large-eddy simulations, was elaborated by Vreman [90], who showed that a normalized filter is conservative if it is self-adjoint. In the current subsection, we briefly review the main elements of Vreman's work.

In continuous form, a spatial filter operator may be defined as [90]

$$\mathcal{G}f(x) = \int_{\Omega} K_G(x, \xi) f(\xi) d\xi, \quad (3.5)$$

where $K_G(x, \xi)$ is the filter kernel. For practical purposes, we focus on low-pass filters \mathcal{G} which are normalized, such that $\mathcal{G}c = c$ for any constant field c on Ω . Vreman [90] showed that any normalized filter is conservative if the filter is self-adjoint, requiring the filter kernel to be symmetric in its arguments, i.e. requiring $K_G(x, \xi) = K_G(\xi, x)$ (in this case, the filter operator is a self-adjoint operator in the Hilbert space of square integrable functions on the domain Ω [90]).

In numerical implementations, filters occur in a discrete form: either from a discretization of Eq. ((3.5)), or directly from a discrete formulation. Discrete filters are linear operators acting on vectors $\mathbf{f} \in \mathbb{R}^n$ with elements the values of $f(x)$ at all nodes in the computational domain. The filter is then expressed as a matrix multiplication

$$\bar{\mathbf{f}} = \mathbf{G}\mathbf{f}, \quad (3.6)$$

with $\mathbf{G} \in \mathbb{R}^{n \times n}$. Normalization, and conservation are now respectively defined as [90]

$$\mathbf{G} \mathbf{1} = \mathbf{1}, \quad (\text{normalization}) \quad (3.7)$$

$$\mathbf{1}^T \mathbf{G} = \mathbf{1}^T, \quad (\text{conservation}) \quad (3.8)$$

and $\mathbf{1} \in \mathbb{R}^n$ a vector with all elements equal to 1. It is now readily seen that for discrete filters, a normalized filter is conservative if

$$\mathbf{G} = \mathbf{G}^T, \quad (3.9)$$

i.e., if the filter matrix \mathbf{G} is symmetric (in this case \mathbf{G} is a self-adjoint operator in the vector space \mathbb{R}^n [90]).

In his work on self-adjoint filters, Vreman constructed a discrete conservative top-hat filter for one-dimensional non-uniform grids, both for internal points, and for points near a wall boundary. At internal points the filter coefficients correspond to

$$g_{i,j} = 0, \quad \text{for } |i - j| \geq 2, \quad \text{and} \quad (3.10)$$

$$g_{i,i-1} = \frac{\Delta_{i-1} + \Delta_i}{8\Delta_{i-1}\Delta_i}, \quad g_{i,i} = \frac{1}{4\Delta_i}, \quad g_{i,i+1} = \frac{\Delta_{i+1} + \Delta_i}{8\Delta_i\Delta_{i+1}}, \quad (3.11)$$

with $g_{i,j}$ elements of the filter matrix \mathbf{G} . It is appreciated that both normalization and conservation properties (Eqs. 3.7,3.8) are fulfilled. Near the boundary, the filter stencil becomes one-sided, and the coefficients need to be adapted. For a top-hat filter, only the first point (with index $i = 1$) is affected, and the coefficients are [90]

$$b_{1,1} = \frac{1 - g_{1,2}\Delta_2}{\Delta_1}, \quad g_{1,2} = \frac{\Delta_2 + \Delta_1}{8\Delta_1\Delta_2}, \quad (3.12)$$

where we use $b_{i,j}$ to denote the coefficients of \mathbf{G} which are adapted to account for the boundary, and do not correspond to coefficients used for internal points. As is appreciated, using this construction, the filter is conservative, and remains symmetric.

3.3 Construction of high-order conservative boundary filters

For the construction of the conservative boundary filters, we restrict ourselves in the current work to orthogonal grids, where the filter is constructed by

successively applying 1D filters in three directions. Equation (3.6) is then formulated as a 1D filter. Written out for an internal node i this corresponds to

$$(\mathcal{G}f)_i = \sum_{j=i-N}^{i+M} g_{i,j} f_j, \quad (3.13)$$

with $M + N$ the width of the stencil. The transfer function of this filter in spectral space is

$$G_i(k\Delta x_i) = \sum_{j=i-N}^{i+M} g_{i,j} \exp(\iota\beta_{i,j}k\Delta x_i), \quad (3.14)$$

where $\beta_{i,j} = (x_j - x_i)/\Delta x_i$, and Δx_i the mesh size at location x_i , and $\iota = \sqrt{-1}$ the imaginary unit. As in Refs. [48, 83, 3, 2] we consider uniform grids, such that $\Delta x_i = \Delta x$, and $\beta_{i,j} = j - i$. Moreover, for internal points, filters are symmetric, and $M = N$. In that case $g_{i,j}$ becomes independent of the position i of the internal point. For simplicity of notation we will drop the index i in this case, i.e. for internal points and symmetric stencils, we use the notation $g_k = g_{i,i+k} = g_{i,i-k}$.

For the construction of filters at the internal points, the filter coefficients are determined by imposing a number of constraints on the filter transfer function [48, 83, 3]. Firstly, normalization (3.7) leads to $G(0) = 1$. Secondly, the filters are constructed to remove π -modes, which corresponds to $G(\pi) = 0$. Hence, using Eq. ((3.14)), and for equidistant meshes, these two constraints lead to

$$\sum_{j=i-N}^{i+M} g_{i,j} = 1, \quad (3.15)$$

$$\sum_{j=i-N}^{i+M} (-1)^{j-i} g_{i,j} = 0. \quad (3.16)$$

Depending on the width of the filter stencil, a number of additional constraints is imposed. These may include the desired order of the filter, or the selectivity of the filter in only removing high-wavenumber content of the signal [48, 83, 3]. In particular, to impose the filter to be of order m , a total of $m - 1$ additional constraints need to be satisfied, corresponding to [48, 83, 3]

$$\sum_{j=i-N}^{i+M} (j - i)^p g_{i,j} = 0; \quad p = 1, \dots, m - 1. \quad (3.17)$$

For boundary filters, Berland *et al.* [2] used similar constraints to construct one-sided filters. Their focus was also on local accuracy of the filters, but

Table 3.1: The constraints imposed in each boundary point of the 11-point matching conservative boundary filter

Type of constraint:	π -mode	Normalization	Accuracy
1 st point (from the wall)	no	yes	2 nd order
2 nd point	no	yes	2 nd order
3 rd point	yes	yes	2 nd order
4 th point	yes	yes	3 rd order
5 th point	yes	yes	4 th order

In case of an 11-point stencil as in Eq. (3.18), 15 coefficients $b_{i,j} = b_{j,i}$ need to be determined, requiring 15 linearly independent constraints on these coefficients. We found that imposing as a minimum, normalization and second-order accuracy in all points (i.e. for all rows in the matrix \mathbf{G}) does not allow for the π -mode constraint in the first two points (first two rows) of the filter scheme. In particular, imposing the normalization constraints, and second-order constraints in addition to π -mode constraints in the first two points leads to a system which is inconsistent (i.e. the rank of the augmented matrix is larger than that of the system matrix). When the π -mode requirement is lifted for the first two points nearest to the boundary, solutions exist. Similar problems with the π -mode constraint were found for 7-point, 9-point, and 13-point stencils. For the 11-point stencil, an overview of the constraints which lead to a satisfactory solution are shown in Table 3.1. The attentive reader will note that the table lists 16 constraints (for 15 unknowns). As a result of the symmetry of the coefficients, we found that the constraints imposing 2nd order accuracy in the boundary points are linearly dependent, such that one second-order constraint comes for free.

We now turn to an evaluation of the spectral properties of the 11-point conservative boundary filter in Fig. 3.1. To this end, the dissipative properties of the filter are investigated, by displaying $\|1 - G_i(k\Delta x)\|$ in the five points closest to the boundary. As a point of reference, the boundary filters of Berland *et al.* [2] are also plotted. It is appreciated that the dissipation of the filters in the low wavenumber range is kept at a very low level, which is required to allow for accurate CAA simulations while using the filter to remove π -modes. As discussed above, for the conservative filters, the π -mode constraint is not imposed in the first two grid points, and this is clearly visible in Fig. 3.1(b) and (c), where the dissipation level of the conservative filter does not reach one for $k\Delta x = \pi$. When comparing the selectivity of the new conservative filter with Berland *et al.* original boundary filter, it is appreciated that the conservative filter performs remarkably well. Only in the second and third

point, the conservative filters are less selective in the low-wavenumber range.

Nine-point and 13-point matching conservative boundary filters are derived in a similar way. The dissipation level of these filters are shown in Fig. 3.2 and the coefficients of the 9-point, 11-point, and 13-point matching conservative boundary filters are shown respectively in Table A.2, A.3, and A.4, provided in the Appendix A.

3.4 Numerical results

We now turn to the evaluation of conservative boundary filters in simulations. Large-eddy simulations are performed using a VMS Smagorinsky subgrid-scale model formulated as Eq. (2.28). The coefficients β , γ_0 and γ_β , are calculated at every grid point. In the case of channel flow, these coefficients are constant across the wall-parallel planes and only varies in the wall-normal direction; nevertheless, they are different from point to point for the case of 2D cavity. In this work, the coefficients are firstly calculated at every grid point in the cavity, and a mean value for each coefficient is then taken via simple average for all the cells across the computational domain.

This section is structured as follows. First, in §3.4.1, channel-flow simulations are presented, and the effect of conservative filtering on VMS subgrid-scale modeling, and on removing π -modes is elaborated. Next, in §3.4.2, 2D cavity simulations are presented, and the importance of conservative filtering for removal of π -modes is illustrated for the correct prediction of the flow pattern, and the corresponding cavity Strouhal number.

3.4.1 Channel flow

The Reynolds number based on friction velocity, $Re_\tau=300$. The corresponding Reynolds number based on the mean stream-wise velocity is approximately 10^4 . As a point of reference LES results are compared with the DNS data which are obtained from Ref. [35]. Simulations are conducted using the in-house compressible code FLOWAVE; the Mach number has been set to 0.2, such that the effect of compressibility is negligible.

In first instance, the effect of conservative filter formulations on the VMS Smagorinsky model is investigated (cf. also the discussion in §3.1). To construct the high-pass filter required for the VMS model, we either use the conservative low-pass top-hat filter of Vreman (cf. Eq. 3.12), or a standard non-conservative version discretized with the trapezoidal integration rule. An overview of the

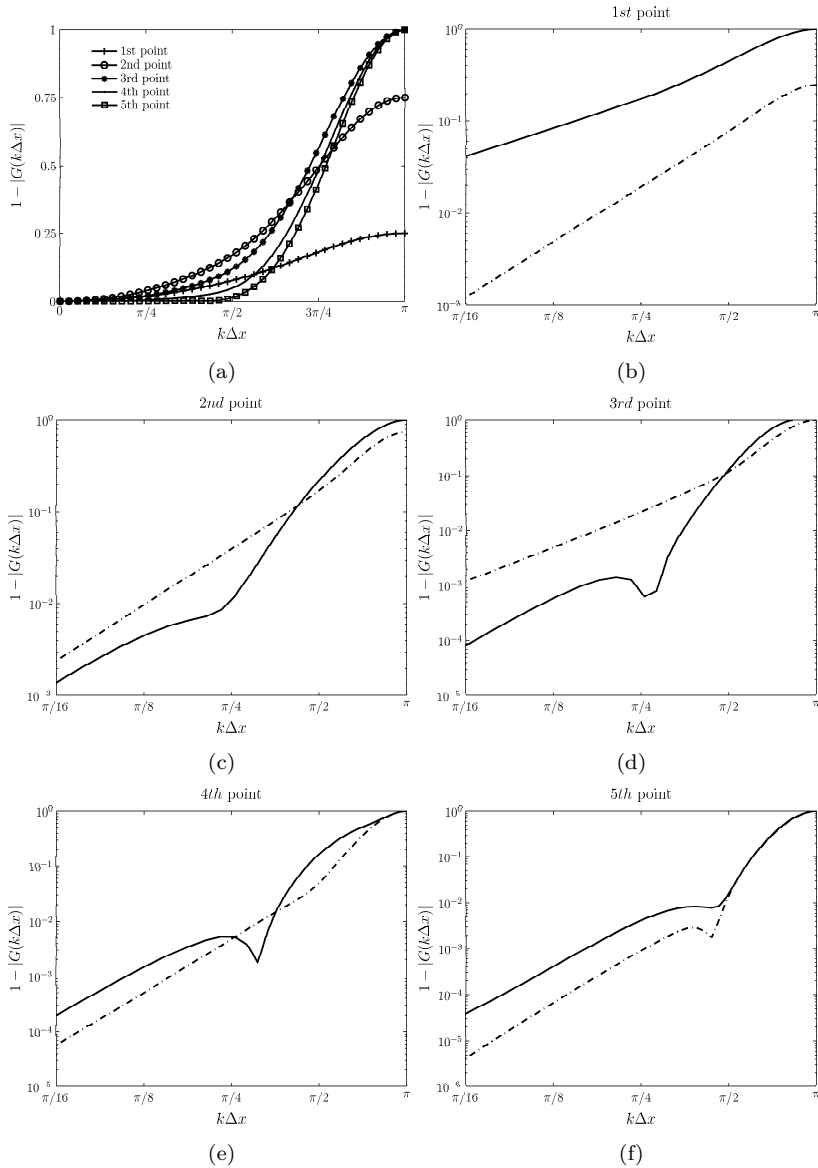


Figure 3.1: Dissipation of the 11-point matching conservative filters and Berland *et al.*'s [2] 11-point boundary filters. (a) The dissipation of the conservative boundary filters, and (b)-(f) the comparison of the dissipation of the conservative filters and Berland *et al.*'s filters at the first five points from the wall. Solid line: Berland *et al.*'s boundary filters; dashed line: conservative boundary filters.

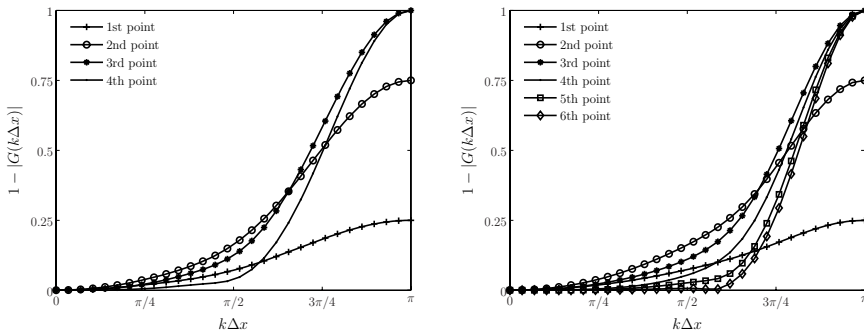


Figure 3.2: The dissipation of the 9-point (left) and 13-point (right) matching conservative boundary filters

Table 3.2: Overview of channel flow test cases used to test the filtering of the VMS model

Case	Grid	SGS model	Filtering in the SGS model
1	Coarse mesh, $64 \times 64 \times 64$	No model	/
2	Coarse mesh, $64 \times 64 \times 64$	VMS	2D filtering
3	Coarse mesh, $64 \times 64 \times 64$	VMS	3D conservative formulation
4	Coarse mesh, $64 \times 64 \times 64$	VMS	3D non-conservative formulation
5	Fine mesh, $96 \times 128 \times 96$	No model	/
6	Fine mesh, $96 \times 128 \times 96$	VMS	3D conservative formulation

different simulations carried out to test the VMS filtering is given in Table 3.2. Two different grids are included (denoted as ‘coarse’ and ‘fine’). For the coarse mesh, four different cases are considered: (1) a no-model case, (2) a case with 2D wall-parallel filtering (as often used for channel-flow LES in the past), (3) a case with a 3D conservative formulation of the filtering, and (4) a non-conservative formulation (similar to the case discussed in Ref. [79]). For the coarse mesh, only a no-model simulation, and VMS using a conservative formulation of the filtering are performed.

In Fig. 3.3(a), the mean stream-wise velocity profiles are shown for the different cases listed in Table 3.2. The velocity is normalized using the friction velocity predicted by the LES simulations. It can be seen that the result obtained from the 3D non-conservative formulation deviates strongly from the DNS data. The velocity and friction velocity near the wall are not correctly predicted due to the failure of this formulation in satisfying $\tau_{M,w} = 0$ (cf. discussion in §3.1), leading to an deviation which is even bigger than that of the no-model simulations. The result with the 3D conservative formulation of the VMS filters matches the

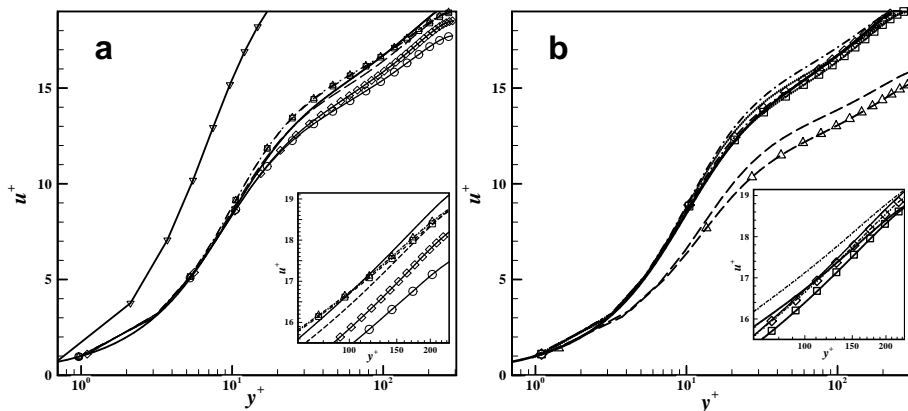


Figure 3.3: Mean stream-wise velocities of the channel-flow testing. (a) Obtained by applying various conservative or non-conservative top-hat filters in the VMS model. (—): DNS reference data [35]; (—○): no-model simulation on the coarse mesh; (—◇): no-model simulation on the fine mesh; (—□): LES simulation on the coarse mesh with filtering applied in wall-parallel directions; (—·△): LES simulation on the coarse mesh with conservative filtering applied in three directions; (—▽): LES simulation on the coarse mesh with non-conservative filtering applied in three directions; (—): LES simulation on the fine mesh with conservative filtering applied in three directions. (b) Obtained by applying various high-order filters to remove odd-even decoupling. (—): DNS reference data; (···): LES simulation on the coarse mesh without spatial filtering; (—): LES simulation on the coarse mesh with Berland *et al.*'s filters [2]; (—·◇): LES simulation on the coarse mesh with conservative filters; (···□): LES simulation on the fine mesh without spatial filtering; (—△): LES simulation on the fine mesh with Berland *et al.*'s filters; (—·): LES simulation on the fine mesh with conservative filters.

DNS data very well, and also corresponds closely with results obtained using 2D filtering. It is appreciated that also on the coarse mesh, the 3D conservative formulation yields satisfactory results.

Second-order turbulent statistics are shown in Fig. 3.4. The results are not significantly different from each other, except that conservative filtering applied in three directions produces the best match with the DNS results, especially for the $\langle u'v' \rangle^+$ and $\langle v'v' \rangle^+$.

We now turn to the use of filters to remove odd-even decoupling or so-called π -modes. The use of top-hat filters is not appropriate for this, since they are

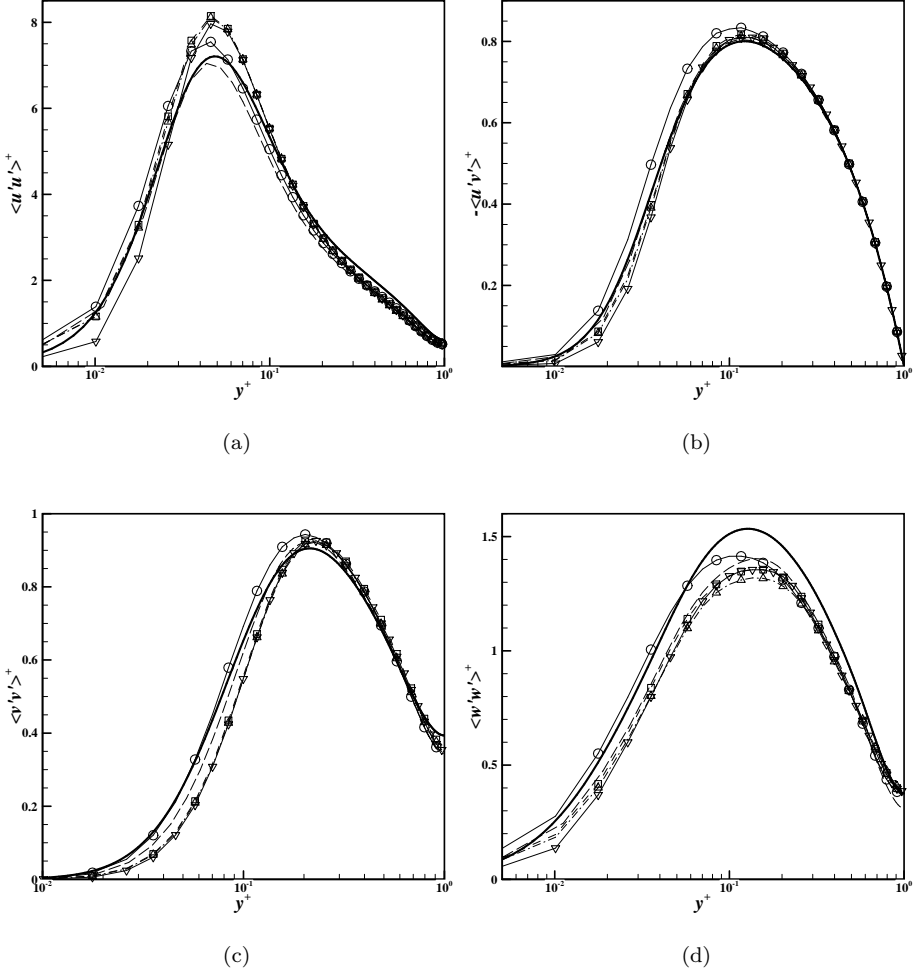


Figure 3.4: Second-order turbulent statistics obtained by applying various conservative or non-conservative top-hat filters in the VMS model: (a) $\langle u'u' \rangle^+$, (b) $\langle u'v' \rangle^+$, (c) $\langle v'v' \rangle^+$ and (d) $\langle w'w' \rangle^+$. (—): DNS reference data [35]; (—○): no-model simulation on the coarse mesh; (—□): LES simulation on the coarse mesh with filtering applied in wall-parallel directions; (—·△): LES simulation on the coarse mesh with conservative filtering applied in three directions; (—▽): LES simulation on the coarse mesh with non-conservative filtering applied in three directions; (—): LES simulation on the fine mesh with conservative filtering applied in three directions.

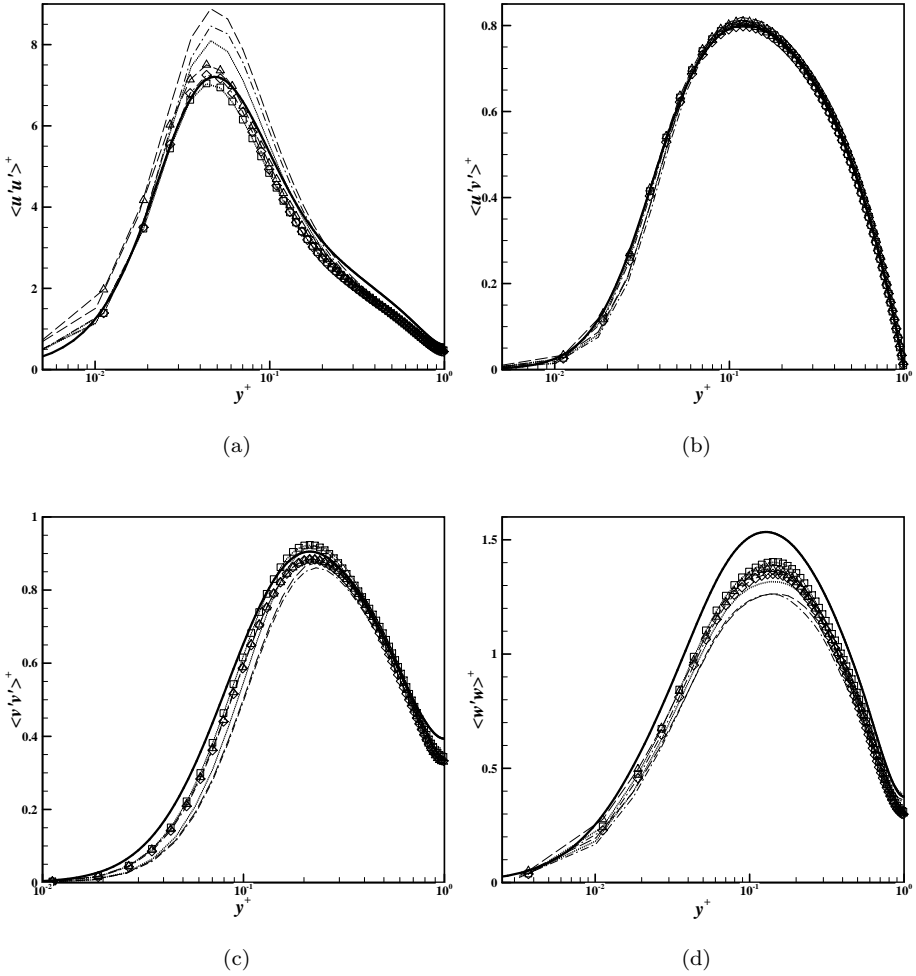


Figure 3.5: Second-order turbulent statistics obtained by applying various high-order filters to remove odd-even decoupling: (a) $\langle u'u' \rangle^+$, (b) $\langle u'v' \rangle^+$, (c) $\langle v'v' \rangle^+$ and (d) $\langle w'w' \rangle^+$. (—): DNS reference data; (···): LES simulation on the coarse mesh without spatial filtering; (—): LES simulation on the coarse mesh with Berland *et al.*'s filters [2]; (— · ◇): LES simulation on the coarse mesh with conservative filters; (··· □): LES simulation on the fine mesh without spatial filtering; (— · △): LES simulation on the fine mesh with Berland *et al.*'s filters; (— ·): LES simulation on the fine mesh with conservative filters.

Table 3.3: Channel-flow cases used to test the use of spatial filters for removal of odd-even decoupling

Case	Grid	Spatial 11-point filtering
1	Coarse mesh, $64 \times 64 \times 64$	/
2	Coarse mesh, $64 \times 64 \times 64$	non-conservative filter [2]
3	Coarse mesh, $64 \times 64 \times 64$	conservative filter
4	Coarse mesh, $64 \times 64 \times 64$	/
5	Fine mesh, $96 \times 128 \times 96$	non-conservative filter [2]
6	Fine mesh, $96 \times 128 \times 96$	conservative filters

Table 3.4: Errors induced by use of conservative, and Berland *et al.*'s filters on stretched grids

Error on:	mass-flow rate	friction velocity
Coarse mesh + non-conservative filter	4%	27%
Coarse mesh + conservative filters	2%	0.5%
Fine mesh + non-conservative filter	5%	30%
Fine mesh + conservative filters	1%	0.2%

not sufficiently selective in only removing the π -modes, and not the large scales in the simulations. Hence, instead, we focus on the high-order conservative filters developed in §3.3, and use an 11-point filter to remove π -modes in the simulations at every time step. For the subgrid-scale model, a VMS model with conservative formulation is used. Table 3.3 summarizes the test cases involved.

Looking at velocity fields for all test cases, we find that both Berland *et al.*'s filters and conservative filters are effective in removing odd-even decoupling (results not shown here). However, by evaluating the mean stream-wise velocity of the different cases in Fig. 3.3(b), we observe a large disparity between the conservative filters and non-conservative filters. It is appreciated that the use of non-conservative filter formulation seriously under-predicts the mean velocity; on the contrary, the results of conservative filtering differ little from the DNS data.

In the current channel-flow simulations, the computational grid is stretched in the wall normal direction. with maximum stretching ratios of 10.5% and 3.2% for the coarse mesh and the fine mesh respectively. For the implementation of the conservative filter, we did not take this stretching into account, but straightforwardly use the filters derived in §3.3. Hence, on these stretched grids, these filters are formally not conservative, but we found the errors to be small,

as listed in Table 3.4. It is appreciated that even for a rather high stretching ratio of 10% on the coarse grid, the error induced by using the conservative filters on stretched grids remains small ($< 2\%$).

Finally, the predicted second-order turbulent statistics are then shown in Fig. 3.5. It is difficult to reach a conclusion based on the plots: both the non-conservative filters on the coarse mesh and the conservative filters on the fine mesh produce the largest errors, while the results from the non-conservative filters on the fine mesh and the conservative filters on the coarse mesh show smaller deviations from both the DNS results and the results without any filtering. Overall, the non-conservative and conservative filters yield comparable second-order statistics. This is not unexpected since the conservative filtering technique is designed to remove the odd-even decoupling and keep the main flow structure unchanged, while the second-order statistics is not on the goal list.

3.4.2 2D cavity flow

We now turn to a 2D cavity flow, and investigate the possible influence of the filter formulation for removing π -modes, on noise predictions. The noise radiated by flow passing over cavities has been studied extensively in the past and is connected to a broad range of aerospace and automotive applications, and a variety of theoretical questions on noise production. Extensive amount of data found in literature for 2D cavity flows [24, 72, 80]. The numerical studies of 3D cavity flows came relatively late compared with the studies of the 2D cavity flows, can be found in [76, 45, 44, 43].

The spectrum of cavity noise contains both broadband components introduced by the turbulence in the shear layer, and tonal components. In 2D cavities, the mechanisms for the intense tonal components in cavities have been identified and can be either [72]

1. a shear-layer mode mechanism in which the shear-layer generated at the upstream edge of the cavity impinges on the rear edge of the cavity, scattering acoustic waves that propagate upstream and further excite the shear layer, or
2. a wake-mode mechanism, induced by periodical vortex shedding at the cavity leading edge and characterized by the shedding of a single vortex which occupies all the cavity and overshadows the role of the smaller-scale vortices of the separated shear layer.

However, the presence of a wake mode is not seen in experiments of compressible cavity flows, nor in the studies of 3D cavities. To investigate higher Reynolds

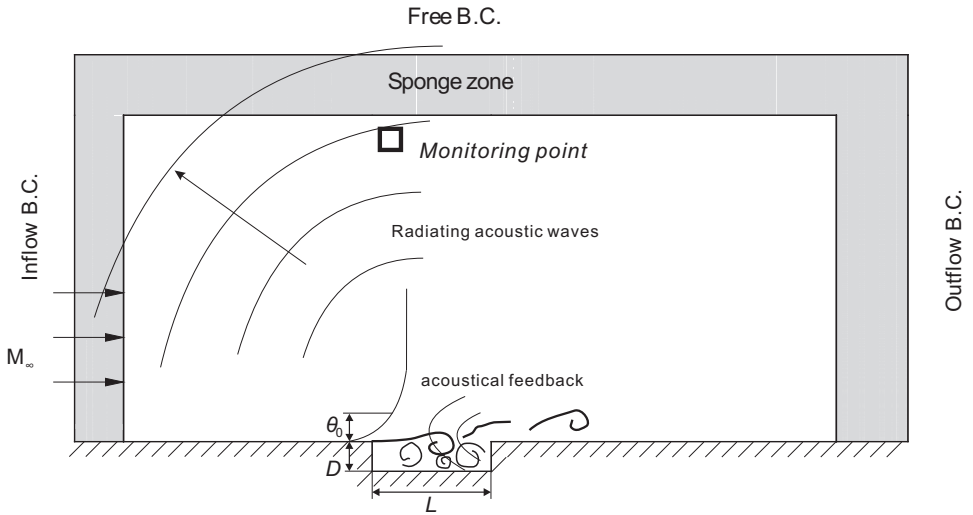


Figure 3.6: Cavity configuration

numbers, Shieh and Morris studies 2D cavities using hybrid URANS/LES [75] and observed a transition to a wake mode; however, a subsequent 3-D study [76] did not show a wake mode transition for the same configurations, indicating that it could be related to the 2-D behaviour.

The dynamics of the incoming boundary layer has an very important effect for the downstream flow pattern. The thickness of the boundary layer was recognized as a determinant factor for the mode selection. As shown by [23], the ratio L/θ participates to the mode selection. Moreover, the simulations of 2D cavities showed a transition toward the wake mode when the ratio of the cavity length over the momentum thickness L/θ became large. Rowley [72] suggested three-dimensional effects may reduce the overall amplitude of oscillations, which would inhibit transition to wake mode.

The 2D cavity is chosen as a validation case of the conservative filtering and to illustrate of the importance of the conservative filtering, not only because it is cheaper and simpler, but also because the unique wake mode exists and the mode selection is sensitive to the incoming boundary layer thickness. In reality, the filtering is not applied at every time step. In this study the extreme case of the non-conservative filter being applied at every time step is explored just to show the potential consequence on noise generation caused by the non-conservative filtering. As will be shown later, the mean velocity profiles at the inner layer upstream of the 2D cavity is changed, which in turn changes the

mode selection in the 2D cavity, leading to a quasi-wake mode.

However, though this study is not intended to discover new physics in cavity flows, one should be aware that in 3D cavities the flow physics are different and the thickness of the incoming boundary layer will not lead to a mode transition as dramatic as the change in 2D cavities. Hence the potential effect of non-conservative filtering in 3D cavity simulations may be significantly lower.

In the current simulations, we focus on the shear-layer mode in a 2D cavity. Frequency of tonal noise in the shear-layer mode can be estimated by an empirical expression, originally introduced by Rossiter [71]:

$$St = \frac{fL}{U_\infty} = \frac{n - \alpha}{M + 1/\kappa} \quad (3.22)$$

where St (Strouhal number) is the dimensionless frequency, f is the frequency, L is the length of the cavity, U_∞ is free stream velocity, n is the mode number, M is undisturbed Mach number, κ and α are empirical constants. The values for κ and α are obtained experimentally and equal to 0.57 and 0.25 respectively for the cavity studied in present research.

We consider a 2D cavity corresponding to the DNS cavity case of Gloerfelt [24]. The configuration of the cavity is shown in Fig. 3.6. Its length-to-depth ratio is $L/D = 4$, and the free-stream Mach number is $M = 0.5$. The Reynolds number based on the depth of the cavity corresponds to 4800 and the ratio $L/\theta = 63$, where θ is the initial boundary layer momentum thickness at the leading edge of the cavity. The sound field in this flow is dominated by the shear-layer mode which generates the dominant modes in the noise spectrum.

In current work, simulations with two different grids are included. A coarse mesh uses 101×51 points inside the cavity and 379×121 outside; a finer mesh uses 201×51 points inside the cavity and 679×221 outside. The computational domain extends over 13D vertically and 28D horizontally to include a portion of the radiated field. At the inlet, three velocity components and temperature are specified; at the outlet, the pressure is imposed. A free boundary condition is applied at the top boundary. In order to reduce spurious wave reflection at the outer boundaries, sponge zones are included at all boundaries, by using progressive damping terms towards the hard boundary of the mesh. To remove π -modes in the simulations, either an 11-point conservative filter, or Berland *et al.*'s filter is used at the final Runge–Kutta stage of every iteration. Simulations start from a Blasius laminar boundary layer along the wall and spanning the cavity. Computations are first run for a few hundred dimensionless time units until the oscillations in the shear layer are established. Subsequently, averaging in time is used over a sufficiently long time window for averaged quantities to statistically converge.

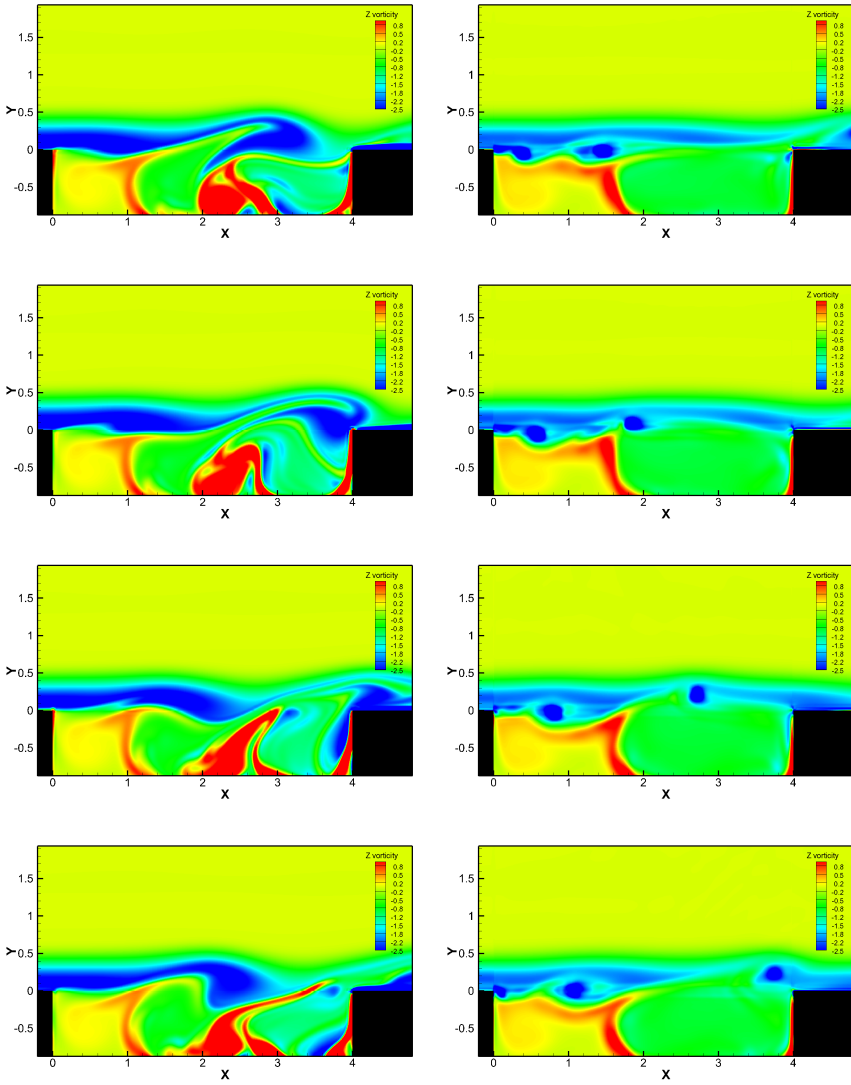


Figure 3.7: Vorticity fields during one cycle of oscillation (first Rossiter mode) obtained by the 11-point conservative filters (left) and non-conservative filters (right) on the fine mesh.

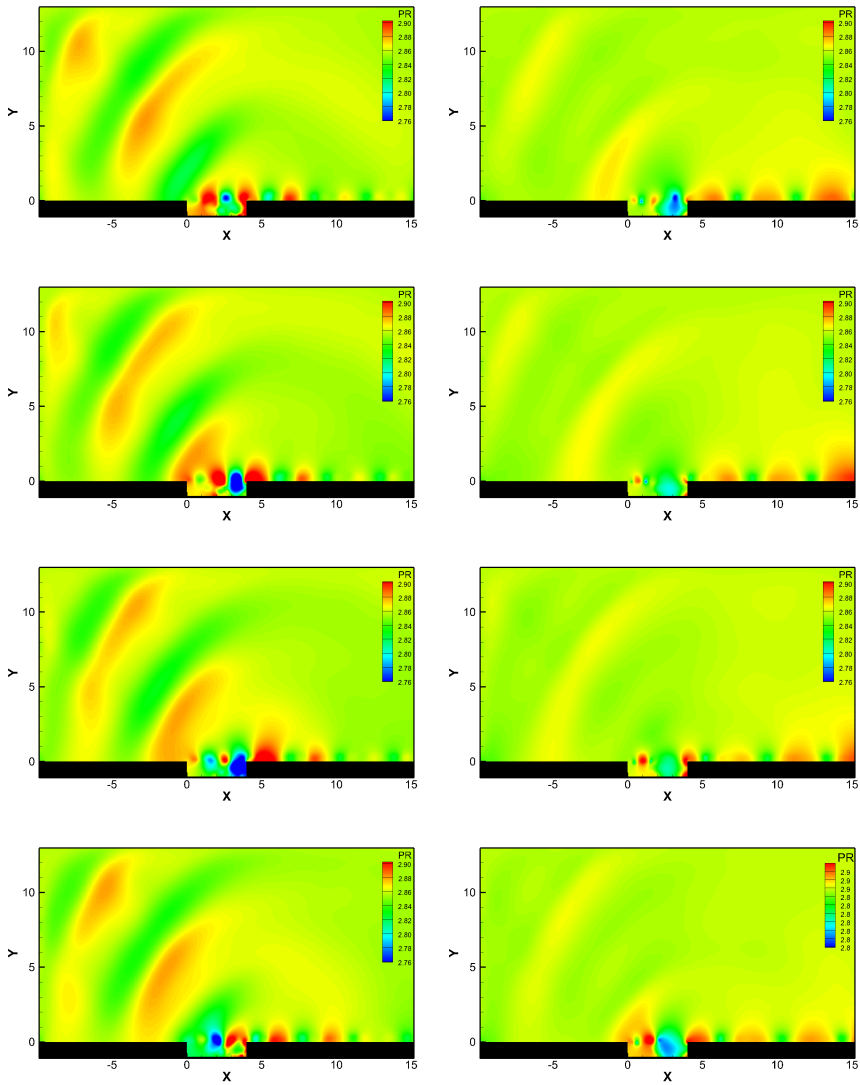


Figure 3.8: Pressure contours during one cycle of oscillation (first Rossiter mode) obtained by the 11-point conservative filters (left) and non-conservative filters (right) on the fine mesh.

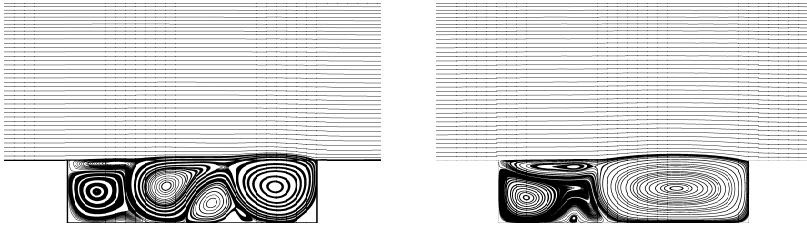


Figure 3.9: Time averaged streamlines on the fine mesh by the conservative filters (left) and Berland *et al.*'s filters (right).

Fig. 3.7 and 3.8 respectively show two instantaneous vorticity fields and pressure fields in one cycle of the dominant Rositer mode, obtained using an 11-point conservative filter (left), and Berland *et al.*'s original non-conservative formulation (right), both obtained on the fine mesh. It is appreciated that large differences exist between solutions obtained with both filter formulations. The structure of the conservative solution very much resemble the flow patterns found in the work of Gloerfelt [24, 25] associated to the shear-layer mode of the cavity. To further investigate the difference between solutions using either conservative or non-conservative filtering, streamlines associated with the time-averaged solution of both cases are presented in Fig. 3.9. It is appreciate that large differences exists; in particular the non-conservative case displays a big stationary vortex occupying the rear part of the cavity, which is more reminiscent of a wake-like cavity mode than of a shear-layer mode.

In Fig. 3.10 we investigate grid dependency of the solutions for both filter types, by looking at the pressure coefficient along the bottom cavity wall for the coarse and fine mesh. We find that the pressure coefficients for the conservative filters coincide for both grids (the respective lines are not distinguishable on the plot), and trends correspond well with pressure coefficients reported in the literature [24, 25]. The results of the non-conservative filter show a large variation when the grid is refined. For the finer grid, it is observed that the results using Berland's filters start approaching the solution found with conservative filters. This trend is to be expected, since even though Berland's filters are non-conservative, they still provide a consistent discretization of the governing equations, such that continued grid-refinement should eventually lead to an exact solution. However, it is appreciated for the current case, that much finer grid levels will be needed for this.

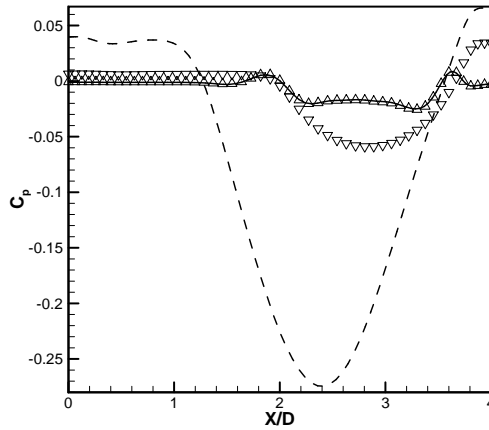


Figure 3.10: Mean pressure coefficient along the cavity bottom wall obtained by (—): the fine mesh and conservative filters, (— □): the fine mesh and Berland *et al.*'s filters, (— ○): the coarse mesh and conservative filters, (— □): the coarse mesh and Berland *et al.*'s filters.

In order to identify the dominant tonal frequencies of the noise, time signals are recorded at a point above the cavity with co-ordinate $(0.2D, 10D)$ (with respect to the leading edge of the cavity. See also Fig. 3.6). Fig. 3.11 shows the power spectral density of the fluctuating pressure recorded at the monitoring point for the different cases. The results obtained with the conservative filters display consistent features for both the coarse mesh and fine mesh, with dominant frequencies at $St = 0.185$, which is very close to the first Rossiter mode $St = 0.19$. This is also in line with the results reported in [24, 25] based on DNS. When looking at the results obtained with non-conservative filters, it is appreciated that the dominant frequencies depend strongly on the grid, and corresponds to $St = 0.15$ and $St = 0.23$ for the coarse and fine grid.

Up to this point, one might wonder why the flow patterns obtained from two different filtering techniques show such a big disparity. Here a tentative analysis is made, with a focus on the characteristic of the incoming boundary layer. The mean velocity profiles of the incoming boundary layer, rightly upstream of the cavity, are shown in Fig. 3.12. A notable difference can be observed between the mean velocity profiles obtained by the conservative filterings and those from the non-conservative filterings. The profiles obtained by the non-conservative filtering again show a dependency on the mesh resolution, while the results of the conservative filtering does not show such dependency. As already elaborated

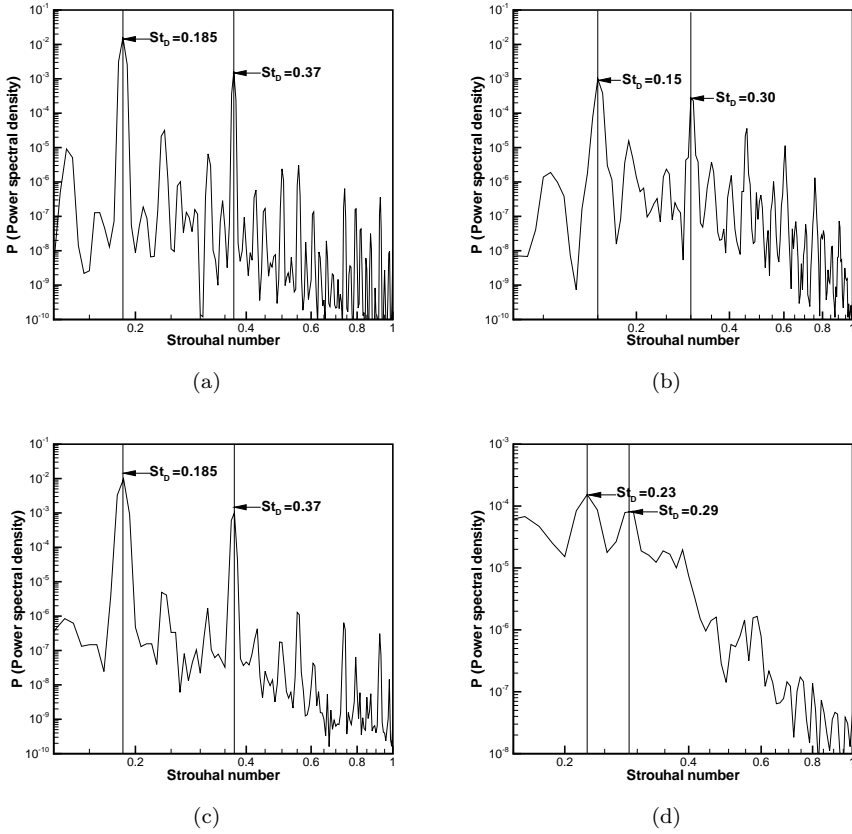


Figure 3.11: Power spectral density of fluctuating pressure versus the Strouhal number $St = fL/U_\infty$ at the position $(0.2D, 10D)$ by: fine mesh with conservative filters (a); fine mesh with Berland *et al.*'s filters (b); coarse mesh with conservative filters (c); coarse mesh with Berland *et al.*'s filters (d).

in previous paragraphs, the characteristic of the incoming boundary layer plays a decisive role in the mode selection. The quasi-wake modes resulting from the non-conservative filtering are probably due to the unphysical behavior of incoming boundary layer near the wall. The difference of PSDs for the non-conservative filtering on different mesh resolutions is possibly related to the disparity between their incoming mean velocities, as shown in Fig. 3.12. In addition to this, the effects of the filterings inside the cavity will also play an important role in the altering flow patterns and the PSDs.

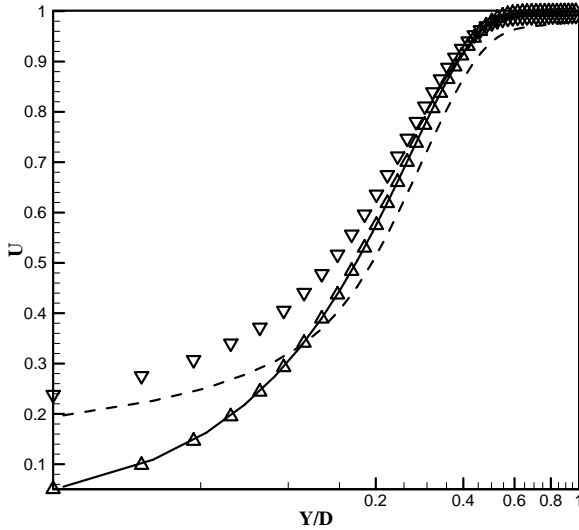


Figure 3.12: Mean velocity profile of the incoming boundary layer in a semi-logarithmic scale plot against the distance from the wall, obtained by the fine mesh and conservative filters (\triangle), the fine mesh and Berland *et al.*'s filters (∇), the coarse mesh and conservative filters (—), the coarse mesh and Berland *et al.*'s filters (—).

3.5 Conclusion

Globally conservative high-order filters were elaborated and used for LES simulations. Focus is on selective filters for removing odd-even decoupling in simulations. Nine-, eleven-, and thirteen-point stencils, and associated one-sided boundary schemes, were elaborated. Next to that, the importance of a conservative filter formulation for use in the VMS Smagorinsky subgrid-scale model was also highlighted. The conservative filtering technique developed in this chapter is mainly intended for structured mesh with a mild stretching ratio. It may be interesting for other numerical methods where explicit filtering is involved, such as the immersed boundary technique. For unstructured mesh, it is a lot more complicated and may not be practical.

In a first step, conservative filters were tested in channel-flow LES, and comparisons with simulations using Berland *et al.*'s non-conservative filters were presented. When using these filters to remove π -modes, it was demonstrated

that a conservative 11-point stencils leads to accurate results both on coarse and finer grids. When using a non-conservative formulation, large errors on the prediction of the skin friction were detected. We used the channel-flow test case also to test the effect of a conservative filter formulation in the formulation of the Smagorinsky model. Here, the use of a conservative top-hat filter, as proposed by Vreman [90], was compared to a traditional top-hat implementation. Again, we found that non-conservative formulations can lead to large errors; in this case errors up to 10% on the prediction of the friction velocity.

In order to investigate the effect of filter formulations (conservative or non-conservative), used for removing π -modes, on noise predictions in aeroacoustics applications, simulations of a 2D cavity flow were conducted. It was observed that simulations with the conservative boundary filters captured the flow pattern of shear-layer mode and the dominant frequencies correctly, while the simulations with non-conservative filter formulation failed to do so. It was observed for the non-conservative filters, that the flow structures at the incoming boundary layers are significantly changed, leading to entirely different recirculation patterns inside the cavity.

Chapter 4

A new self-adaptive Smagorinsky model: a solution to the log-layer mismatch

This chapter addresses one of most persisting problems in wall-modeled large eddy simulation (LES): the overshoot of the mean velocity gradient near the wall, which is referred to as ‘log-layer mismatch’ in some circumstances. An analysis of the relationship between turbulent kinetic energy budgets and mean velocity gradient is elaborated for both direct numerical simulations (DNS) and large eddy simulation (LES) of fully developed channel flows at high-Reynolds number. Based on the analysis, a self-adaptive Smagorinsky model for LES of high-Reynolds-number boundary layer flows is proposed, in which the Smagorinsky coefficient is dynamically adjusted so that a logarithmic mean velocity distribution is captured. The model is then implemented in a second-order finite-volume code, taking into consideration of discretization errors, and applied to a infinite-Reynolds-number channel flow. The desired logarithmic mean velocity distribution is correctly predicted. Finally in Section 4.5, the model is extended to account for viscous effects. The work discussed in this chapter is partially published in [96] and [95].

4.1 Introduction

In the current study we aim at clarifying the factors which influence the normalized mean-velocity gradient $\phi(y)$, and solving the issue of the overshoot of the mean velocity gradient. By reformulating the balance equation for turbulent kinetic energy, and combining with the mean momentum balance, we manage to find an explicit relation between $\phi(y)$ and turbulent dissipation and transport. In a first step, we illustrate this relation by evaluating the high-Reynolds-number DNS data base by Hoyas and Jiménez [30]. In a next step, a similar relation is derived for wall-modeled LES, in which effects of the subgrid-scale closure are included, and we show that this equation determines the velocity gradient in LES. Therefore, this relation can serve as a constraint to the subgrid-scale model in the logarithmic layer, and can, e.g., be used to ‘dynamically’ determine the Smagorinsky length scale near the wall. Moreover, issues related to numerical discretization are readily accounted for by considering the structure of the discrete kinetic energy equation implicated by the discretization. The model is then extended to include viscous effect. For practical elaboration, we concentrate on the case of a rough channel flow at infinite Reynolds number, and a set of smooth wall channel flow test cases, with DNS results [30] as reference. We illustrate the approach using second-order Smagorinsky LES in combination with the new near-wall closure model, and present simulation results in which the error on the normalized mean-velocity gradient largely remains below 5%, except very close to the wall, where errors are influenced by discretization.

4.2 Analysis of turbulent kinetic energy budgets and relation to mean shear

We focus in the current work on the high-Reynolds-number boundary-layer in a fully developed turbulent channel flow. This simplifies some of the equations, e.g., allowing for a simple force balance. However, a generalization to any type of high-Reynolds number boundary layer should be relatively straightforward. In a first step, in §4.2.1 the standard Navier–Stokes equations are used to derive a relation between normalized mean-velocity gradient, and dissipation and transport of turbulent kinetic energy. Results are verified using a DNS database. Next, in §4.2.2, we derive similar relations for large-eddy simulations, and show that subgrid-scale dissipation and transport are related to the normalized mean-velocity gradient. An evaluation of these different terms in Smagorinsky LES is discussed in §4.2.3.

4.2.1 Relation between energy budgets and mean velocity gradients in direct numerical simulation

Consider an incompressible turbulent channel flow with turbulent velocity $\mathbf{u} = \langle \mathbf{u} \rangle + \mathbf{u}'$, decomposed in its mean, and fluctuating part ($\langle \mathbf{u} \rangle$, and \mathbf{u}' , resp.). Cartesian coordinate directions x, y, z (also denoted as x_1, x_2, x_3) correspond to the stream-wise, normal, and span-wise directions. Velocity components in these directions are respectively u, v , and w , or also denoted as u_1, u_2 , and u_3 .

In a first step, we briefly review the momentum balance, as it is used later on. For fully developed turbulent channel flow, the axial momentum equation reduces to

$$0 = \frac{d}{dy} \left[-\langle u'v' \rangle + \nu \frac{d\langle u \rangle}{dy} \right] + f, \quad (4.1)$$

where $f = -(1/\rho)d\langle p \rangle/dx$ is the driving mean pressure gradient, and ν the kinematic viscosity. This relation is integrated from the wall to a height y , and using the boundary condition $\tau_w/\rho \equiv u_\tau^2 = \int_0^\delta f \, dy = f\delta$ for the total stress, to obtain

$$-\langle u'v' \rangle + \nu \frac{d\langle u \rangle}{dy} = u_\tau^2 - fy = f(\delta - y) \quad (4.2)$$

where δ is the boundary layer thickness (corresponding to the half-width of the channel in the fully developed case). Eq. (4.2) reflects the force balance in a fully developed channel flow. The sum of the viscous and turbulent shear stresses follows a linear distribution. Outside of the viscous sublayer and buffer layer, the viscous term is negligible, and the turbulent shear stress will follow a simple linear distribution.

To arrive at an expression for $\phi(y)$, we start from the turbulent kinetic energy equation. For fully developed channel flow, the turbulent kinetic energy equation corresponds to [67] (defining $q = u'_i u'_i / 2$, and $k = \langle u'_i u'_i \rangle / 2$)

$$0 = -\langle u'v' \rangle \frac{d\langle u \rangle}{dy} - \nu \left\langle \frac{\partial u'_i}{\partial x_j} \frac{\partial u'_i}{\partial x_j} \right\rangle + \nu \frac{d^2 k}{dy^2} - \frac{d}{dy} \langle qv' \rangle - \frac{1}{\rho} \frac{d}{dy} \langle v'p' \rangle. \quad (4.3)$$

The first term on the right-hand side is the production term, the second term is the pseudo-dissipation, the third term is the viscous diffusion, and the fourth and fifth terms represent turbulent convection and pressure transport respectively.

If we add and subtract the mean-flow viscous dissipation $\nu(\partial\langle u \rangle/\partial y)^2$ to Eq. (4.3), and reorganize some of the terms, we end up with following equation:

$$0 = \tilde{P} - \tilde{\epsilon} - T, \quad (4.4)$$

where

$$\tilde{P} = -\langle u'v' \rangle \frac{d\langle u \rangle}{dy} + \nu \frac{d\langle u \rangle}{dy} \frac{d\langle u \rangle}{dy} = (u_\tau^2 - fy) \frac{d\langle u \rangle}{dy}, \quad (4.5)$$

is a modified production term (further elaborated here using Eq. 4.2), and where

$$\tilde{\epsilon} = 2\nu \langle s'_{ij} s'_{ij} \rangle + \nu \frac{d\langle u \rangle}{dy} \frac{d\langle u \rangle}{dy} \quad (4.6)$$

with $s'_{ij} = (\partial u'_i / \partial x_j + \partial u'_j / \partial x_i) / 2$, combines the dissipation terms, i.e. turbulent dissipation, and mean-flow viscous dissipation. The last term on the right-hand side

$$T = \frac{d}{dy} \langle qv' \rangle + \frac{1}{\rho} \frac{d}{dy} \langle v'p' \rangle - \nu \frac{d^2 k}{dy^2} - \nu \frac{d^2 \langle v'v' \rangle}{dy^2} \quad (4.7)$$

is a transport term, representing turbulent diffusion, pressure transport, and viscous diffusion.

By multiplying Eq. (4.4) with $y\kappa[fu_\tau(\delta - y)]^{-1}$, and further using Eq. (4.5), we finally obtain

$$\phi(y) \equiv \frac{y\kappa}{u_\tau} \frac{d\langle u \rangle}{dy} = \frac{y\kappa}{u_\tau(u_\tau^2 - fy)} (\tilde{\epsilon} + T), \quad (4.8)$$

which relates the normalized mean-velocity gradient $\phi(y)$ to dissipation and transport terms in the kinetic energy equation.

We now evaluate the terms contributing to $\phi(y)$ based on the DNS database of Hoyas and Jiménez [30] with $Re_\tau = 550, 950$ and 2000 . Results are shown in Fig. 4.1 both in inner and outer scaling. It is appreciated from the figure that contributions of the mean-flow dissipation, the turbulent dissipation, and the transport terms add up to the normalized mean-velocity gradient. Moreover, between $y^+ = 50$ and $y/\delta = 0.2$, the normalized mean-velocity gradient is approximately one, indicating the logarithmic region. In this region the dominant term is the turbulent dissipation term, while effects of the transport remain below 10%, and mean-flow dissipation is negligible (only close to the wall, $y^+ < 30$, the latter plays an important role).

4.2.2 Relation between energy budgets and mean velocity gradients in large-eddy simulation

Inspired by the analysis of the DNS data and the terms contributing to ϕ , we now conduct a similar analysis for ϕ in large-eddy simulations based on the resolved turbulent kinetic energy equation. The resolved LES velocity

⁰cf. also <http://torroja.dmt.upm.es/ftp/channels/data/>

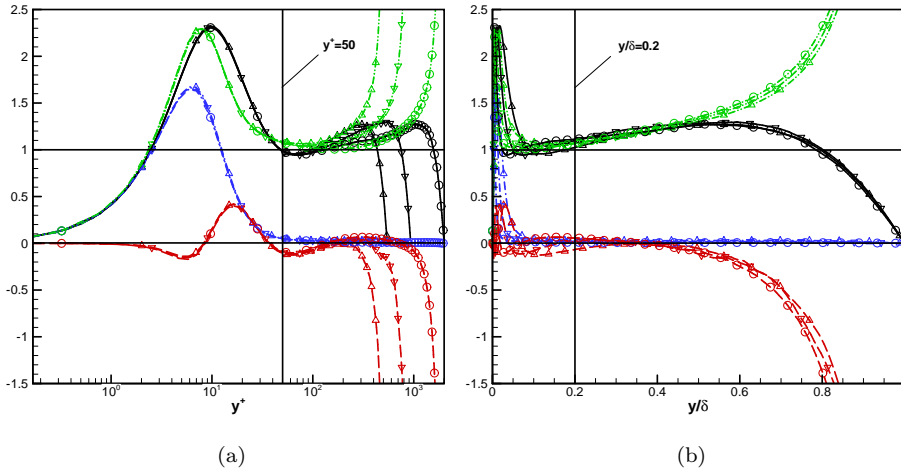


Figure 4.1: The contributions to $\phi(y)$ according to Eq. (4.8) in DNS of full developed turbulent channel (database by Hoyas and Jiménez [30]), in inner scaling (left) and outer scaling (right). Symbols, (o): $Re_\tau = 2003$, (\diamond): $Re_\tau = 950$, (Δ): $Re_\tau = 550$. Lines, (—, black): $\phi(y)$. Further, all multiplied with $y\kappa/[u_\tau(u_\tau^2 - fy)]$, (- · - ·, blue): mean-flow viscous dissipation; (- · · - ·, green): total dissipation (mean-flow + turbulent); (- - -, red): transport terms.

$\bar{\mathbf{u}} = \langle \bar{\mathbf{u}} \rangle + \bar{\mathbf{u}}'$, decomposed in its mean $\langle \bar{\mathbf{u}} \rangle$, and (resolved) fluctuating part $\bar{\mathbf{u}}'$. Further the subgrid-scale stresses are modeled with a subgrid-scale model $\tau_{M,ij} = \langle \tau_{M,ij} \rangle + \tau'_{M,ij}$, similarly decomposed into a mean and fluctuating part (note that, depending on the formulation of model, the mean part may be zero).

We consider a turbulent channel flow at infinite Reynolds number, and hence neglect resolved effects of viscosity. As for the DNS case, we first express the integrated momentum balance for the LES case, which corresponds to

$$-\langle \bar{u}'v' \rangle - \langle \tau_{M,12} \rangle = u_\tau^2 - fy = f(\delta - y). \quad (4.9)$$

Next, the resolved turbulent kinetic energy equation (defining $\bar{q} = \bar{u}'_i \bar{u}'_i / 2$, and $\bar{k} = \langle \bar{u}'_i \bar{u}'_i \rangle / 2$) for the LES case yields

$$0 = -\langle \bar{u}'v' \rangle \frac{d\langle \bar{u} \rangle}{dy} + \left\langle \tau'_{M,ij} \frac{\partial \bar{u}'_i}{\partial x_j} \right\rangle - \frac{d}{dy} \langle \tau'_{M,j2} \bar{u}'_j \rangle - \frac{d}{dy} \langle \bar{q}v' \rangle - \frac{1}{\rho} \frac{d}{dy} \langle \bar{v}'p' \rangle. \quad (4.10)$$

The first term on the right-hand side corresponds to the production of resolved turbulent kinetic energy, the second term is the SGS dissipation, the third

term is the SGS diffusion, and the fourth and fifth terms represent turbulent convection, and pressure transport.

We now add and subtract the mean-flow SGS dissipation $\langle \tau_{M,12} \rangle d\langle u \rangle / dy$ to Eq. (4.10), and reorganize the balance equation into

$$0 = \tilde{P}_{LES} - \tilde{\epsilon}_{LES} - T_{SGS} - T_{RES}, \quad (4.11)$$

where

$$\tilde{P}_{LES} = -\langle \bar{u}' \bar{v}' \rangle \frac{d\langle \bar{u} \rangle}{dy} - \langle \tau_{M,12} \rangle \frac{d\langle \bar{u} \rangle}{dy} = (u_\tau^2 - fy) \frac{d\langle \bar{u} \rangle}{dy}, \quad (4.12)$$

is the modified production term (further elaborated using Eq. 4.9), and where

$$\tilde{\epsilon}_{LES} = -\left\langle \tau'_{M,ij} \frac{\partial \bar{u}'_i}{\partial x_j} \right\rangle - \langle \tau_{M,12} \rangle \frac{d\langle \bar{u} \rangle}{dy} \quad (4.13)$$

include the dissipation terms, i.e., the turbulent SGS dissipation, and the mean-flow SGS dissipation. Finally, the subgrid-scale transport term, and the resolved turbulent transport terms respectively correspond to

$$T_{SGS} = \frac{d}{dy} \langle \tau'_{M,j2} \bar{u}'_j \rangle, \quad T_{RES} = \frac{d}{dy} \langle q \bar{v}' \rangle + \frac{1}{\rho} \frac{d}{dy} \langle \bar{v}' \bar{p}' \rangle. \quad (4.14)$$

Further reorganizing the terms, we obtain

$$\bar{\phi}(y) \equiv \frac{y\kappa}{u_\tau} \frac{d\langle \bar{u} \rangle}{dy} = \frac{y\kappa}{u_\tau(u_\tau^2 - fy)} (\tilde{\epsilon}_{LES} + T_{RES} + T_{SGS}), \quad (4.15)$$

which identifies the contributions to the normalized mean-velocity gradient $\bar{\phi}(y)$ in large-eddy simulations.

4.2.3 Evaluation of terms contributing to the normalized mean-velocity gradient in conventional wall-modeled Smagorinsky LES

The different terms in Eq. (4.15) are now evaluated based on a set of large-eddy simulations of a turbulent channel flow using conventional Smagorinsky LES. A rough wall with roughness $y_0/\delta = 10^{-4}$ is considered, and the Reynolds number is selected to be infinite (hence all turbulent dissipation is modeled by the subgrid-scale model). Simulations are performed using the second-order compressible Navier–Stokes solver FLOWAVE,[73, 94] operated at a Mach number of 0.2, such that effects of compressibility are negligible. Discretization

relies on a second-order finite-volume method combined with fourth-order Runge-Kutta time integration. The computational box size corresponds to $2\pi \times 1 \times \pi$ in stream-wise, wall-normal and span-wise directions respectively, and periodic boundary conditions are used in stream and span-wise directions. For discussion in the current subsection, all simulations are performed on a $64 \times 48 \times 64$ mesh.

At the wall, we use the conventional wall-stress model of Moeng, [61] but slightly adapted following Bou-Zeid *et al.*, [4] i.e., in Eq. (2.58), additionally filtered velocities $\bar{\bar{u}}_i$ are used instead of \bar{u}_i , such that the size of the mean stress is not overestimated. We use a running time average with a filter length of around $3.3\delta/U_c$, where U_c is the mean center-line velocity.

The subgrid-scale model corresponds to the conventional Smagorinsky model, i.e.

$$\tau_{M,ij} = -2l_s^2 |\bar{S}| \bar{S}_{ij}, \quad (4.16)$$

with $\bar{S}_{ij} = (\partial\bar{u}_i/\partial x_j + \partial\bar{u}_j/\partial x_i)/2$ the filtered rate-of-strain tensor, and $|\bar{S}| = (2\bar{S}_{ij}\bar{S}_{ij})^{1/2}$ its magnitude. Far away from the wall, in the center of the channel, the Smagorinsky length $l_s = C_s\Delta$, with $\Delta = (\Delta_1\Delta_2\Delta_3)^{1/3}$ the grid spacing, and C_s the Smagorinsky coefficient. To reduce the Smagorinsky length scale close to the wall, we employ Mason and Thomson's wall damping, [54] i.e.,

$$\frac{1}{l_s} = \frac{1}{C_s\Delta} + \frac{1}{\kappa y}, \quad (4.17)$$

such that close to the wall, Prandtl's mixing length $l_s = \kappa y$ is recovered.

In Fig. 4.2 simulation results are shown for two different values of the Smagorinsky coefficient, i.e. $C_s = 0.10$, and $C_s = 0.17$. The first is often used in wall-modeled LES (empirically tuned), while the second corresponds to Lilly's classical estimate for the coefficient, [50] i.e., $C_s = (3C_K/2)^{-3/4}/\pi \approx 0.17$ (taking a Kolmogorov constant $C_K = 1.6$). It is appreciated from the figure that the main contributions to the normalized mean-velocity gradient come from the subgrid-model contributions, while effects of resolved turbulent transport remain relatively small in most of the domain (except near the center of the channel). Further the large difference between results at $C_s = 0.10$ and $C_s = 0.17$ appears to be largely related to the considerable difference in mean-flow subgrid-model dissipation, which roughly doubles for the $C_s = 0.17$ case. This can be directly related to the fact that $(C_s\Delta)^2$ is more than twice higher for the 0.17 case than for the 0.1 case.

However, over-dissipation is not the only possible cause for an overshoot of the velocity gradient, as also the effect of transport may play an active role. To demonstrate this, we investigate the small-small VMS Smagorinsky model, which applies a high-pass filter to the resolved scales before extracting the subgrid stresses. As a result of this, the VMS subgrid stresses drop to zero

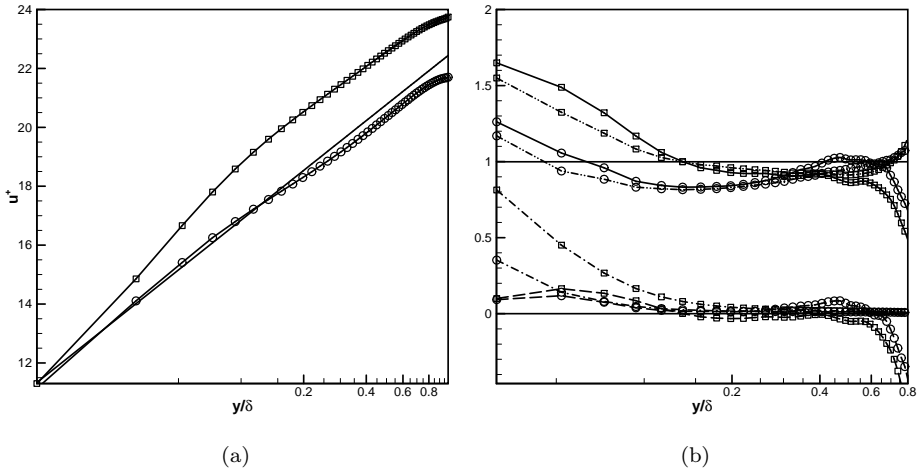


Figure 4.2: Mean velocity (left), and terms contributing to $\bar{\phi}(y)$ (right) for the standard Smagorinsky model with Mason & Thomson’s damping[54] near the wall. Symbols, (\circ): $C_s = 0.10$; (\square): $C_s = 0.166$. Lines in right figure, (—, black): $\bar{\phi}(y)$. Further, all multiplied by $y\kappa/[u_\tau(u_\tau^2 - fy)]$, (---, blue): mean-flow subgrid-model dissipation; (- · - ·, green) sum of all subgrid contributions (dissipation + transport), (---, red): resolved turbulent transport.

at the wall, where the solution is under resolved, roughly corresponding to a RANS-like region. The mean streamwise velocities and the budgets for $\phi(y)$ are shown in Fig. 4.3 for the standard Smagorinsky model ($C_s = 0.11$) and the small-small version of the VMS model, respectively.

It can be seen that the $\phi(y)$ predicted by the VMS model experience firstly an overshoot and then an undershoot. We can see that the SGS terms $\tilde{\epsilon}$ for the standard Smagorinsky model is actually higher than that of the VMS model, however, mean-flow SGS dissipation which is part of the SGS terms is zero for the VMS model since $\langle \tau_{ij} \rangle$ is zero, which has been high-pass filtered. If we subtract the mean-flow SGS dissipation from the $\tilde{\epsilon}$ and define the remaining terms as $\tilde{\epsilon}'$, we then find that $\tilde{\epsilon}'$ and T of the VMS model are actually much higher than those of the Smagorinsky model. These terms mainly account for the interactions between the smallest resolved scales and the unresolved sub-grid scales. It must be noted that the VMS model is calibrated and yields better results than the standard Smagorinsky model only when the scale separation happens and the interaction between the integral length scales and sub-grid scales can be neglected. However, near the wall where the grid cut-off is

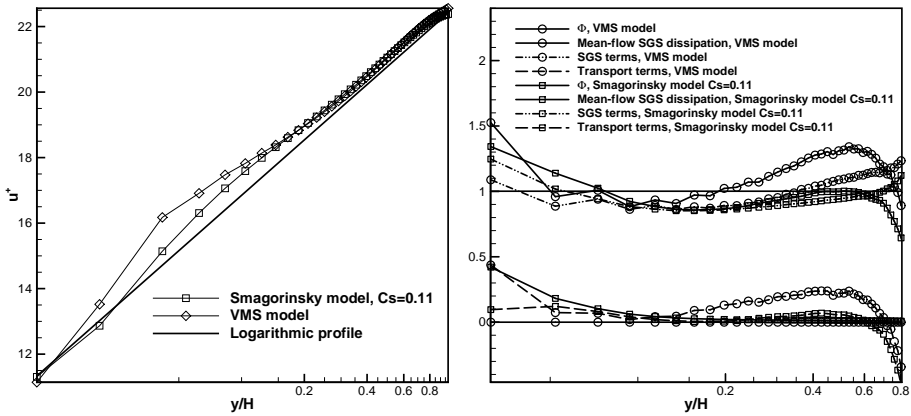


Figure 4.3: The mean velocity (left) and budgets for $\phi(y)$ (right) using the VMS model and the standard Smagorinsky model with $C_s = 0.11$ respectively.

comparable with the integral length scales, the fore mentioned requisites are no longer valid. Hence, the mean-flow SGS dissipation can be neglected far away from the wall, but not near the wall, where the simulation does not resolve any fluctuations.

Hence, although the VMS is under-dissipated compared with the standard Smagorinsky model (the total SGS dissipation is lower), the $\phi(y)$ is still over-predicted, clarifying that over-dissipation is not the sole possible cause for over-prediction of the mean velocity gradient.

4.3 A self-adaptive Smagorinsky model for LES of high-Re boundary layer flows

In the current section, a model is derived that can be, e.g. used to determine the correct Smagorinsky length scale in the logarithmic region of a boundary layer. First, in §4.3.1, we discuss the derivation of this self-adaptive model. Subsequently, we briefly explain the practical implementation of the new self-adaptive model in the second-order FV-based in-house code FLOWAVE . Since the turbulent kinetic energy equation used to derive an expression for ϕ is a derived property in incompressible flow, obtained from momentum and continuity, it is important to implement a discrete version of the model (and underlying energy equation), which corresponds to the discrete momentum

balance. First, in §4.3.2 the discrete implementation of the model is discussed for internal grid points. Next, in §4.3.3 additional issues related to the boundary points near the wall are addressed.

4.3.1 Derivation of the self-adaptive model

By reorganizing the terms which involve the subgrid-scale model in (4.15), we have

$$\bar{\phi}(y) = \frac{\kappa y}{u_\tau} \frac{d\bar{u}}{dy} \approx \frac{y\kappa}{u_\tau(u_\tau^2 - fy)} \left[\left\langle \bar{u}'_i \frac{\partial \tau'_{M,ij}}{\partial x_j} \right\rangle - \langle \tau_{M,12} \rangle \frac{\partial \langle \bar{u} \rangle}{\partial y} + T_{RES} \right]. \quad (4.18)$$

We now express the Smagorinsky SGS stress as

$$\tau_{M,ij} = -2l_s^2 |\bar{S}| \bar{S}_{ij} \equiv l_s^2 \psi_{ij}, \quad (4.19)$$

introducing an auxiliary tensor $\psi_{ij} = -2|\bar{S}| \bar{S}_{ij}$. Then Eq. (4.18) is reformulated into

$$\bar{\phi}(y) \approx \frac{\kappa y}{u_\tau(u_\tau^2 - fy)} \left[l_s^2 \left(\left\langle \bar{u}'_i \frac{\partial \psi'_{ij}}{\partial x_j} \right\rangle - \langle \psi_{12} \rangle \frac{\partial \langle \bar{u} \rangle}{\partial y} \right) + \frac{dl_s^2}{dy} \langle \bar{u}'_i \psi'_{i2} \rangle + T_{RES} \right]. \quad (4.20)$$

Hence, we obtain a simple ordinary differential equation (ODE) which determines l_s , i.e.,

$$A(y) \frac{dl_s^2}{dy} + B(y) l_s^2 + C(y) = 0, \quad (4.21)$$

with

$$A(y) = \langle \bar{u}'_i \psi'_{i2} \rangle, \quad B(y) = \left\langle \bar{u}'_i \frac{\partial \psi'_{ij}}{\partial x_j} \right\rangle - \langle \psi_{12} \rangle \frac{\partial \langle \bar{u} \rangle}{\partial y},$$

and $C(y) = T_{RES} - \frac{u_\tau(u_\tau^2 - fy) \bar{\phi}}{\kappa y}.$ (4.22)

Given any type of known velocity gradient $\bar{\phi}(y)$, and using the boundary condition $l_s \langle \psi_{12} \rangle = u_\tau$ at $y = y_0$, this ODE may be solved. In the current work, we focus on the situation where $\bar{\phi}(y) = 1$, i.e., related to a logarithmic velocity profile.

Taking $\bar{\phi}(y) = 1$, an exact solution can be expressed for Eq. (4.21). However, the resulting expression is rather cumbersome, involving multiple nestings of exponentials and integrals. Similarly, an approach based on numerical

integration of the ODE may also introduce significant computational complexity. Instead, in the current work, we strongly simplify the equation based on an order-of-magnitude analysis, which requires $l_s \sim \Delta$ (i.e. more particularly $l_s \ll \Delta$).

As a starting point, let us presume above the logarithmic layer, which we select conveniently to be $y \geq 0.2\delta$, that $l_s = C_s\Delta \approx 0.2\Delta$ (with Δ the LES filter width or grid spacing), then $dl_s^2/dy = \mathcal{O}(l_s\Delta/\delta)$. Hence,

As a starting point, let us presume above the logarithmic layer, which we select conveniently to be $y \geq 0.2\delta$, that $l_s = C_s\Delta \approx 0.2\Delta$ (with Δ the LES filter width or grid spacing), then $dl_s^2/dy = \mathcal{O}(l_s\Delta/\delta)$. Hence,

$$\frac{dl_s^2}{dy} \langle \bar{u}'_i \psi'_{i2} \rangle \sim l_s \Delta \left\langle \bar{u}'_i \frac{\psi'_{i2}}{\delta} \right\rangle \ll l_s \Delta \left\langle \bar{u}'_i \frac{\partial \psi'_{ij}}{\partial x_j} \right\rangle. \quad (4.23)$$

The inequality above is based on the fact that the fluctuating filtered shear in LES is a (resolved) small-scale property, such that $\partial \psi'_{ij}/\partial x_j \sim \psi'_{ij} e_j/\Delta \sim \psi'_{i2}/\Delta$. When l_s sufficiently large, we then obtain

$$\frac{dl_s^2}{dy} \langle \bar{u}'_i \psi'_{i2} \rangle \ll l_s \Delta \left\langle \bar{u}'_i \frac{\partial \psi'_{ij}}{\partial x_j} \right\rangle \sim l_s^2 \left\langle \bar{u}'_i \frac{\partial \psi'_{ij}}{\partial x_j} \right\rangle. \quad (4.24)$$

We will illustrate that this order-of-magnitude analysis is reasonably well satisfied resulting in good velocity gradients in §4.4.

Thus, neglecting $A(y)dl_s^2/dy$ in (4.21), we obtain

$$l_s^2 = \frac{u_\tau(u_\tau^2 - fy)/(\kappa y) - T_{RES}}{\left\langle \bar{u}'_i \frac{\partial \psi'_{ij}}{\partial x_j} \right\rangle - \langle \psi_{12} \rangle \frac{\partial \langle \bar{u} \rangle}{\partial y}}. \quad (4.25)$$

This formula may now be directly used in the logarithmic region of wall-modeled large-eddy simulations for a ‘dynamic’ determination of the Smagorinsky length scale.

Finally, we turn to an asymptotic analysis of the model for $\bar{u}'_i \rightarrow 0$, in which case the LES turns into a Reynolds-averaged Navier–Stokes simulation. Following limits can then be used for the analysis of Eq. (4.21):

$$\bar{u} = \langle \bar{u} \rangle, \quad \frac{d\langle \bar{u} \rangle}{dy} = \frac{u_\tau}{\kappa y}, \quad \text{and} \quad \bar{v} = \bar{w} = 0. \quad (4.26)$$

It is now easily verified that $A(y) = 0$ in this case. Further, also $\psi'_{ij} = 0$, and the only non-zero component of $\langle \psi_{ij} \rangle$ corresponds to

$$\psi_{12} = -2|\bar{S}|\bar{S}_{12} = - \left(\frac{d\langle \bar{u} \rangle}{dy} \right)^2. \quad (4.27)$$

Hence, for $\bar{u}'_i \rightarrow 0$, Eq. (4.21) becomes

$$l_s^2 = \frac{u_\tau(u_\tau^2 - fy)}{\kappa y \left[-\langle \psi_{12} \rangle \frac{d\langle \bar{u} \rangle}{dy} \right]} = \frac{u_\tau(u_\tau^2 - fy)}{\kappa y \left[\frac{d\langle \bar{u} \rangle}{dy} \right]^3} = (\kappa y)^2 (1 - fy/u_\tau^2). \quad (4.28)$$

For $fy/u_\tau^2 \ll 1$, we obtain to first order that $l_s = \kappa y$, which corresponds to Prandtl's classical expression for the mixing length in a boundary layer close to the wall.

4.3.2 Discretization of energy balance and self-adaptive model in internal points

Discretizing (4.18), and using $\delta/\delta x_i$ as a short-hand notation for the discretized derivatives, we obtain

$$\bar{\phi}(y) \equiv \frac{y\kappa}{u_\tau} \frac{d\langle \bar{u} \rangle}{dy} \approx \frac{y\kappa}{u_\tau(u_\tau^2 - fy)} \left[\underbrace{\left\langle \bar{u}'_i \frac{\delta \tau'_{M,ij}}{\delta x_j} \right\rangle}_{\text{term I}} - \underbrace{\langle \tau_{M,12} \rangle \frac{\delta \langle \bar{u} \rangle}{\delta y}}_{\text{term II}} + T_{RES} \right]. \quad (4.29)$$

In (4.18), we already chose a continuous form of the model which is consistent with the way the equation is constructed from the momentum equation. Term I in (4.29) is obtained by multiplying the divergence of the subgrid-scale stress in the discrete momentum equations with the velocity vector, subsequently followed by ensemble averaging, and removing the effects of the mean velocity, and mean subgrid-scale stress. Term II is obtained by multiplying the divergence of the mean subgrid-scale stress (in the mean momentum balance, i.e. Eq. 4.9) by the mean velocity gradient $\delta \langle \bar{u} \rangle / \delta y$. In continuous form, these terms may be conveniently reformulated (e.g. separating sub-grid dissipation and sub-grid dispersion), or contracted, but in discrete this is not generally possible, i.e.

$$\begin{aligned} \left\langle \bar{u}'_i \frac{\delta \tau'_{M,ij}}{\delta x_j} \right\rangle &\neq - \left\langle \tau'_{M,ij} \frac{\delta \bar{u}'_i}{\delta x_j} \right\rangle + \frac{\delta}{\delta y} \langle \tau'_{M,j2} \bar{u}'_j \rangle, \\ \langle \tau_{M,12} \rangle \frac{\delta \langle \bar{u} \rangle}{\delta y} &\neq \frac{\delta \langle \tau_{M,12} \rangle \langle \bar{u} \rangle}{\delta y} - \langle \bar{u} \rangle \frac{\delta \langle \tau_{M,12} \rangle}{\delta y}, \end{aligned} \quad (4.30)$$

and it important to use the left-hand sides of above inequalities and not the right-hand sides (though they are valid for the continuous case) in the formulation of the discretized model.

In the current work, we employ a collocated second-order finite-volume method for spatial discretization on a Cartesian mesh. The discretization of Eq. (4.25) is relatively straightforward, and values for l_s are calculated at the cell centers. We obtain (using index c for cell center, and f for cell face)

$$\left\langle \bar{u}'_i \frac{\partial \psi'_{ij}}{\partial x_j} \right\rangle_c \Omega_c \approx \left\langle \bar{u}'_{i,c} \sum_f [\psi'_{ij,f} n_{j,f} \Gamma_f] \right\rangle, \quad (4.31)$$

with $\Omega_c = \Delta_1 \Delta_2 \Delta_3$ the cell volume, Γ_f the face surfaces, and $n_{j,f}$ the face normals. Further, using t and b indices to denote the top and bottom face of a cell (resp. at $y_c + \Delta_y/2$ and $y_c - \Delta_y/2$),

$$\left[\langle \psi_{12} \rangle \frac{\partial \langle \bar{u} \rangle}{\partial y} \right]_c \Omega_c \approx \frac{1}{2} \langle \psi_{12,t} + \psi_{12,b} \rangle [\langle \bar{u}_t \rangle \Gamma_t - \langle \bar{u}_b \rangle \Gamma_b]. \quad (4.32)$$

Further, face values of u and ψ'_{ij} are obtained using linear interpolation and second-order central differences using cell-centered values of the velocities.

Finally, also the resolved turbulent diffusion term T_{RES} needs to be discretized. Starting from the momentum equation in discretized form multiplied with $\bar{\mathbf{u}}'$ we arrive at

$$T_{RES} = \left\langle \bar{u}'_i \frac{\delta \bar{u}'_i \bar{u}'_j}{\delta x_j} \right\rangle + \left\langle \bar{u}'_i \frac{\delta \bar{p}'}{\delta x_i} \right\rangle \neq \frac{\delta}{\delta y} \langle q \bar{v}' \rangle + \frac{1}{\rho} \frac{\delta}{\delta y} \langle \bar{v}' \bar{p}' \rangle, \quad (4.33)$$

where above inequality becomes an equality for the continuous case.

4.3.3 Discretization issues at boundary points

At points close to the wall (i.e. in our simulations, this applies to the first three cells closest to the wall), additional issues arise, which should be carefully treated to achieve an accurate discretization of the self-adaptive length-scale model. Even then, a peak in the error is observed around the second and third point from the wall (cf. results in Section 4.4). In our opinion, the reasons for that are related to inherent discretization errors on the mean shear, as discussed first in §4.3.3. A second point of importance is ensuring that the total shear is linearly interpolated (instead of ψ'_{ij}), further discussed in 4.3.3.

Accurate discretization of mean shear

An essential problem which occurs at points close to the wall is related to the accuracy of the discretization of the shear, and in particular the accurate representation of its mean component.

The average shear corresponds to $d\langle\bar{u}\rangle/dy$, and its discretization may be expressed based on a Taylor series expansion as

$$\frac{\delta\langle\bar{u}\rangle}{\delta y} = \frac{d\langle\bar{u}\rangle}{dy} + c_1\Delta_y \frac{d^2\langle\bar{u}\rangle}{dy^2} + c_2\Delta_y^2 \frac{d^3\langle\bar{u}\rangle}{dy^3} + \cdots + c_n\Delta_y^n \frac{d^{n+1}\langle\bar{u}\rangle}{dy^{n+1}} + \cdots, \quad (4.34)$$

where Δ_y is the wall-normal grid-spacing, and where c_1, c_2, \dots are coefficients which depend on the selected discretization scheme (in the current work, we use a central second-order scheme, for which $c_1 = 0$ and $c_2 = 1/6$).

In the particular case of a logarithmic mean-velocity profile, we obtain that

$$\frac{d^n\langle\bar{u}\rangle}{dy^n} = (-1)^{n-1} \frac{u_\tau}{\kappa} \frac{(n-1)!}{y^n} \quad (n = 1, 2, \dots). \quad (4.35)$$

For cells close to the wall, and defining the normalized distance $d = y/\Delta_y$ (e.g., $d = 1/2, 1, 3/2$, and 2 at the cell centers, and top faces of the first two cells), the relative error on the mean shear is expressed as

$$\frac{\delta\langle\bar{u}\rangle/\delta y}{d\langle\bar{u}\rangle/dy} - 1 = -c_1 \frac{1}{d} + c_2 \frac{2}{d^2} + \cdots + (-1)^n c_n \frac{n!}{d^n} + \cdots \quad (4.36)$$

Consequently, for $d < 1$ the relative error on the derivative becomes high, irrespective of the order of the discretization scheme. For cells far away from the wall, this is not an issue, since in that case $d \gg 1$. Hence, given a logarithmic mean-velocity profile, the discretized representation of $\phi(y)$ close to the wall in Eq. (4.29) is not equal to unity due to the aforementioned discretization error.

To circumvent this problem in the first cells closest to the wall, instead of using unity, we use a corrected value of $\phi(y)$ in Eq. (4.29). To this end, we presume a logarithmic mean profile, and obtain the discretized value $\phi_d(y)$ of $\phi(y)$ by plugging that profile in the discretization for the wall-normal velocity derivative, i.e.,

$$\phi_d(y) = y \frac{\delta \log(y/y_0)}{\delta y}. \quad (4.37)$$

For $d \gg 1$, we find that $\phi_d(y) \approx \phi(y)$. For instance, at the fourth grid point (with $d = 7/2$), $\phi_d(7\Delta_y/2) \approx 1.03$.

Note that this approach yields very satisfactory results for the RANS-like simulations (cf. §4.4.1). For the LES some errors remain, related to the fact that discretization errors close to the wall also affect the resolved fluctuating part of the shear. These errors are much more difficult to quantify.

Interpolation of $\langle \psi_{12} \rangle$

A final problem which need to be addressed is the interpolation of $\langle \psi_{12} \rangle$ close to the wall. At internal grid-points we straightforwardly employ linear interpolation to obtain $\langle \psi_{12} \rangle$ at cell centers from values at faces (cf. Eq. 4.32). Formally, by virtue of the integrated momentum balance, the total shear stress is known to behave linearly, such that

$$\langle \tau_{M,12} \rangle_c + \langle \bar{u}'_c \bar{v}'_c \rangle = \frac{1}{2} [\langle \tau_{M,12} \rangle_t + \langle \tau_{M,12} \rangle_b + \langle \bar{u}'_t \bar{v}'_t \rangle + \langle \bar{u}'_b \bar{v}'_b \rangle]. \quad (4.38)$$

At cells close to the wall, both $\langle \bar{u}' \bar{v}' \rangle$ and $\tau_{M,12}$ change non-linearly, and only their sum is accurately approximated by linear interpolation. Therefore, close to the wall (i.e. in the first three points), we approximate (cf. Eq. 4.32)

$$l_s \left[\langle \psi_{12} \rangle \frac{\partial \langle \bar{u} \rangle}{\partial y} \right]_c \Omega_c \approx \frac{1}{2} [l_s \langle \psi_{12,t} + \psi_{12,b} \rangle + \langle \bar{u}'_t \bar{v}'_t \rangle + \langle \bar{u}'_b \bar{v}'_b \rangle - 2 \langle \bar{u}'_c \bar{v}'_c \rangle] [\langle \bar{u}_t \rangle \Gamma_t - \langle \bar{u}_b \rangle \Gamma_b]. \quad (4.39)$$

Note that in this discrete approximation, l_s is presumed constant over the cell. However, this is fully consistent with neglecting the effect of $A(y)dl_s^2/dy$ in Eq. (4.21).

4.4 Wall-modeled LES using self-adaptive Smagorinsky length scales

We now investigate the self-adaptive Smagorinsky model for a number of wall-modeled large-eddy simulations. In §4.4.1 a first test is presented, in which the self-adaptive model is used up to the center of the channel. Next, in §4.4.2 a more physically relevant approach is elaborated, in which a set of simulations are presented for which the self-adaptive model is only used in the logarithmic region up to $y/\delta = 0.12$. Above the log region, it is merged with a constant-coefficient Smagorinsky model in the center of the channel. Finally, in §4.4.3, we continue discussion on the use of the self-adaptive model, and demonstrate some issues that may arise when it is used outside its region of validity.

The computational setup is the same as described in §4.2.3. The brackets in Eq. (4.25), representing ensemble averaging, are approximated by a combination of wall-parallel averaging and averaging in time, with a filter length of around $3.3\delta/U_c$, where U_c is the mean center-line velocity. Since our time integration

is based on an explicit Runge–Kutta method, the evaluation of l_s in Eq. (4.25) for determination of the LES solution in the next time step, is based on flow quantities in the current time step. Further details on the numerical implementation of the self-adaptive model are already discussed in §4.3.

4.4.1 Experiment with self-adaptive model for full channel height

In the current section, the self-adaptive model is first used for the full height of the channel, enforcing a logarithmic profile everywhere. Two cases are considered, both on a grid of $64 \times 36 \times 64$ cells. The first corresponds to a large-eddy simulation in which the Smagorinsky length l_s is determined using Eq. (4.25). The second case, is a RANS-like case (for which $\bar{u}'_i = 0$) which is run on the same mesh with the Smagorinsky model, using the asymptotic l_s expression obtained in Eq. (4.28). Results are shown in Figure 4.4.

In Figure 4.4(a), mean velocity profiles are shown for both cases. We observe a nearly perfect logarithmic profile up to the center of the channel for the RANS case. For the LES case, the match with the log profile is also very good except for the most central part of the channel ($y/\delta > 0.85$), and for the second point near the wall, which displays a small undershoot of the velocity. This is further appreciated in Figure 4.4(b), in which ϕ is displayed for both cases. The RANS result matches the normalized logarithmic derivative very well; errors on the LES remain below 5% for $y/\delta < 0.85$, except for a peak in the third point from the wall with an error of 10%. This is directly related to the small undershoot in the velocity at the second point. This is probably related to second-order discretization errors. Finally in Figure 4.4(c), values for $C_s = l_s/\Delta$ are shown. It is observed that the effective Smagorinsky coefficient of the LES case is considerably lower than the RANS case. This is related to the fact that in LES part of the Reynolds stresses are resolved in the simulation.

Near the center of the channel, the LES results do not follow the logarithmic layer (cf. Fig. 4.4). In this part of the flow, the resolved stresses T_{RES} , involving triple correlations of the resolved fluctuating velocity, play a dominant role in the determination of l_s . Probably related to this, we found it is difficult to get a converged flow solution, i.e., we had to extend the temporal averaging for the brackets in Eq. (4.25) up to 6 through-flow times. In case T_{RES} is not dominant in the determination of l_s (further discussed in next section), we find an averaging time of a few eddy turn-over times sufficient.

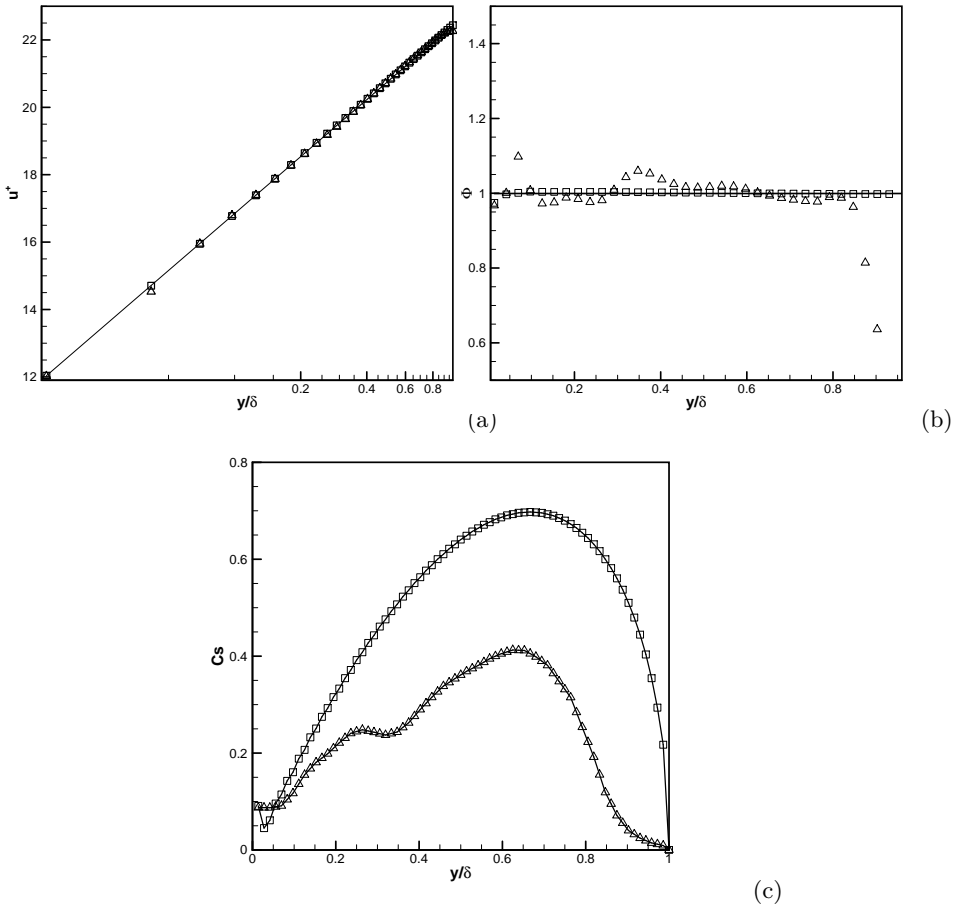


Figure 4.4: Mean velocity (a), normalized velocity gradient (b), and Smagorinsky coefficient C_s (c) obtained from a RANS-like simulation (\square), and a large-eddy simulation (\triangle), using l_s determined with a log profile up to the center. Both simulations use a $64 \times 36 \times 64$ mesh.

4.4.2 Use of self-adaptive model in the logarithmic region ($y < 0.12\delta$)

In real flow regimes, the log-layer is limited to the region near the wall. It is commonly accepted that the log-layer exists up to the upper limit of the inner region, i.e. roughly estimated as [67] $y/\delta \approx 0.1 - 0.15$. Therefore, the use of the self-adaptive model with $\phi = 1$, should be limited to this near wall region.

Table 4.1: Different cases for the testing of the self-adaptive model up to $y/\delta = 0.12$. All cases use equidistant meshes on a domain of $2\pi \times 1 \times \pi$, with wall roughness $y_0 = 10^{-4}\delta$.

	$N_x \times N_y \times N_z$	Δ/δ	Δ_x/Δ	Δ_x/Δ_y	Δ_x/Δ_z
Case 1	$96 \times 54 \times 96$	0.034	1.92	2.0	3.53
Case 2	$96 \times 72 \times 96$	0.031	2.11	2.0	4.71
Case 3	$128 \times 96 \times 128$	0.0232	2.11	2.0	4.71
Case 4	$192 \times 108 \times 192$	0.0171	1.92	2.0	3.53

Here we use the self-adaptive model up to 12% of the height of the channel in combination with a constant-coefficient Smagorinsky model in the center. To this end, a trigonometric blending function is employed, i.e.,

$$B(y) = \cos \left(\min \left(\frac{\pi}{2}, \max \left(0, \frac{y - 0.3\delta}{4\Delta_2} \pi \right) \right) \right), \quad (4.40)$$

with Δ_2 the grid spacing in the y -direction. Thus near the wall up to 12% of the channel height the self-adaptive model is employed and the mixing length is dynamically determined from the flow field, given that mean velocity displays a logarithmic profile. Beyond 12% of the channel height, the standard Smagorinsky model is employed using $C_s = 0.17$. Remark that the blending between both regions is localized to four cells around $y/\delta = 0.12$, so that the width of the blending region decreases with grid refinement.

Four simulations are performed with four different resolutions. Two ratios $\Delta_x/\Delta = 1.92$, and $\Delta_x/\Delta = 2.11$ are included, next to two different cell aspect ratios; details are provided in Table 4.1. The resulting velocity profiles and normalized mean-velocity gradients are shown in Fig. 4.5. It is appreciated that the performance of the new self-adaptive model is very good and the results are greatly improved compared to conventional approaches relying on a Smagorinsky model (cf., e.g., Fig. 4.2). For $y/\delta < 0.12$, the mean stream-wise velocity exhibits the desired logarithmic distribution, with an error on normalized mean-velocity gradient that is below 5%, except for the third point. In fact, in Fig. 4.5(a) we find a slight undershoot of the mean stream-wise velocity at the second point, which leads to a peak in the error of about 10% in the normalized mean-velocity gradients ϕ at the third point (in Fig. 4.5(b)). We believe this is mainly related to inevitable discretization errors, which impact on the self-adaptive determination of l_s in the points closest to the wall.

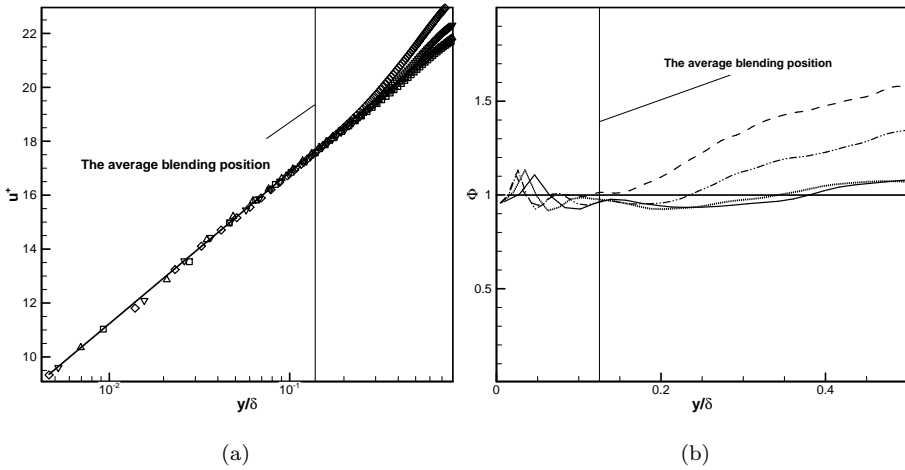


Figure 4.5: Stream-wise velocity profile in a semi-logarithmic scale (a), and normalized mean-velocity gradient $\phi(y) = (y\kappa/u_\tau)(d\langle u \rangle/dy)$ (b) for simulations with a self-adaptive model applied up to 12% of the channel height. Four cases are compared: $96 \times 54 \times 96$ (\square , and solid line), $96 \times 72 \times 64$ (Δ , and dotted line), $128 \times 96 \times 128$ (∇ , and dash-dot-dot line) and $192 \times 108 \times 192$ (\diamond , and dashed line).

It is important to note that the outer-layer results for the different grid resolutions show considerable disparity, and the predicted value of $\phi(y)$ beyond the blending position increases as the grid resolution increases. The results from the finer grid tend to yield higher velocities near the center, compared to that of the coarse grid. However, the coarsest grids used in the current study may be too coarse for a reliable prediction of the nearly isotropic turbulence which is expected in the channel center. Moreover, as various studies have shown,[59, 58, 55] the optimal Smagorinsky coefficient for very high Reynolds number isotropic flows depends on many factors, such as spatial discretization, the shape of grid cell and grid resolution, such that the value $C_s = 0.17$ may not be suitable. A comprehensive study on the effect of the Smagorinsky coefficient C_s in the center of the channel is not in the scope of the current study.

In Fig. 4.6 the average value of the Smagorinsky coefficients, and l_s is shown as function of the channel height. Averages over 100 through-flow times are shown. The effective values during the simulation fluctuate a lot more, partially due to the highly fluctuating nature of the triple correlations in T_{RES} . Nevertheless, we did not experience difficulties related to stability; the effect of T_{RES} is not

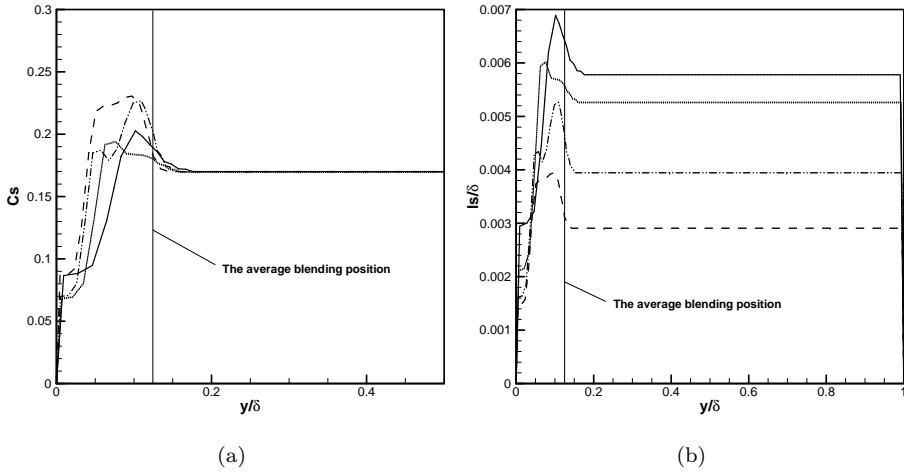


Figure 4.6: Averaged Smagorinsky coefficient (a) and length scale l_s (b) from the simulations with the self-adaptive model applied up to 12% of the channel height. Four cases are compared: $96 \times 54 \times 96$ (solid line), $96 \times 72 \times 92$ (dotted line), $128 \times 96 \times 128$ (dash-dot-dot line) and $192 \times 108 \times 192$ (dashed line).

dominant in the determination of l_s , i.e., in the order of 10% to 15%. We observe in Fig. 4.6 that above $y = 0.12$, all the curves converge to $C_s = 0.17$ as imposed by our blending. In the logarithmic region, the dependence of C_s on y and resolution is less trivial. Near the blending region, we find that the Smagorinsky coefficient increases up to a value of $C_s = 0.23$ for the finest mesh, while close to the wall, the coefficient drops to a value of $C_s \approx 0.08$.

Finally, in Fig. 4.7 the normal Reynolds stresses are displayed for the different cases. For comparison, a result using the standard Smagorinsky model with Mason and Thomson's wall damping, [54] is also shown. It is appreciated that the blending of the self-adaptive model with the constant Smagorinsky model in the outer layer of the boundary layer does not lead to abrupt changes in Reynolds stresses near the blending region.

4.4.3 Further discussion on the use of the self-adaptive model

During initial testing of the self-adaptive model, we focussed on cases with a blending at $y/\delta = 0.3$, as the logarithmic layer is often reported to exist up to 30% of the channel height for channel flows. As for the cases presented above,

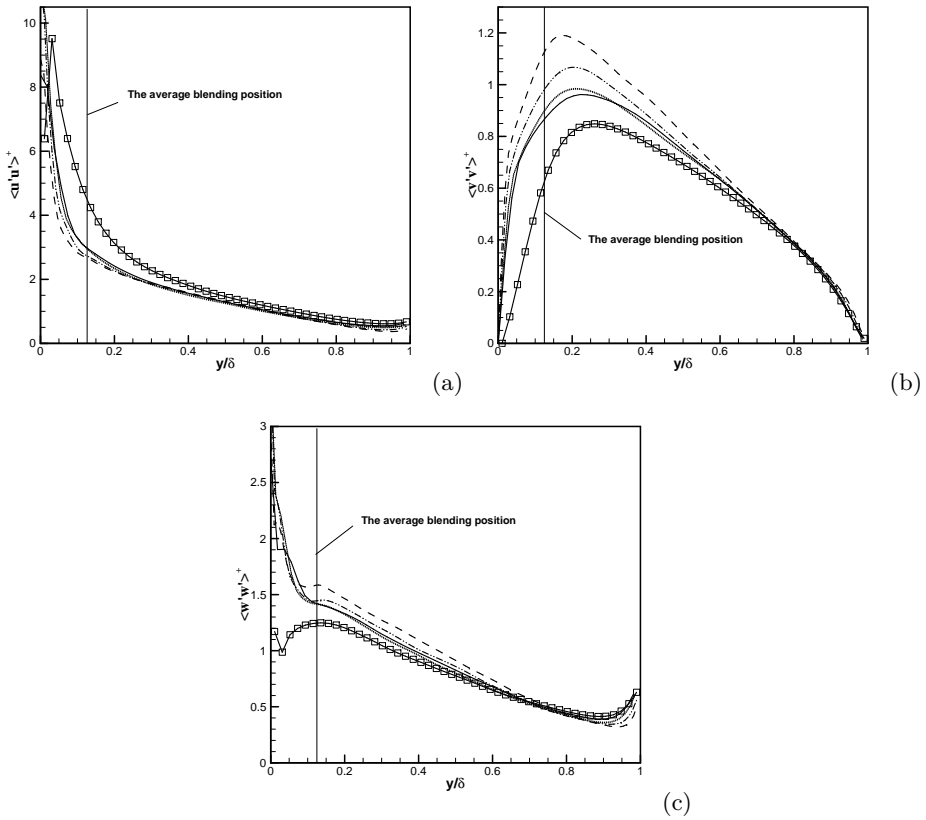


Figure 4.7: Normal Reynolds stresses $\langle u'u' \rangle / u_\tau^2$ (a), $\langle v'v' \rangle / u_\tau^2$ (b), and $\langle w'w' \rangle / u_\tau^2$ (c), from simulations with self-adaptive model applied up to 12% of the channel height, and comparison to conventional Smagorinsky result. Self-adaptive cases: $96 \times 54 \times 96$ (solid line), $96 \times 72 \times 92$ (dotted line), $128 \times 96 \times 128$ (dash-dot-dot line) and $192 \times 108 \times 192$ (dashed line). Conventional Smagorinsky model using $C_s = 0.17$, cf. Section 4.2.3 (\square —).

we find that the velocity profiles match the logarithmic law well in the region where we enforce it. However, we observed some issues related to convergence of the Smagorinsky coefficient, and the second-order statistics (discussed below) that we believe are worthwhile to report. Four different grid resolutions were considered, cf. Table 4.2.

In Fig. 4.8, the velocity profiles and normalized mean-velocity gradients ϕ are shown. It is appreciated that the new self-adaptive model performs as expected

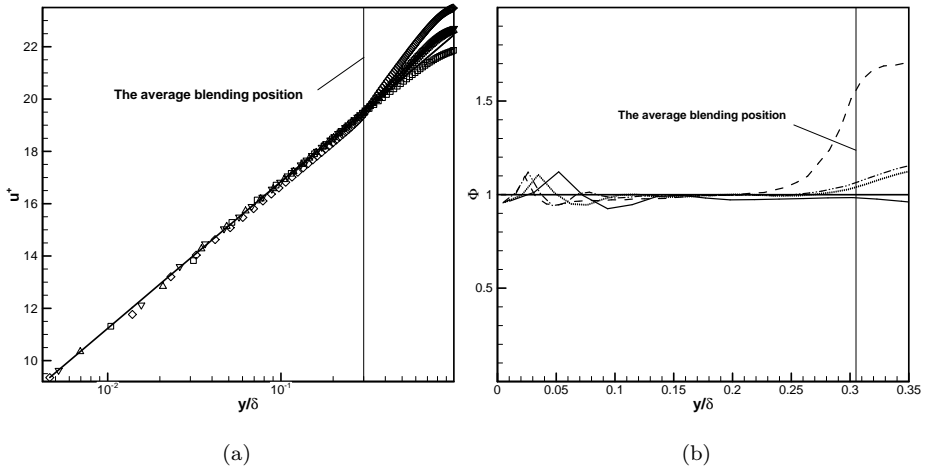


Figure 4.8: Stream-wise velocity profile in a semi-logarithmic scale (a), and normalized mean-velocity gradient $\phi(y) = (y\kappa/u_\tau)(d\langle u \rangle/dy)$ (b), for simulations with a self-adaptive model up to 30% of the channel height. Five cases are compared: $64 \times 48 \times 64$ (\square , and solid line), $128 \times 72 \times 128$ (Δ , and dotted line), $128 \times 96 \times 128$ (∇ , and dash-dot-dot line) and $192 \times 108 \times 192$ (\diamond , and dashed line).

Table 4.2: Different cases for the testing of the self-adaptive model up to $y/\delta = 0.3$. All cases use equidistant meshes on a domain of $2\pi \times 1 \times \pi$, with wall roughness $y_0 = 10^{-4}\delta$.

	$N_x \times N_y \times N_z$	Δ/δ	Δ_x/Δ	Δ_x/Δ_y	Δ_x/Δ_z
Case 2	$64 \times 48 \times 64$	0.0465	2.11	2.0	4.71
Case 3	$128 \times 72 \times 128$	0.0256	1.92	2.0	3.53
Case 4	$128 \times 96 \times 128$	0.0232	2.11	2.0	4.71
Case 5	$192 \times 108 \times 192$	0.0171	1.92	2.0	3.53

when looking at the velocity profiles. However when further looking at the Smagorinsky coefficient, and higher order statistical moments in Fig. 4.9, we observe that results behave rather unexpectedly when the grid is refined. First of all, the Smagorinsky coefficient does not converge with grid refinement. For

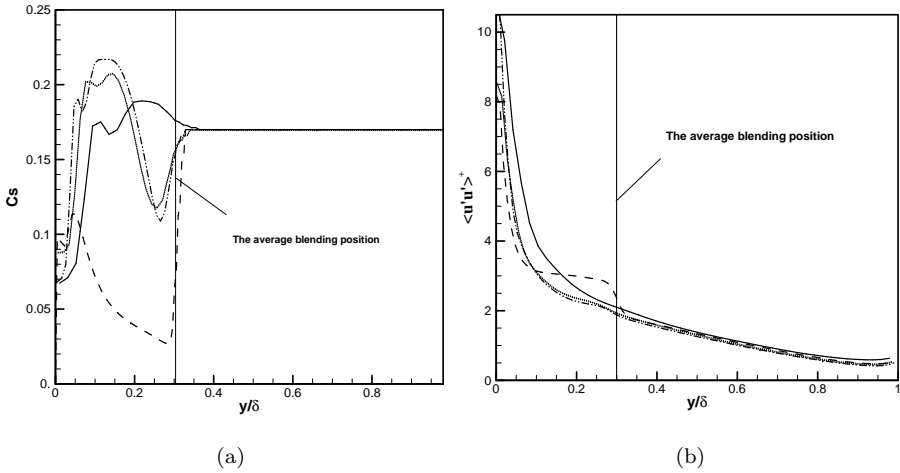


Figure 4.9: The averaged Smagorinsky coefficient (a) and normal Reynolds stress component $\langle u'u' \rangle / u_\tau^2$ (b) from the simulations with the self-adaptive model applied up to 30% of the channel height. Four cases are compared: $64 \times 48 \times 64$ (solid line), $128 \times 72 \times 128$ (dotted line), $128 \times 96 \times 128$ (dash-dot-dot line) and $192 \times 108 \times 192$ (dash line).

the finest mesh, C_s is very low left of the blending region, leading to a sharp increase of the Smagorinsky coefficient in the blending region. Also looking at the $\langle u'u' \rangle$ Reynolds stress in Fig. 4.9, we find that this jump in Smagorinsky coefficient for the finest mesh, leads to a jump in the energy content of the resolved velocity fluctuations ($\langle v'v' \rangle$, and $\langle w'w' \rangle$, not shown here, display similar behavior).

We believe that the lack of grid-convergence and the unrealistic second-order statistics are related to the fact that the log-layer is forced to far into the outer layer of the flow, where $\phi = 1$ is not valid anymore. For instance, looking at the DNS data of Hoyas and Jiménez [30] (cf. Fig. 4.1), we observe $\phi \approx 1.2$ around $y/\delta = 0.3$. Hence, even though we may force the mean flow into a desired logarithmic profile, the associated distribution of dissipation and turbulent transport (cf. Eq. (4.15)) can lead to unrealistic distributions of turbulent statistics. As demonstrated in §4.4.2 this poses no problem when the self-adaptive model is used in the inner layer of a high-Reynolds number channel flow, where a log-law correctly reflects the expected mean-velocity distribution.

4.5 Extension of the self-adaptive model to include viscous effect

In previous section, the new self-adaptive model is shown to be able to produce desired logarithmic velocity profile for a channel flow with rough walls. Assuming infinite Reynolds number, the viscous effect was neglected. In this section, the flow regimes where the Reynolds number is neither too high (the viscous effect can not be neglected) nor too low (so that wall-modeled LES is justified) are considered. Eq. (4.41) is expanded to include the viscous terms

$$\bar{\phi}(y) = \frac{\kappa y}{u_\tau} \frac{d\bar{u}}{dy} \approx \frac{y\kappa}{u_\tau(u_\tau^2 - fy)} \left[\left\langle \tilde{u}'_i \frac{\partial \tau'_{ij}}{\partial x_j} \right\rangle - \langle \tau_{12} \rangle \frac{\partial \langle \bar{u} \rangle}{\partial y} + T_{RES} + T_{VIS} \right], \quad (4.41)$$

where T_{vis} accounts for the viscous contribution to the mean shear and defined as

$$T_{VIS} = - \left\langle \tilde{u}'_i \frac{\partial \hat{\sigma}'_{ij}}{\partial x_j} \right\rangle = \langle \tilde{u} \rangle \frac{\partial \langle \hat{\sigma}_{ij} \rangle}{\partial x_j} - \left\langle \tilde{u} \frac{\partial \hat{\sigma}_{ij}}{\partial x_j} \right\rangle \quad (4.42)$$

Following the similiar procedures as is described by Eq. (4.20-4.25), we obtain

$$l_s^2 = \frac{u_\tau(u_\tau^2 - fy)/(\kappa y) - T_{RES} - T_{VIS}}{\left\langle \tilde{u}'_i \frac{\partial \psi'_{ij}}{\partial x_j} \right\rangle - \langle \psi_{12} \rangle \frac{\partial \langle \bar{u} \rangle}{\partial y}}. \quad (4.43)$$

A channel flow is considered here as the test case with the DNS results [29, 30] as reference. The dimensions of the channel in streamwise, wall-normal and spanwise directions are 2π , 1 and π respectively. The grid is $64 \times 72 \times 64$. The Reynolds numbers based on friction velocity Re_τ are 2000 and 950 respectively. Firstly, a preliminary study is conducted, and then four cases are computed, in combination with the conventional Smagorinsky model and the new self-adaptive model.

4.5.1 A Preliminary study of the channel flow with $Re_\tau = 2000$

Given the new self-adaptive model, many factors may influence the results for the case of finite Reynolds number. This preliminary study is intended to study the influence of these factors on the predicted mean velocities. The first factor is the viscous terms T_{VIS} , as defined by Eq. (4.42). The influence of the viscous effect at $Re_\tau = 2000$, which is commonly regarded as ‘high’ Reynolds number, is to be investigated. Secondly, as mentioned in previous

section, the transport terms T_{RES} , which contains triple correlations, caused a highly fluctuating dynamic mixing length, and sometimes even divergence of the simulations. This not only leads to more stringent time step restrictions (to avoid possible divergence) but also exceptionally long average time to take time statistics. As shown in Fig. 4.2, the magnitude of the transport terms accounts for a much smaller portion of the budgets for the mean shear compared with other terms. Thus it is worthwhile to investigate whether these terms can be neglected without sacrificing the quality of results. Thirdly, as shown in Fig. 4.1, the normalized mean shear, ϕ_y , is actually not unity, as far as the three DNS cases are concerned. The ϕ_y will increase up to 1.2 at around 40% of the channel height. This is not in line with the presumption considered in previous section that the ϕ_y is strictly unity below 30% of the channel height. Therefore, the influence of the value of ϕ_y , either a constant (unity) or spatially varying, needs further attention.

The next factor which may influence the prediction of mean shear is the position where the velocity is used to prescribe the shear stress at the wall. This study is based on the reasoning by Kawai and Larsson [40], who argued that the conventional WSM receives inevitably under-resolved input (the velocity components at the first grid point from the wall) from the LES. A simple and effective remedy was proposed: to simply increase the modeled wall-layer and taking input to the wall model from the inner grid point off the wall. The results have been notably improved and a much better prediction of the friction coefficient is achieved. They found it is sufficient to use the 4th point off the wall. In this work, j_τ , j -th grid point away from the wall, is used to denote the position where the velocity components are taken to feed the WSM. Finally the Smagorinsky coefficient C_s at the outer layer may also influence the prediction of the mean shear at the outer layer and in the blending region.

An overview of the test cases which have been carried out is given in Table 4.3. The first two cases are conducted to study the influence of the viscous terms on the prediction of the mean velocity profile. The third case is introduced to study the effect of j_τ , the position where the velocities are used to prescribe the wall stress. The fourth case excluded the transport terms, which often cause computational instability. The fifth case takes into account the spatially varying nature of the ϕ_y . In the sixth case, the Smagorinsky coefficient is calibrated according to Eq. (2.30). Three additional cases are conducted using conventional Smagorinsky model.

Fig. 4.10(a) shows the velocities predicted with mixing length calculated according to Eq. (4.25) and Eq. (4.43). The difference between the two velocities is notable, therefore the influence of the viscous effect can not be neglected even at $Re_\tau = 2000$, which is normally considered as a high Reynolds number. The mean velocity profile considering the viscous effect matches the desired

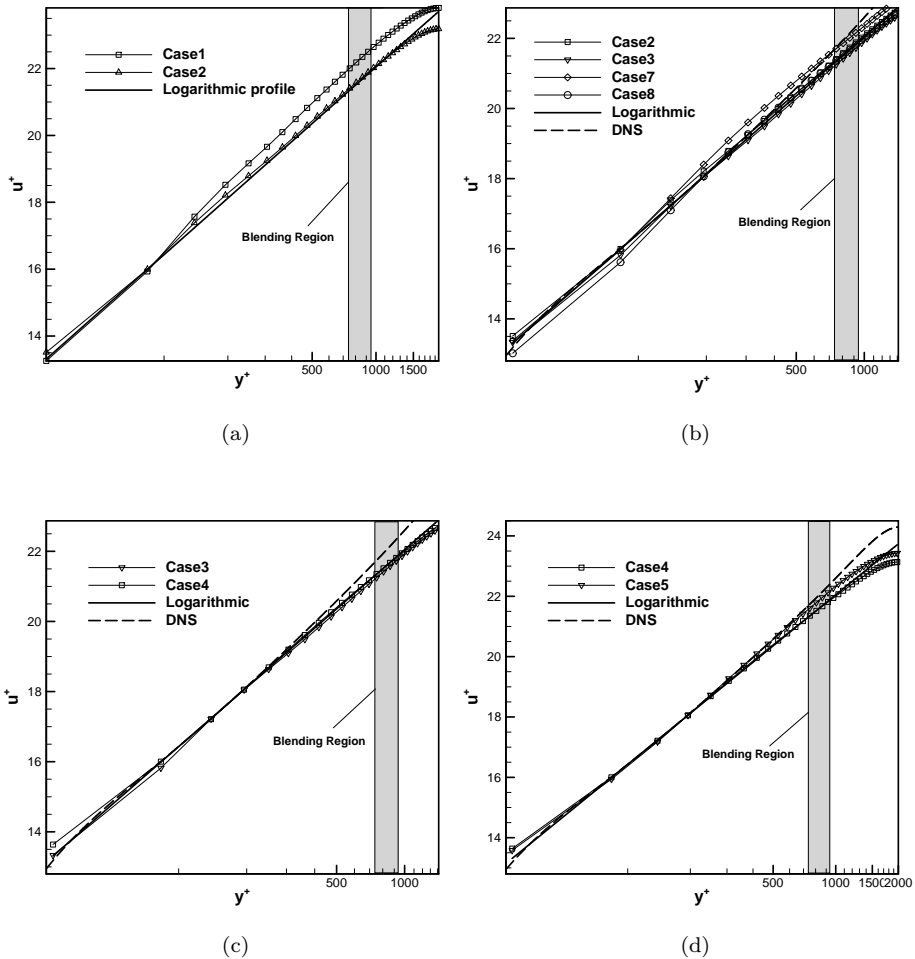


Figure 4.10: The predicted normalized mean velocities ($Re_\tau = 2000$) in comparison with DNS results [30] and logarithmic profile (classic log law) with logarithmic x-axis representing y^+ . The factors which influence the prediction of normalized mean velocities are investigated and can be found respectively in: (a) the viscous terms, (b) the transport terms, (c) j_τ , the positions where the velocities are taken to computed wall stress and (d) the value of $\phi(y)$.

Table 4.3: Overview of channel flow test cases used to test the factors which influence the prediction of log velocity profile

Case	T_{VIS}	T_{RES}	ϕ_y	C_s	j_τ	SGS model	Blending position
1	no	yes	1	0.17	2	self-adaptive model	30%
2	yes	yes	1	0.17	2	self-adaptive model	30%
3	yes	yes	1	0.17	4	self-adaptive model	30%
4	yes	no	1	0.17	4	self-adaptive model	30%
5	yes	no	varying	0.17	4	self-adaptive model	40%
6	yes	no	varying	0.25	4	self-adaptive model	40%
7	/	/	/	0.17	2	Smagorinsky model	/
8	/	/	/	0.17	4	Smagorinsky model	/
9	/	/	/	0.25	4	Smagorinsky model	/

logarithmic profile well. One should note, however, the actual velocity profile is not an exact logarithmic profile, as will be shown later; the purpose of this study is just to show the ability of the revised model to produce the desired velocity profile and the importance of the viscous term T_{VIS} .

The influence of j_τ is then investigated. Four cases are setup, corresponds to case 2, 3, 7 and 8 in Table 4.3. The y^+ at the first grid point off the wall is around 28 for $Re_\tau = 2000$, thus $j_\tau = 2$ and $j_\tau = 4$ are chosen for both the conventional Smagorinsky model and the self-adaptive model, which are safely situated in the logarithmic region. It is noticed that the result for the inner layer (up to $y^+ = 450$) has been improved for the conventional Smagorinsky model with $j_\tau = 4$ compared with $j_\tau = 2$, confirming the aforementioned findings in [40]; whereas for the self-adaptive model, the difference is small and the results are less dependent on the value of j_τ .

The influence of the transport term T_{TRES} as defined by Eq. (4.14) is then studied and the predicted mean velocities with and without T_{TRES} are shown in Fig. 4.10(c). This term contains a three-order moment term, and is highly fluctuating, often causes numerical instability and divergence. The difference between the two velocities is very small, both velocities match the desired velocity quite well. Thus for the sake of numerical instability, this term will be neglected in following calculations.

Another important observation is that the real velocity profile (DNS data) does not follow a logarithmic distribution from around $y^+ = 200$, where the mean velocity gradient notably increases, which is evidenced in Fig. 4.11. Thus the value of $\phi(y)$ should be revised to take into account the deviation from the standard logarithmic profile. A empirical fit of $\phi(y)$ is then proposed and takes

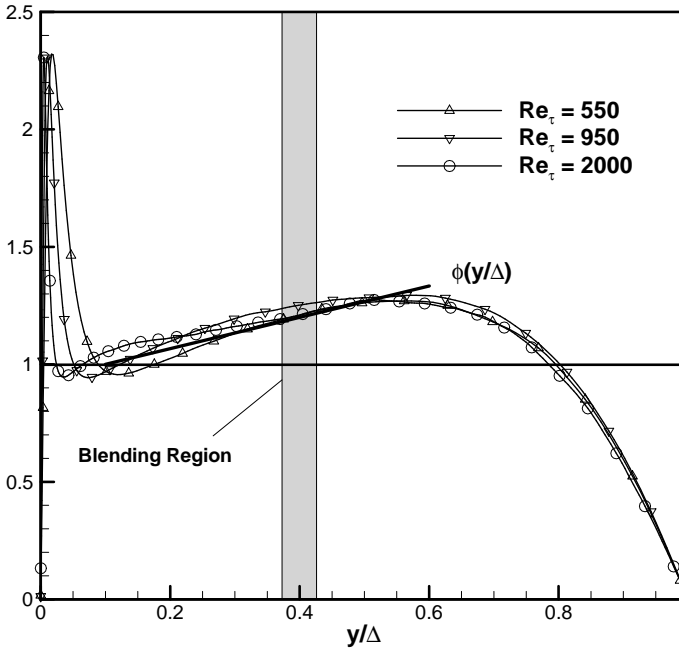


Figure 4.11: Normalized mean velocity gradient $\phi(y)$, calculated from the DNS data [30]. The read line indicates the empirical fit of $\phi(y)$, see Eq. (4.44).

the following form

$$\phi(y) = \frac{2(y - 0.1)}{3} + 1, 0.1 \leq y \leq 0.4$$

$$\phi(y) = 1, y < 0.1 \quad (4.44)$$

The results using $\phi(y) = 1$ and $\phi(y)$ as an empirical fit are shown in Fig. 4.10(d). The later obviously provides a better fit than the constant $\phi(y)$.

Finally, the influence of the Smagorinsky coefficient are investigated. The Smagorinsky coefficient is calibrated according to Eq. (2.30), taking into account second-order discretization error and shape of filter. The calibrated Smagorinsky coefficient on current mesh is 0.25. However, one must note, as already mentioned in chapter 2, the second-order scheme which is used to derive Eq. (2.30) is not a real second-order scheme since only the effective wavenumber is modified, the spectrum is still assumed to be a perfect $-5/3$ spectrum, which

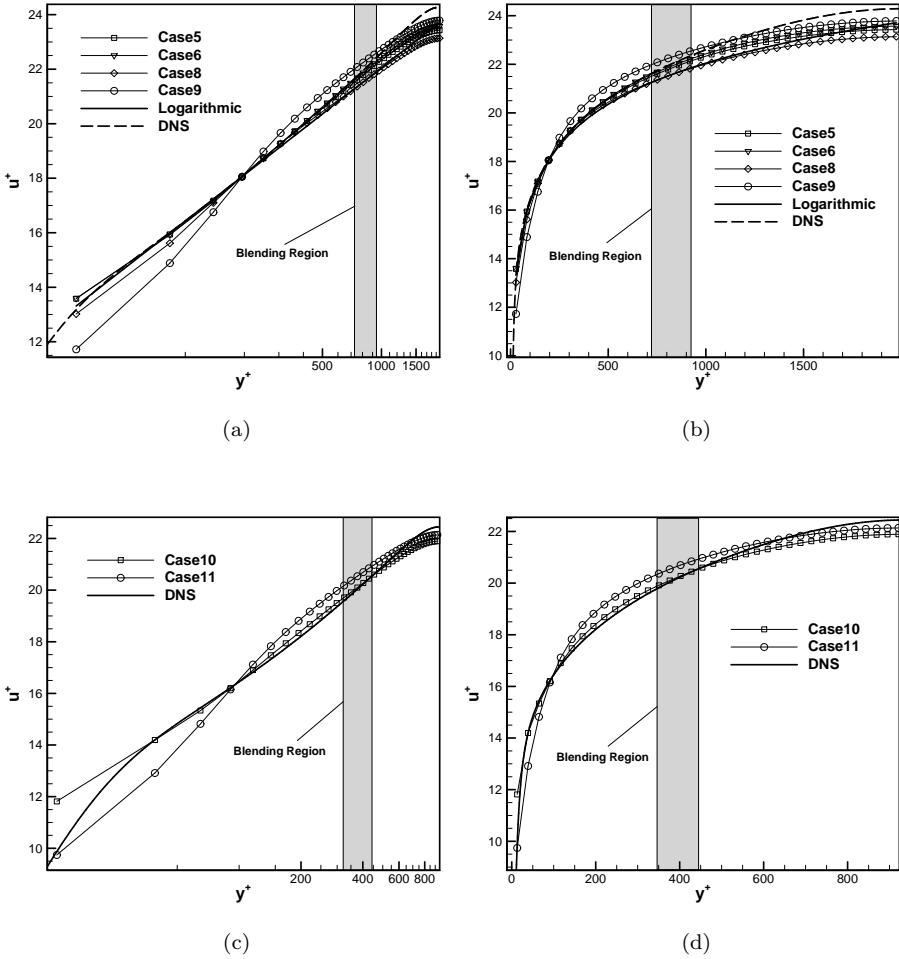


Figure 4.12: The predicted normalized mean velocities ($Re_\tau = 2000$ and $Re_\tau = 950$) using conventional Smagorinsky model and self-adaptive model with Smagorinsky coefficient 0.17 and 0.25 respectively, in comparison with DNS results [30] and logarithmic profile (classic log law) with (a) $Re_\tau = 2000$ plotted against a logarithmic x-axis representing y^+ , (b) $Re_\tau = 2000$ plotted against a non-logarithmic x-axis, (c) $Re_\tau = 950$ plotted against a logarithmic x-axis representing y^+ and (d) $Re_\tau = 950$ plotted against a non-logarithmic x-axis.

Table 4.4: Overview of channel flow test cases with $Re_\tau = 950$

Case	T_{VIS}	T_{RES}	the value of ϕ_y	C_s	j_τ	SGS model
10	yes	no	empirical fit	0.25	4	self-adaptive model
11	/	/	/	0.25	4	Smagorinsky model

is not the case if a real second-order scheme is employed. However, current analysis still sheds light on the trend of the Smagorinsky coefficient: the Lilly Smagorinsky coefficient 0.17 has led to a underprediction of the mean velocities near the center of the channel, thus a higher Smagorinsky coefficient should be expected.

Fig. 4.12(a) and 4.12(b) show the results obtained by both the conventional Smagorinsky model and the self-adaptive model with the Smagorinsky coefficients 0.17 and 0.25 respectively. The new self-adaptive model produces overall much more superior results than the Smagorinsky model. The self-adaptive model with the Smagorinsky coefficient 0.25 yields a better mean velocity near the center of the channel compared with 0.17. It is noticed that the Smagorinsky model with a Smagorinsky coefficient 0.25 is even inferior than the results of 0.17, showing that the aforementioned analysis of the Smagorinsky coefficient is not applicable for the inner layer, and the Smagorinsky coefficient can not be a constant, as evidenced in Fig. 4.9. In contrast, the self-adaptive model produces consistently good results for the inner layer, irrespective of the Smagorinsky coefficient which is used for the out layer.

4.5.2 The channel flow with $Re_\tau = 950$

The model is then applied to the channel flow with a $Re_\tau = 950$ and the results are shown in Fig. 4.12(c) and 4.12(d). The numerical setup can be found in Table 4.4. The self-adaptive model provides a much better prediction compared with the Smagorinsky model, except for the first grid point where the velocity is overpredicted for the self-adaptive model. This is expected since the first point corresponds to $y^+ \approx 13$, which no longer falls into the logarithmic region (approximately starting from $y^+ \approx 30$).

4.6 Conclusion

This study addressed one of the most persistent problems in wall-modeled LES, i.e., the overshoot of the mean velocity gradient in the log layer. The factors

influencing the mean velocity gradient in high-Reynolds number wall-modeled DNS and LES were analyzed, and a relationship between mean velocity gradient and turbulent kinetic energy budgets was elaborated. By analyzing the LES data from simulations of a rough-wall channel flow at infinite Reynolds number, we highlighted the different terms that contribute to the mean velocity gradient.

Based on the analysis, a self-adaptive model was proposed in which the Smagorinsky coefficient is dynamically adjusted to yield a logarithmic mean velocity distribution. The model was implemented in a second-order FVM code, and tested for various simulation cases. It was found that the mean-velocity gradient was well predicted, with errors on the normalized gradient which remain below 5%, except for the third point from the wall, with an error of 10%. The latter error was attributed to unavoidable discretization errors of the shear stresses close to the wall. Finding different discrete formulations of the self-adaptive model which cancel these errors, is subject of further research.

The model is then extended to include the viscous effect and applied to channel flows with $Re_\tau = 950$ and $Re_\tau = 2000$ respectively. The different factors which influence the prediction of the mean velocities are analyzed: the viscous effect is important and should be included, the transport terms can be safely neglected to ensure numerical stability; the position where the velocities are fed to the wall-stress model does not have a big influence on the results of the self-adaptive model, however, this is not the case for the Smagorinsky model; an empirical fit of $\phi(y)$ is proposed based on the DNS data and leads to an improved prediction; the Smagorinsky coefficient is calibrated and the new coefficient 0.25 proves to provide better results than the Lilly Smagorinsky coefficient 0.17. The self-adaptive model produces overall much better results than the conventional Smagorinsky model. Finally, the case of $Re_\tau = 950$ is computed, the result of the self-adaptive model matches the DNS data quite well except for the first grid point.

The current self-adaptive model was developed and demonstrated for the Smagorinsky model in high-Reynolds-number rough-wall channel flow. Hence, an interesting application area where it can be used in its present form would be, e.g., neutral atmospheric boundary-layer flows over flat terrain. Other applications may need additional research. In a more general formulation, the self-adaptive model may also be used to approximate any type of relevant mean-velocity gradient ϕ . This may be, e.g., interesting for the matching of velocity profiles in LES inlet flow zones to experimental data, or established analytical relations for the velocity profile. It is however important to emphasize that the self-adaptive model is not predictive, i.e. it requires a prescription for ϕ . Therefore, extensions to cases in which ϕ is not known a priori, such as e.g., boundary-layer separation, are not so straightforward.

Chapter 5

The application of wall-modeled LES: square duct flows

In this chapter, turbulent flows in a square duct at high Reynolds number are studied, using a conventional Smagorinsky model in the center of the duct and a self-adaptive Smagorinsky model near the walls which allows to recover correct velocity profiles close to the wall. At the wall, a wall-stress model is used as a boundary condition. This provides a better match than the classic log law with the experimental data. In section 5.1, a review of past experimental and numerical studies on duct flows are made. In section 5.2, the methodology and numerical setup is presented. The validity of the classical log law in duct flows is discussed. A modified log law, which describes the distribution of the normalized mean velocity along the wall bisector, is then proposed. The numerical results are shown in section 5.3. The methodology developed in this study provides a pragmatic wall-modeled LES methodology for the simulation of a square duct at high Reynolds numbers. The work discussed in this chapter is published in [97].

5.1 Introduction

Turbulent flows in rectangular ducts are commonly encountered in engineering practice, such as in air-conditioning systems, nuclear reactors, turbomachinery

and heat exchangers. These flows are characterized by Prandtl's secondary flows in the cross-sectional plane, which are driven by the turbulent motion and have a significant effect on the transport of momentum [16]. Although the magnitude of the secondary flows is relatively weak (1-3% of the mean streamwise velocity), its impact on the transport of heat and momentum is quite significant. As a result, the mean streamwise velocity and local wall shear stress are distorted considerably towards the corners.

A considerable number of experimental investigations, dated back to 1960s and 1970s, have been carried out on turbulent flow in straight non-circular ducts to understand underlying physics of secondary flows. Brundrett and Baines are among the first to provide a fairly complete description of these secondary motions in a square duct, with the Reynolds number based on bulk velocity Re_b at 83000 [7]. Gessner examined the mechanism of initiated secondary flow in developing turbulent flow along a corner in his early experiments [20, 22, 21]. Both the square ducts and rectangular ducts are measured, with the Reynolds number up to 250000. Other experimental studies can be found in [47, 42]. Demuren and Rodi made a review of early experimental studies [16]; by analyzing the experimental data at various Reynolds numbers, they found the ratio of maximum (centerline) velocity to bulk velocity U as well as the mean friction velocity, decrease with increasing Reynolds number. Another review on both experimental and numerical studies can be found in [66].

Numerical studies in this area started a lot later than the experimental studies. Gavrilakis presented the DNS results for the turbulent flow in a straight duct of $Re_\tau = 300$ (based on mean friction velocity) and $Re_b = 4410$ [18]. He found the turbulent statistics along the wall bisectors show good agreement with plane channel data despite the influence of the sidewalls in the former flow. He also found the mean velocity along the wall bisector exhibit a logarithmic distribution $u^+ = 3.2 \ln y^+ + 3.9$, which is different from a standard log law. Almost concurrently, Huser and Biringen investigated the fully developed turbulent flow in a square duct at a Reynolds number at $Re_b = 10320$ [34]. They showed the distribution of the normalized mean velocity along the wall bisector depends on how the mean velocity is normalized, using either local friction velocity or mean friction velocity. The streamwise mean velocity using local friction velocity is found to exceed the standard logarithmic law, which is interpreted as the result of slightly stronger turbulence production near the duct corners compared to a channel or a boundary-layer flow. However, they found the mean velocity computed by Gavrilakis, normalized by local friction velocity, shows a closer fit with the classic log law. This is due to the higher local friction velocity compared with the mean friction velocity for that specific case. Other numerical studies can be found in [39, 101] as well as [87, 69, 27, 100], with a focus on heat transfer in square ducts; [99, 98] on square annular ducts and [46, 12] on

Table 5.1: Overview of some of previous studies on duct flows

Researcher	Re_B	Re_τ	Method	$\frac{U_{CL}}{U_b}$	$\frac{u_\tau}{U_b}$	$\frac{\tau_w}{\bar{\tau}_w}$
Gavrilakis (1992)	4410	300	DNS	1.33	0.068	1.17
Huser & Biringen (1993)	10320	600	DNS	/	0.058	1.13
Lund (1977)	25000	/	Exp.	1.24	0.055	/
Leutheusser (1963)	34000	/	Exp.	/	/	1.0
Lund (1977)	50000	/	Exp.	1.20	0.050	1.015
Knight (1984)	65000	/	Exp.	/	/	1.0
Fujita (1986)	65000	/	Exp.	/	/	1.03
Brundrett & Baines (1964)	83000	3860	Exp.	1.2	0.047	/
Lund (1977)	125000	/	Exp.	1.17	0.046	1.02
Lauder & Ying (1972)	210000	/	Exp.	1.19	0.043	/
Lund (1977)	250000	/	Exp.	1.18	0.043	1.02
Gessner (1979)	250000	10550	Exp.	1.15	0.04	/

square-sectioned U-bends. A list of some of past studies on duct flows, both experimental and numerical, are listed in Table 1. The U_{CL} , U_b and u_τ are main centerline velocity, bulk velocity and friction velocity; while u_τ , τ_w and $\bar{\tau}_w$ represent mean friction velocity, local wall shear stress and mean wall shear stress respectively.

As previously mentioned, mean friction velocity will decrease as Reynolds number increases. Jones [38] proposed the following empirical relationship for square duct flows which relates the Reynolds number based on bulk velocity and the friction factor

$$\frac{1}{\sqrt{f}} = 2 \log \left(1.125 Re_b \sqrt{f} \right) - 0.8, \quad (5.1)$$

where the friction factor f is defined as $f = 8u_\tau^2/U_b^2$.

The ratio of local wall shear stress at the wall bisector to the mean wall shear stress $\tau_w/\bar{\tau}_w$ in square duct flows depends on Reynolds number as well, as evidenced by both experimental and numerical studies. The ratio for low and moderate Reynolds number tends to be higher. As shown in Table 1, the ratio

is around 1.1, for $Re_b = 4410$ and $Re_b = 10320$. As the Reynolds number increases, the ratio is closer to unity [49, 41, 51]. Therefore, the aforementioned discrepancy which appears due to the way how the mean velocity at the wall bisector is normalized (local friction velocity versus mean friction velocity) will disappear, since as the Reynolds number increases, the two friction velocities will match.

However, most of the numerical studies for square duct flows are limited to low Reynolds numbers, in contrast with the very few studies on duct flows at high Reynolds numbers. This study aims to identify a pragmatic wall-modeled LES approach for duct flows at high Reynolds numbers, to obtain improved time statistics. More specific physical details such as mechanism of second motions are not the within the scope of this study.

5.2 Methodology and numerical setup

In this section, the wall-modeled LES is conducted using both the classic wall-stress model and the new self-adaptive model. Gessner's experimental data [22] will be used as a primary reference. This section is structured as follows. First, the experimental data is analyzed and a modified log law is proposed for square duct flows at high Reynolds numbers. Next, five cases are set up in combination with the classic wall-stress model, using either the conventional Smagorinsky model or the self-adaptive model. Finally, the implementation of the self-adaptive model in the context of square ducts are presented.

Here the validity of classical log law is examined in square duct flows. In Fig. 5.1, the normalized experimental mean velocities along the wall bisector at Reynolds numbers 83000 [7] and 250000 [22] are shown together with the theoretical velocity profiles calculated from classical log law and the modified log law which is proposed to replace the classical log law as a better representation of the mean velocity field in square ducts. It takes the following form

$$U = \bar{u}_\tau (2.8 \ln y^+ + 4.35), \quad (5.2)$$

where \bar{u}_τ is the mean friction velocity, which is virtually the same as the local friction velocity u_τ for square duct flows at high Reynolds numbers, as has been already pointed out in the previous section. The modified log law obviously provide a better fit compared with the classical log law for both Reynolds numbers. Therefore, the current wall-stress model in combination with the classical log law is impractical and will cause considerable inaccuracies. The influence of the constants in the log law will be investigated later.

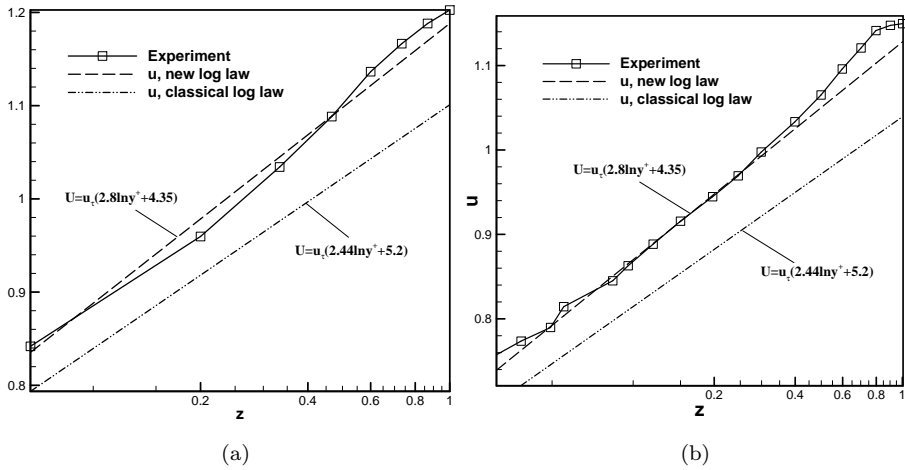


Figure 5.1: The experimental mean velocities along wall bisector, normalized using bulk velocity, at Reynolds numbers respectively (a) 83000 [7] and (b) 250000 [22]. The theoretical velocity profiles calculated from classical log law and modified log law are plotted as references.

The square duct flow of $Re_b = 250000$ is then investigated. The size of the computational domain is $4\pi \times 1 \times 1$, and an equidistant mesh of $128 \times 96 \times 96$ is employed. A total of 5 cases are setup and the details can be found in Table 2, where j_τ is the j -th point away from the wall, and corresponds to the position where the velocity components are taken as input for the wall-stress model, as defined in chapter 4. The case of $j_\tau = 4$ is only conducted for the conventional Smagorinsky model, since as have already shown in chapter 4, the value of j_τ does not have a noticeable impact on the results for the self-adaptive model.

Eq. (4.25) is employed to calculate the dynamic mixing length for the self-adaptive model. However, only one homogeneous direction (the streamwise direction) exists for the square duct flows, in contrast with two homogeneous directions for the channel flows. If the ensemble average which is represented by the brackets in Eq. (4.25) were to be replaced by the time filtering combined with spatial average along the streamwise direction, the simulation will suffer from numerical instabilities from the author's practice. Therefore, to overcome the numerical instabilities, additional local spatial average in the non-homogeneous and wall-parallel directions (parallel to the closest wall) is employed. The quantities in the brackets are average over the 13 neighboring points (centered around the point where the filtered/averaged quantities are calculated). More

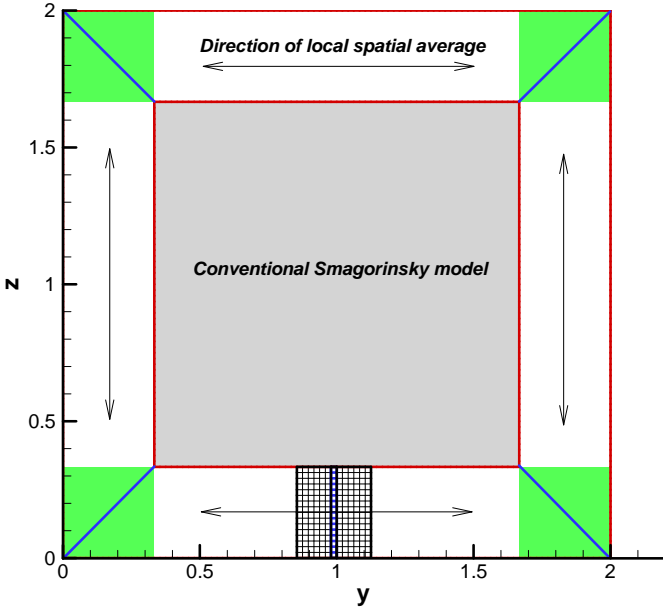


Figure 5.2: The numerical setup for the calculation of square duct flows using the self-adaptive model.

Table 5.2: Overview of square duct flow test cases of $Re_b = 250000$

Case	log law	j_τ	SGS model	Error of friction velocity \bar{u}_τ
1	classical	1	Smagorinsky model	10.2%
2	classical	1	self-adaptive model	9.1%
3	modified	1	Smagorinsky model	7.9%
4	modified	4	Smagorinsky model	6.25%
5	modified	1	self-adaptive model	2.2%

details can be found in Fig. 5.2. The self-adaptive model is used up to 30% of the half duct height away from the wall. The central grey area is where the conventional Smagorinsky model is applied. Near the corners, in the green area indicated in Fig. 5.2, the local average won't be justified due to the strong anisotropy. The dynamic mixing length is copied from the points just outside of the green area.

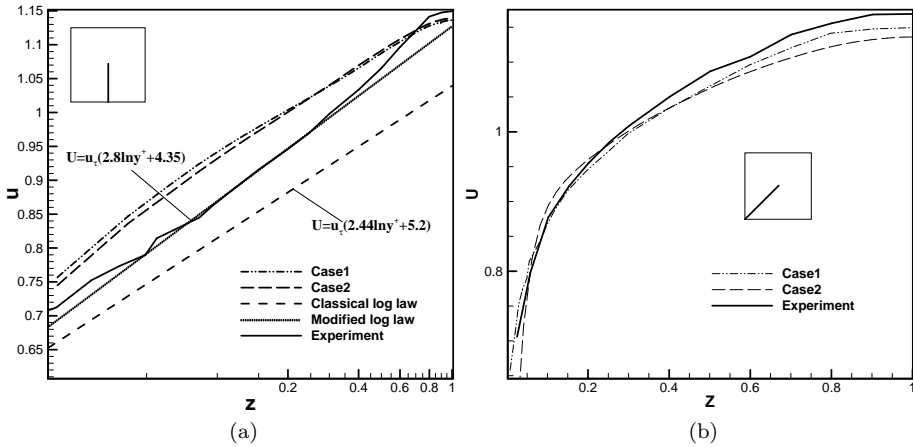


Figure 5.3: The predicted mean velocities based on the classical log law and normalized using bulk velocities, in comparison with experimental results [22] (a) along the wall bisector, and (b) along the corner bisector.

5.3 Results

The prediction errors of the friction velocity can be found in Table 2. The modified log law yields considerably better results than the classical log law, while the results of the self-adaptive model are better than those of the Smagorinsky model. The result of case 1 is inferior than that of case 4, where the value of j_τ is taken as 4 instead of 1; this is also in line with the results of the channel flow which are presented in section 4.5.

The predicted mean velocities along the wall bisector and corner bisector are shown in Fig. 5.3. The self-adaptive model yields better results than the conventional Smagorinsky model along the wall bisector, while the results along the corner bisector are not improved. The mean velocity contours, which are average over the four quadrants can be found in Fig. 5.4, with the red lines representing experimental mean velocity contours. The experimental velocity contours are distorted towards the corner, which means that the mean velocities are accelerated near the corner. This phenomenon is believed to be caused by the secondary flow [22]. The velocity contours predicted by the self-adaptive model matches the experimental results better than the Smagorinsky model where the distortion of the velocity contours are not captured at all.

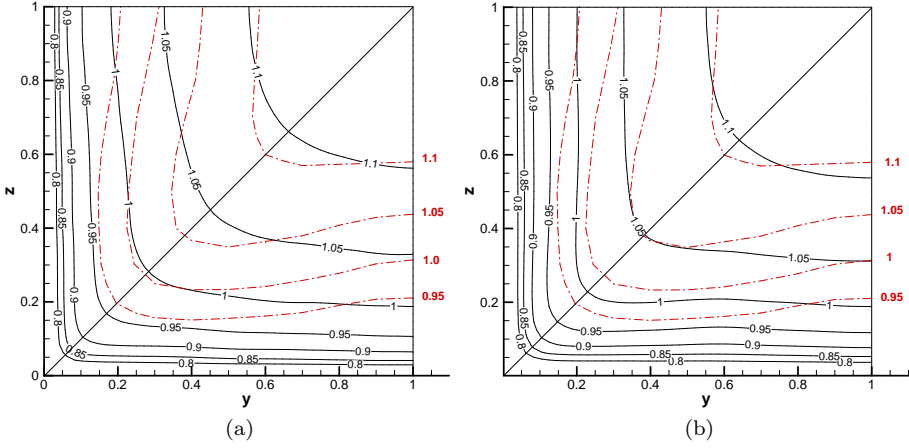


Figure 5.4: The predicted mean velocity contours based on the classical log law and normalized using bulk velocities, in comparison with experimental results (dash-dot lines) [22], using (a) Smagorinsky model, and (b) self-adaptive model.

The results obtained using the modified law, as shown in Eq. (5.2), can be found in Fig. 5.5 and Fig. 5.6. The self-adaptive model produced considerably better results along the wall bisector than those of the Smagorinsky model; however, the results along the corner bisector do not differ very much from each other. The value of j_τ , the position where the velocity components are taken as input for the wall-stress model, does not yield improved velocity profiles, except for the friction velocity, as already summarized in Table. 5.2. The velocity contours predicted using the self-adaptive model is once again superior than those of the Smagorinsky model. The velocity contours predicted using the conventional Smagorinsky model in combination with a $j_\tau = 4$ similar to those of the Smagorinsky model with a $j_\tau = 1$, and are not shown here.

The mean secondary velocity vectors predicted using the self-adaptive model in combination with the modified log-law are shown in Fig. 5.7(a), with the DNS results by Gavrilakis [18] as a reference. Two counter-rotating vortices are well captured and match the DNS results qualitatively. Though the secondary flows are very weak compared with the mean flow, they are responsible for momentum transfer towards that corner. The other models produce similar flow patterns to Fig. 5.7(a), thus are not presented here.

Finally the second-order turbulent statistics are shown in Fig. 5.8. The predicted statistics are in fair agreement with the experimental results, except near the wall,

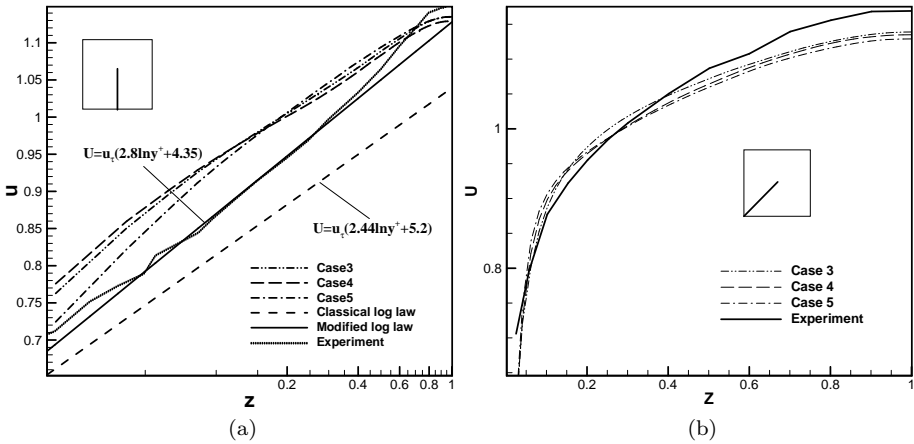


Figure 5.5: The predicted mean velocities based on the modified log law and normalized using bulk velocities, in comparison with experimental results [22] (a) along the wall bisector, and (b) along the corner bisector.

where large disparities are observed between predicted results and experiments. This is probably due to the coarse mesh resolution near the wall. On the other hand, the experimental resolution is very coarse near the wall as well, which makes it difficult to know the trends of the second-order statistics near the wall. It is also worthwhile to point out that the combination of the modified log law and the self-adaptive model, which yields improved friction velocities and mean flow profiles, tends to under-predicts the turbulent statistics. The other methodologies do not yields better results neither, as shown in Fig. 5.8(a), where under-predictions of $\langle v'v' \rangle$ and $-\langle u'v' \rangle$ can be observed. Another factor which may have great influence over the prediction of the turbulent statistics is the blending position, as is discussed in chapter 4 for the case of channel flow. This still remains an open question and further studies are needed to clarify this issue in the future.

5.4 Conclusion

Square duct flows at a Reynolds number of 250000 based on bulk velocity are simulated using wall-modeled LES in combination with the Smagorinsky model and the self-adaptive Smagorinsky model. A modified log law is proposed for

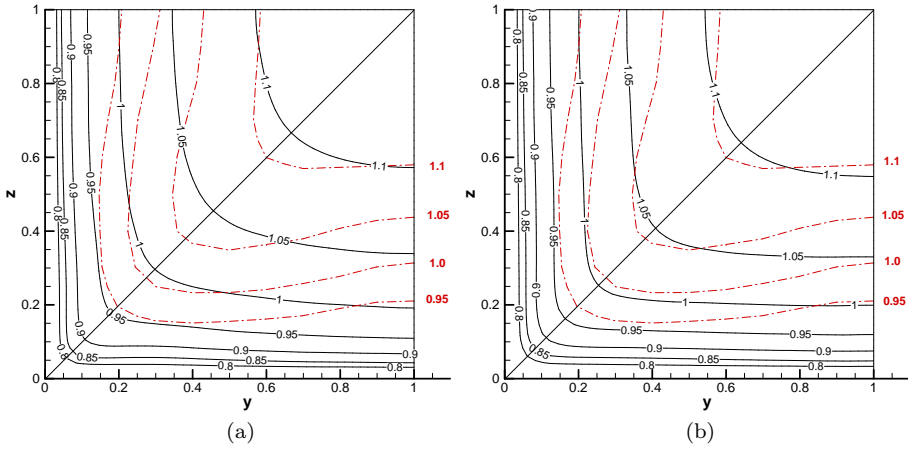


Figure 5.6: The predicted mean velocity contours based on the modified log law and normalized using bulk velocities, in comparison with experimental results (dash-dot lines) [22], using (a) Smagorinsky model, and (b) self-adaptive model.

square duct flows at high Reynolds numbers which provides a better fit with experimental results. The self-adaptive model leads to a smaller error on the prediction of friction velocity compared with the conventional Smagorinsky model; the modified law yields a more accurate prediction of the friction velocity for both the self-adaptive model and Smagorinsky model, in contrast with the classical log law.

The self-adaptive Smagorinsky model captured the acceleration of the mean velocity near the corners, while the conventional Smagorinsky model fails to capture this acceleration. The self-adaptive Smagorinsky model combined with the modified log law provides a more pragmatic and better means for the simulation of square duct flows at high Reynolds numbers compared with the conventional WSM.

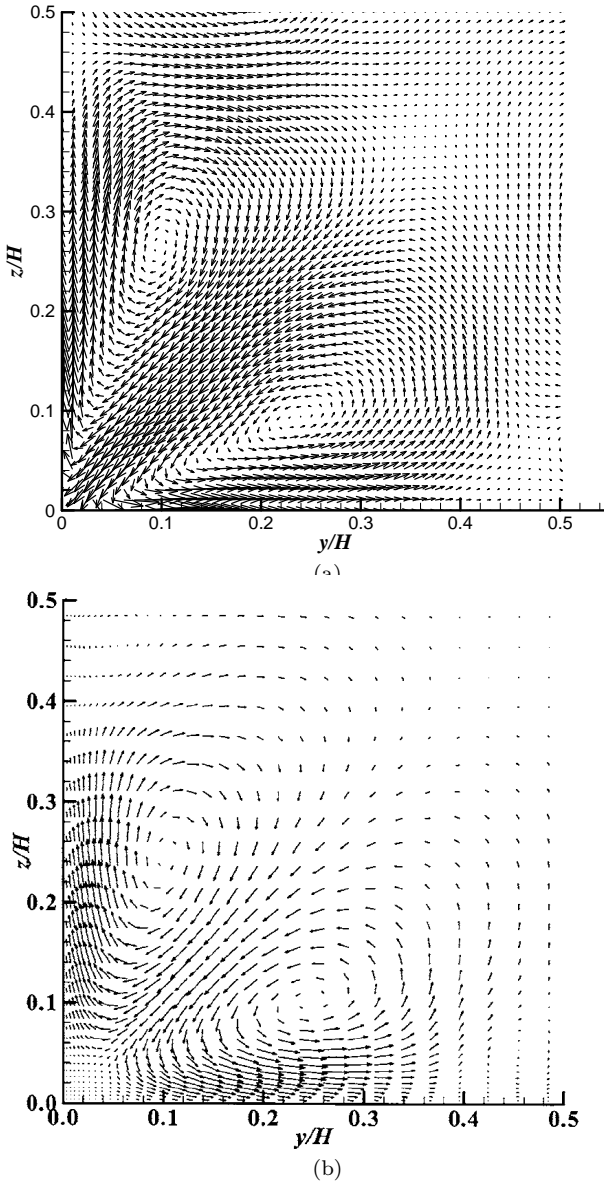


Figure 5.7: Mean secondary velocity vectors (a) obtained using the self-adaptive model in combination with the modified log law (b) the DNS results from Gavrilakis [18].

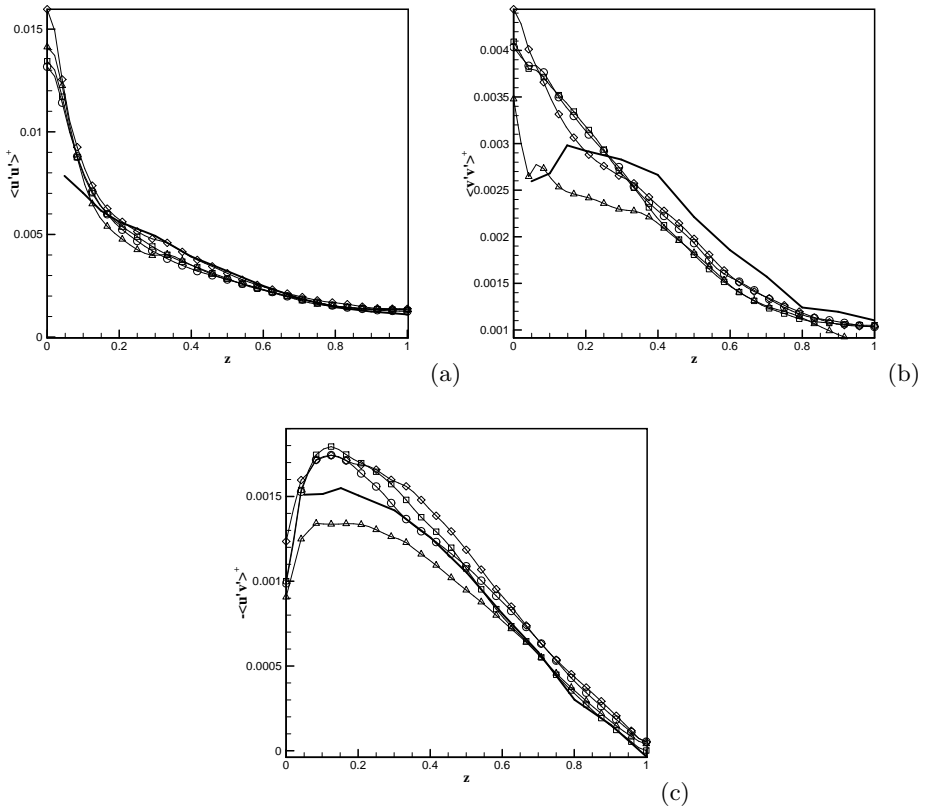


Figure 5.8: Reynolds stresses (a) $\langle u'u' \rangle$, (b) $\langle v'v' \rangle$, and (c) $-\langle u'v' \rangle$, from simulations obtained by: log law combined with Smagorinsky model (—□), modified log law combined with self-adaptive model (—◇), log law combined with Smagorinsky model (—○) and modified log law combined with self-adaptive model (—△). The experimental results are taken from reference [22], indicated by bold lines.

Chapter 6

Conclusion and suggestions for future research

6.1 Conclusion

Wall-modeled large eddy simulations for high Reynolds number wall-bounded flows is the major focus of this work.

To suppress the commonly encountered phenomenon of odd-even decoupling, explicit filtering is normally employed. However, the conventional filtering technique does not conserve the global momentum and mass flow rate, and in the worst scenario, alters the flow structure, as shown in [94]. This work builds on the principle of ‘conservative filtering’, which was firstly elaborated by Vreman [90]; and the high-order selective filters [3]. The boundary filters are constructed to match the selective filters at the internal points. Following Vreman’s work, the filter matrix is required to be symmetric to be conservative. In addition to that, a couple of constraints such as normalization, accuracy and the π -mode are imposed. Nine-, eleven-, and thirteen-point stencils, and associated one-sided boundary schemes, are then elaborated. The set of conservative filters are validated firstly over a channel flow test case, and then over a 2D cavity, to investigate the effect of filter formulations on noise prediction. The non-conservative boundary filters leads to large errors on the prediction of friction velocity; in contrast, the conservative filters has very little impact of the prediction of the friction velocity, irrespective of mesh resolution and filtering frequency. The non-conservative boundary filters fail to capture the dominant frequencies of the shear-layer mode and significantly change the flow structure

inside the cavity, while the conservative filters captures the dominant frequencies correctly without changing the flow structure.

The effect of the conservative filtering formulations in the formulation of the VMS model is studied and tested over a channel flow as well. The use of a conservative top-hat filter, was compared to a traditional top-hat implementation. The non-conservative formulations are found to lead to large errors, while the conservative filters again yield much small errors. This explicit filtering technique is applied after each physical time step and is independent of numerical schemes. The conservative filters developed in this study are mainly intended for structured grid with a mild grid stretching ratio, and not so straightforward for unstructured mesh.

The wall-stress model is employed in this study in combination with the Smagorinsky model to circumvent the excessive computational cost of wall-resolved LES. To solve the problem of log-layer mismatch which exists in conventional Smagorinsky model, starting from the equation for turbulent kinetic energy, a framework is setup in which the normalized mean shear and its budgets are explicitly linked. As a result of that, the contribution of each single term on the mean shear can be quantified. The analysis is extended to the case of wall-modeled LES. The budgets of the mean shear are studied over a rough-wall channel flow using the Smagorinsky model and the VMS model respectively. It is shown that over-dissipation does not necessarily leads over-prediction of the mean shear, which is the common perception before.

Based on this framework, a self-adaptive Smagorinsky model is proposed (neglecting viscous effect), in which the mixing length l_s is dynamically adjusted so that the desired logarithmic velocity distribution can be produced. In the case of RANS (the fluctuating variables will disappear), Prandtl's classical expression for the mixing length $l_s = \kappa y$ is recovered. The formulation of the self-adaptive model is then implemented in a second order in-house code FLOWAVE, taking into account the discretization errors. The model is validated and tested over the rough-wall channel flow at infinite Reynolds number. The desired logarithmic velocity distributions are obtained, and are independent of grid resolution and grid aspect ratio.

The self-adaptive model is then extended to include the viscous effect and applied to smooth-wall channel flows at $Re_\tau = 950$ and $Re_\tau = 2000$ respectively. Different factors which may influence the prediction such as the viscous effect, transport terms, the value of $\phi(y)$, j_τ and the Smagorinsky coefficient for the outer layer are investigated. The results of the self-adaptive model are found to be independent of the j_τ , the position where the velocity components are fed to the wall-stress model; the calibrated Smagorinsky coefficient according to Eq. (2.30) proves to produce better results than the Lilly Smagorinsky coefficient

0.17. The self-adaptive model yields overall better results than the conventional Smagorinsky model.

It should be noted, however, the self-adaptive model is mainly designed for high-Reynold-number attached wall flows. The extension to other types of attached flows is possible, for instance, attached wall flows with pressure gradients. In this case the pressure term should be included. The extension of the model to flow regimes with mass separation is impractical, since the log-law and local equilibrium, which are the preconditions for current model, will not be justified in this case.

In the last part of this work, the wall-modeled large eddy simulations are conducted for a square duct. A modified log law is proposed, which provides a better fit with the experimental results compared with the classic log law. The modified log law leads to smaller errors on the prediction of skin friction for both the conventional Smagorinsky model and the self-adaptive Smagorinsky model, while the self-adaptive Smagorinsky model yields more accurate friction velocity. In addition, the self-adaptive Smagorinsky model captures the acceleration of the mean streamwise velocity near the corners, which the conventional Smagorinsky model fails to predict.

6.2 Suggestions for future research

The conservative filtering could be extended to numerical method where both explicit filtering and hard boundary are involved such as the immersed boundary technique.

A major part of this thesis is dedicated to improving the wall-modeled LES for high Reynolds number wall bounded flows. Focus has been centered around the development and validation of a framework in which the ‘log-layer mismatch’ problem can be analyzed and a self-adaptive Smagorinsky model.

First, the influence of the blending position over the prediction of the mean flow and turbulent statistics in the square duct need to be investigated, following the same way as indicated in chapter 4 for the case of channel.

Secondly as a successful breakthrough, the self-adaptive model opens up new possibilities for further studies and improvements as well. Thus it is highly valuable to conduct further extensions to this approach and handle more practical problems.

The model can be extended to allow for more general combination of the wall model and internal model. This combination may provide two constraints for

kinetic energy, allowing for not only more general combination of the wall model and internal model (SGS model), but also better control of the discretization error at the first point. A hybrid methodology can be proposed, based on the balance for mean-flow kinetic energy in addition to the balance for turbulent kinetic energy, allowing for a more general combination of the wall model and internal model.

Further development of the methodology for different types of flow gradient different parallel flows could be carried out. Instead of presuming log layer, other profiles can be presumed and for instance applied to inlet BC or high-Reynolds number developing boundary layers. The model may be used to simulate the turbulent boundary layers, adaption of the model is necessitated considering the spatially evolving nature of turbulent boundary layers. At the same time, the model will be alternatively used to prescribe desired inlet BC. The turbulent boundary layer flow can be used as a test case.

Finally, as an application of the wall LES to CAA, it would be interesting to conduct wall-model large-eddy simulation of a square muffler at high Reynolds number, employing the expertise gained in this thesis, in terms of the conservative filters, the new self-adaptive model and proper use of the WSM in a square duct. The Reynolds number based on the height of the inlet duct and mean center-line velocity in the duct is approximately 168400. The computational cost for wall-resolved large-eddy simulation in this case will be prohibitive; therefore, a pragmatic way can be adopted: the walls of inlet duct and tail duct are modeled, given the fact that the flows in the ducts are attached; on the other hand, the expansion chamber could be fully resolved, considering the strong secondary flows and the fact that the local Reynolds number is likely to be much lower than that in the ducts.

The VMS model is superior to the Smagorinsky model and does not need the explicit damping to reduce the dissipation near the wall. It can be employed in the expansion chamber. In the duct, either the conventional Smagorinsky model or the self-adaptive model will be used. The practice established in chapter 5 can be used a guideline when setting up the wall-modeled LES in the inlet and tail duct: the modified log law will replace the classical log law, and value of j_τ will be set as a value of 4 to minimize the error on the prediction of the skin friction.

To conclude, there could be many interesting research tracks starting from this work, and I sincerely hope this work is sound basis for continued research on the wall-modeled LES for high-Reynolds number wall flows.

Appendix A

Coefficients of conservative boundary filters

j	1	2	3
g_0	0.24352749312000	0.23481047976170	0.19089951150600
g_1	-0.20478888064000	-0.19925013128581	-0.17150383223600
g_2	0.12000759168000	0.12019831024519	0.12363289179700
g_3	-0.04521111936000	-0.04930377563602	-0.06997542910500
g_4	0.00822866176000	0.01239644987396	0.02966275473600
g_5		-0.00144609307817	-0.00852073865900
g_6			0.00125459771400

Table A.1: The 9-point [3], 11-point [2] and 13-point [3] spatial filters for internal points, $g_{-j} = g_j$

j	1	2	3	4
$b_{1,j}$	0.04197486592000	-0.09624620416000	0.07479647232000	-0.02875379584000
$b_{2,j}$	-0.09624620416000	0.24676374656000	-0.23354267648000	0.12000759168000
$b_{3,j}$	0.07479647232000	-0.23354267648000	0.29696727424000	-0.22124620416000
$b_{4,j}$	-0.02875379584000	0.12000759168000	-0.22124620416000	0.25175615488000
g_{5-j}	0.00822866176000	-0.04521111936000	0.12000759168000	-0.20478888064000
g_{6-j}		0.00822866176000	-0.04521111936000	0.12000759168000
g_{7-j}			0.00822866176000	-0.04521111936000
g_{8-j}				0.00822866176000

Table A.2: The coefficients of the 9-point matching conservative boundary filters

j	1	2	3
$b_{1,j}$	0.04170901551687	-0.09759693795557	0.07523281384367
$b_{2,j}$	-0.09759693795557	0.24818961219352	-0.22954537948657
$b_{3,j}$	0.07523281384367	-0.22954537948657	0.28928023988085
$b_{4,j}$	-0.02595696896626	0.11441393793252	-0.21970475179924
$b_{5,j}$	0.00805817063946	-0.04641158947969	0.12309049640152
g_{6-j}	-0.00144609307817	0.01239644987396	-0.04930377563602
g_{7-j}		-0.00144609307817	0.01239644987396
g_{8-j}			-0.00144609307817
g_{9-j}			
g_{10-j}			

j	4	5
$b_{1,j}$	-0.02595696896626	0.00805817063946
$b_{2,j}$	0.11441393793252	-0.04641158947969
$b_{3,j}$	-0.21970475179924	0.12309049640152
$b_{4,j}$	0.25299130194833	-0.20358841052031
$b_{5,j}$	-0.20358841052031	0.23625657283987
g_{6-j}	0.12019831024519	-0.19925013128581
g_{7-j}	-0.04930377563602	0.12019831024519
g_{8-j}	0.01239644987396	-0.04930377563602
g_{9-j}	-0.00144609307817	0.01239644987396
g_{10-j}		-0.00144609307817

Table A.3: The coefficients of the 11-point matching conservative boundary filters

j	1	2	3
$b_{1,j}$	0.04031416306317	-0.09321174458200	0.07147004890233
$b_{2,j}$	-0.09321174458200	0.23345995106884	-0.21306138057267
$b_{3,j}$	0.07147004890233	-0.21306138057267	0.26254508756000
$b_{4,j}$	-0.02692028815167	0.11279882665300	-0.20571121271533
$b_{5,j}$	0.01196119032050	-0.06020613618633	0.13506751108767
$b_{6,j}$	-0.00486796726633	0.02748662456417	-0.07270666805300
g_{7-j}	0.00125459771400	-0.00852073865900	0.02966275473600
g_{8-j}		0.00125459771400	-0.00852073865900
g_{9-j}			0.00125459771400
g_{10-j}			
g_{11-j}			
g_{12-j}			
j	4	5	6
$b_{1,j}$	-0.02692028815167	0.01196119032050	-0.00486796726633
$b_{2,j}$	0.11279882665300	-0.06020613618633	0.02748662456417
$b_{3,j}$	-0.20571121271533	0.13506751108767	-0.07270666805300
$b_{4,j}$	0.22910917945267	-0.18887233136900	0.12717464144433
$b_{5,j}$	-0.18887233136900	0.19842105434483	-0.17242536468067
$b_{6,j}$	0.12717464144433	-0.17242536468067	0.19078848974450
g_{7-j}	-0.06997542910500	0.12363289179700	-0.17150383223600
g_{8-j}	0.02966275473600	-0.06997542910500	0.12363289179700
g_{9-j}	-0.00852073865900	0.02966275473600	-0.06997542910500
g_{10-j}	0.00125459771400	-0.00852073865900	0.02966275473600
g_{11-j}		0.00125459771400	-0.00852073865900
g_{12-j}			0.00125459771400

Table A.4: The coefficients of the 13-point matching conservative boundary filters

Bibliography

- [1] BALARAS, E., BENOCCI, C., AND PIOMELLI, U. Two-layer approximate boundary conditions for large-eddy simulations. *AIAA journal* 34, 6 (1996), 1111–1119.
- [2] BERLAND, J., BOGEY, C., MARSDEN, O., AND BAILLY, C. High-order, low dispersive and low dissipative explicit schemes for multiple-scale and boundary problems. *Journal of Computational Physics* 224, 2 (2007), 637–662.
- [3] BOGEY, C., AND BAILLY, C. A family of low dispersive and low dissipative explicit schemes for flow and noise computations. *Journal of Computational Physics* 194, 1 (2004), 194–214.
- [4] BOU-ZEID, E., MENEVEAU, C., AND PARLANGE, M. A scale-dependent Lagrangian dynamic model for large eddy simulation of complex turbulent flows. *Physics of Fluids* 17 (2005), 025105.
- [5] BRASSEUR, J., AND WEI, T. Designing large-eddy simulation of the turbulent boundary layer to capture law-of-the-wall scaling. *Physics of Fluids* 22 (2010), 021303.
- [6] BREUER, M., JAFFRÉZIC, B., AND ARORA, K. Hybrid les-rans technique based on a one-equation near-wall model. *Theoretical and Computational Fluid Dynamics* 22, 3 (2008), 157–187.
- [7] BRUNDRETT, E., AND BAINES, W. The production and diffusion of vorticity in duct flow. *Journal of Fluid Mechanics* 19, 03 (1964), 375–394.
- [8] CABOT, W. Large-eddy simulations with wall models. *Annual Research Briefs, Center for Turbulence Research, Stanford University* (1995), 41–50.
- [9] CABOT, W. Near-wall models in large-eddy simulations of flow behind a backward-facing step. *Annual Research Briefs, Center for Turbulence Research, Stanford University* (1996), 199–210.

- [10] CABOT, W., AND MOIN, P. Approximate wall boundary conditions in the large-eddy simulation of high Reynolds number flow. *Flow, Turbulence and Combustion* 63 (1999), 269–291.
- [11] CHAPMAN, D. Computational Aerodynamics Development and Outlook. *AIAA journal* 17 (1979), 1293–1313.
- [12] CHOI, Y., IACOVIDES, H., AND LAUNDER, B. Numerical computation of turbulent flow in a square-sectioned 180 deg bend. *TRANS. JSME J. FLUIDS ENG.* 111, 1 (1989), 59–68.
- [13] COCLE, R., BRICTEUX, L., AND WINCKELMANS, G. Scale dependence and asymptotic very high reynolds number spectral behavior of multiscale subgrid models. *Physics of Fluids* 21 (2009), 085101.
- [14] COLONIUS, T., LELE, S., AND MOIN, P. Boundary conditions for direct computation of aerodynamic sound generation. In *14th DGLR/AIAA Aeroacoustics Conference* (1992), vol. 1, pp. 438–447.
- [15] DE ROECK, W. *Hybrid methodologies for the computational aeroacoustics analysis of confined subsonic flows*. PhD thesis, University of Leuven, 2007.
- [16] DEMUREN, A., AND RODI, W. Calculation of turbulence-driven secondary motion in non-circular ducts. *Journal of Fluid Mechanics* 140, 1 (1984), 189–222.
- [17] FERZIGER, J., AND PERIĆ, M. *Computational methods for fluid dynamics*, vol. 3. Springer Berlin etc, 1999.
- [18] GAVRILAKIS, S. Numerical simulation of low-reynolds-number turbulent flow through a straight square duct. *Journal of Fluid Mechanics* 244, 1 (1992), 101–129.
- [19] GERMANO, M., PIOMELLI, U., MOIN, P., AND CABOT, W. A dynamic subgrid-scale eddy viscosity model. *Physics of Fluids A: Fluid Dynamics* 3 (1991), 1760.
- [20] GESSNER, F. The origin of secondary flow in turbulent flow along a corner. *Journal of Fluid Mechanics* 58, 01 (1973), 1–25.
- [21] GESSNER, F., AND EMERY, A. The numerical prediction of developing turbulent flow in rectangular ducts. *Journal of Fluids Engineering* 103 (1981), 445.
- [22] GESSNER, F., PO, J., AND EMERY, A. Measurements of developing turbulent flow in a square duct. In *Symposium on Turbulent Shear Flows, University Park, Pa* (1977), p. 9.

- [23] GHARIB, M., AND ROSHKO, A. The effect of flow oscillations on cavity drag. *Journal of Fluid Mechanics* 177, 10 (1987), 510–530.
- [24] GLOERFELT, X., BAILLY, C., AND JUVÉ, D. Calcul direct du rayonnement acoustique d'un écoulement affleurant une cavité. *Comptes Rendus de l'Acad mie des Sciences-Series IIB-Mechanics* 328, 8 (2000), 625–631.
- [25] GLOERFELT, X., AND JUVÉ, D. *Bruit rayonné par un écoulement affleurant une cavité: Simulation aéroacoustique directe et application de méthodes intégrales*. PhD thesis, Ecole Centrale de Lyon, 2001.
- [26] HAMBA, F. Log-layer mismatch and commutation error in hybrid rans/les simulation of channel flow. *International Journal of Heat and Fluid Flow* 30, 1 (2009), 20–31.
- [27] HÉBRARD, J., MÉTAIS, O., AND SALINAS-VASQUEZ, M. Large-eddy simulation of turbulent duct flow: heating and curvature effects. *International journal of heat and fluid flow* 25, 4 (2004), 569–580.
- [28] HIRSCH, C. *Numerical computation of internal and external flows: fundamentals of computational fluid dynamics*, vol. 1. Butterworth-Heinemann, 2007.
- [29] HOYAS, S., AND JIMÉNEZ, J. Scaling of the velocity fluctuations in turbulent channels up to $re=2003$. *Physics of fluids* 18 (2006), 011702.
- [30] HOYAS, S., AND JIMÉNEZ, J. Reynolds number effects on the Reynolds-stress budgets in turbulent channels. *Physics of Fluids* 20 (2008), 101511.
- [31] HUGHES, T., MAZZEI, L., AND JANSEN, K. Large eddy simulation and the variational multiscale method. *Computing and Visualization in Science* 3, 1 (2000), 47–59.
- [32] HUGHES, T., MAZZEI, L., OBERAI, A., AND WRAY, A. The multiscale formulation of large eddy simulation: Decay of homogeneous isotropic turbulence. *Physics of fluids* 13 (2001), 505.
- [33] HUGHES, T., OBERAI, A., AND MAZZEI, L. Large eddy simulation of turbulent channel flows by the variational multiscale method. *Physics of fluids* 13 (2001), 1784.
- [34] HUSERT, A., AND BIRINGEN, S. Direct numerical simulation of turbulent flow in. *J. Fluid Mech* 257 (1993), 65–95.
- [35] IWAMOTO, K., SUZUKI, Y., AND KASAGI, N. Reynolds number effect on wall turbulence: toward effective feedback control. *International journal of heat and fluid flow* 23, 5 (2002), 678–689.

- [36] JAMESON, A., SCHMIDT, W., TURKEL, E., ET AL. Numerical solutions of the euler equations by finite volume methods using runge-kutta time-stepping schemes. *AIAA paper 81*, -125 (1981), 9.
- [37] JEANMART, H., AND WINCKELMANS, G. Investigation of eddy-viscosity models modified using discrete filters: A simplified" regularized variational multiscale model" and an" enhanced field model". *Physics of Fluids 19*, 5 (2007), 55110–56100.
- [38] JONES JR, O. An improvement in the calculation of turbulent friction in rectangular ducts. *Journal of Fluids Engineering 98* (1976), 173.
- [39] JOUNG, Y., CHOI, S., AND CHOI, J. Direct numerical simulation of turbulent flow in a square duct: analysis of secondary flows. *Journal of engineering mechanics 133* (2007), 213.
- [40] KAWAI, S., AND LARSSON, J. Wall-modeling in large eddy simulation: Length scales, grid resolution, and accuracy. *Physics of Fluids 24*, 1 (2012), 015105–015105.
- [41] KNIGHT, D., HAMED, M., ET AL. Boundary shear in smooth rectangular channels. *Journal of hydraulic engineering 110* (1984), 405.
- [42] KNIGHT, D., AND PATEL, H. Boundary shear in smooth rectangular ducts. *Journal of Hydraulic Engineering 111*, 1 (1985), 29–47.
- [43] LARCHEVÊQUE, L., SAGAUT, P., AND LABBÉ, O. Large-eddy simulation of a subsonic cavity flow including asymmetric three-dimensional effects. *Journal of Fluid Mechanics 577*, 1 (2007), 105–126.
- [44] LARCHEVÊQUE, L., SAGAUT, P., LE, T., AND COMTE, P. Large-eddy simulation of a compressible flow in a three-dimensional open cavity at high reynolds number. *Journal of Fluid Mechanics 516* (2004), 265–301.
- [45] LARCHEVÊQUE, L., SAGAUT, P., MARY, I., LABBÉ, O., AND COMTE, P. Large-eddy simulation of a compressible flow past a deep cavity. *Physics of fluids 15* (2003), 193.
- [46] LAUNDER, B., LOIZOU, P., AND ZHAO, H. Turbulent boundary-layer development around a square-sectioned u-bend: measurements and computation. *Journal of fluids engineering 112* (1990), 409.
- [47] LAUNDER, B., AND YING, W. Secondary flows in ducts of square cross-section. *J. Fluid Mech 54*, part 2 (1972), 289–295.
- [48] LELE, S. Compact finite difference schemes with spectral-like resolution. *Journal of Computational Physics 103*, 1 (1992), 16–42.

- [49] LEUTHEUSSER, H. Turbulent flow in rectangular ducts. *J. Hydraulics Div., Proc. ASCE* 89 (1963), 1–19.
- [50] LILLY, D. K. The representation of small-scale turbulence in numerical simulation experiments. In *Proceedings of IBM Scientific Computing Symposium on Environmental Sciences* (1967), IBM Data Processing Division, White Plains, New York.
- [51] LUND, E. Mean flow and turbulence characteristics in the near corner region of a square duct. Master’s thesis, University of Washington, 1977.
- [52] MARSDEN, O., BOGEY, C., AND BAILLY, C. High-order curvilinear simulations of flows around non-cartesian bodies. *Journal of Computational Acoustics* 13, 4 (2005), 731–748.
- [53] MARUSIC, I., MCKEON, B. J., MONKEWITZ, P. A., NAGIB, H. M., SMITS, A. J., AND SREENIVASAN, K. R. Wall-bounded turbulent flows at high reynolds numbers: Recent advances and key issues. *Physics of Fluids* 22 (2010), 065103.
- [54] MASON, P., AND THOMSON, D. Stochastic backscatter in large-eddy simulations of boundary layers. *Journal of Fluid Mechanics* 242, 1 (1992), 51–78.
- [55] MELDI, M., LUCOR, D., AND SAGAUT, P. Is the smagorinsky coefficient sensitive to uncertainty in the form of the energy spectrum? *Physics of Fluids* 23, 12 (2011), 125109.
- [56] MEYERS, J. Error-landscape assessment of large-eddy simulations: a review of the methodology. *Journal of Scientific Computing* 49 (2011), 65–77.
- [57] MEYERS, J., GEURTS, B., AND SAGAUT, P. A computational error-assessment of central finite-volume discretizations in large-eddy simulation using a smagorinsky model. *Journal of Computational Physics* 227, 1 (2007), 156–173.
- [58] MEYERS, J., MENEVEAU, C., AND GEURTS, B. J. Error-landscape-based multi-objective calibration of the smagorinsky eddy-viscosity using high-reynolds-number decaying turbulence data. *Physics of Fluids* 22 (2010), 125106.
- [59] MEYERS, J., AND SAGAUT, P. On the model coefficients for the standard and the variational multi-scale Smagorinsky model. *Journal of Fluid Mechanics* 569 (2006), 287–319.

- [60] MEYERS, J., AND SAGAUT, P. Evaluation of smagorinsky variants in large-eddy simulations of wall-resolved plane channel flows. *Physics of Fluids* 19, 9 (2007), 95105–95105.
- [61] MOENG, C.-H. A large-eddy simulation model for the study of planetary boundary-layer turbulence. *J. Atmos. Sci.* 6 (1984), 2311.
- [62] NIKITIN, N., NICOUD, F., WASISTHO, B., SQUIRES, K., AND SPALART, P. An approach to wall modeling in large-eddy simulations. *Physics of Fluids* 12 (2000), 1629.
- [63] PIOMELLI, U. Wall-layer models for large-eddy simulations. *Progress in aerospace sciences* 44, 6 (2008), 437–446.
- [64] PIOMELLI, U., BALARAS, E., PASINATO, H., SQUIRES, K., AND SPALART, P. The inner–outer layer interface in large-eddy simulations with wall-layer models. *International Journal of heat and fluid flow* 24, 4 (2003), 538–550.
- [65] PIOMELLI, U., AND E., B. Wall-layer models for large-eddy simulations. *Annual Review of Fluid Mechanics* 34, 6 (2002), 349–374.
- [66] PIQUET, J. *Turbulent flows: models and physics*. Springer, 1999.
- [67] POPE, S. *Turbulent flows*. Cambridge Univ Pr, 2000.
- [68] PORTÉ-AGEL, F., MENEVEAU, C., AND PARLANGE, M. A scale-dependent dynamic model for large-eddy simulation: application to a neutral atmospheric boundary layer. *Journal of Fluid Mechanics* 415 (2000), 261–284.
- [69] QIN, Z., AND PLETCHER, R. Large eddy simulation of turbulent heat transfer in a square duct. In *Proceedings of 2004 ASME International Mechanical Engineering Congress and RD&D Expo, Anaheim, USA* (2004).
- [70] RADHAKRISHNAN, S., PIOMELLI, U., KEATING, A., AND LOPES, A. Reynolds-averaged and large-eddy simulations of turbulent non-equilibrium flows. *Journal of Turbulence*, 7 (2006).
- [71] ROSSITER, J. Wind tunnel experiments on the flow over rectangular cavities at subsonic and transonic speeds. royal aircraft establishment. Tech. rep., TR, 1964.
- [72] ROWLEY, C. *Modeling, simulation, and control of cavity flow oscillations*. PhD thesis, California Institute of Technology, 2002.

- [73] RUBIO, G. *Numerical methodologies for the determination of noise sources in subsonic flows*. PhD thesis, University of Leuven, 2007.
- [74] SAGAUT, P. *Large eddy simulation for incompressible flows: an introduction*. Springer Verlag, 2006.
- [75] SHIEH, C., AND MORRIS, P. Parallel computational aeroacoustic simulation of turbulent subsonic cavity flow. *AIAA paper 1914* (2000).
- [76] SHIEH, C., AND MORRIS, P. Comparison of two-and three-dimensional turbulent cavity flows. *AIAA paper 511* (2001).
- [77] SPALART, P. R. Detached-eddy simulation. *Annual Review of Fluid Mechanics 41* (2009), 181–202.
- [78] SPALART, P. R., JOU, W.-H., STRELETS, M., AND ALLMARAS, S. R. Comments on the feasibility of LES for wings, and on a hybrid RANS/LES approach. In *Advances in DNS/LES* (1997), C. Liu and Z. Liu, Eds., Greyden Press, Columbus, OH, pp. 137–147.
- [79] STOLZ, S., SCHLATTER, P., AND KLEISER, L. High-pass filtered eddy-viscosity models for large-eddy simulations of transitional and turbulent flow. *Physics of Fluids 17* (2005), 065103.
- [80] TAKEDA, K., AND SHIEH, C. Cavity tones by computational aeroacoustics. *International Journal of Computational Fluid Dynamics 18*, 6 (2004), 439–454.
- [81] TAM, C., AND SHEN, H. Direct computation of nonlinear acoustic pulses using high order finite difference schemes. *AIAA paper 4325* (1993).
- [82] TAM, C., AND WEBB, J. Dispersion-relation-preserving finite difference schemes for computational acoustics. *Journal of computational physics 107*, 2 (1993), 262–281.
- [83] TAM, C., WEBB, J., AND DONG, Z. A study of the short wave components in computational acoustics. *Journal of Computational Acoustics 1*, 1 (1993), 1–30.
- [84] TEMPLETON, J. A., MEDIC, G., AND KALITZIN, G. An eddy-viscosity based near-wall treatment for coarse grid large-eddy simulation. *Physics of Fluids 17* (2005), 105101.
- [85] TEMPLETON, J. A., WANG, M., AND MOIN, P. An efficient wall model for large-eddy simulation based on optimal control theory. *Physics of Fluids 18* (2006), 025101.

- [86] VANELDEREN, B., DE ROECK, W., VANDEUN, D., MATTHEYS, Y., SAS, P., AND DESMET, W. Experimental study on the aeroacoustic characterization of exhaust mufflers in the presence of mean flow. In *Proceedings of ISMA2010 International Conference on Noise and Vibration Engineering including USD2010* (2010).
- [87] VÁZQUEZ, M., AND MÉTAIS, O. Large-eddy simulation of the turbulent flow through a heated square duct. *Journal of Fluid Mechanics* 453 (2002), 201–238.
- [88] VISBAL, M., AND GAITONDE, D. High-order-accurate methods for complex unsteady subsonic flows. *AIAA journal* 37, 10 (1999), 1231–1239.
- [89] VREMAN, A. The filtering analog of the variational multiscale method in large-eddy simulation. *Physics of Fluids* 15 (2003), L61.
- [90] VREMAN, A. The adjoint filter operator in large-eddy simulation of turbulent flow. *Physics of Fluids* 16 (2004), 2012.
- [91] VREMAN, B., GEURTS, B., AND KUERTEN, H. A priori tests of large eddy simulation of the compressible plane mixing layer. *Journal of engineering mathematics* 29, 4 (1995), 299–327.
- [92] WU, P. The prediction of complex turbulent flows in a compressor stage using cfd technique. Master’s thesis, Tsinghua University, 2006.
- [93] WU, P., AND MEYERS, J. On the construction of globally conservative high-pass filters for computational aeroacoustics. In *Proceedings of 17th International Congress on Sound and Vibration (ICSV17)* (2010).
- [94] WU, P., AND MEYERS, J. Globally conservative high-order filters for large-eddy simulation and computational aero-acoustics. *Computers & Fluids* 48 (2011), 150–162.
- [95] WU, P., AND MEYERS, J. A constraint for the subgrid-scale stresses in the logarithmic region of high reynolds number turbulent boundary layers: a solution to the log-layer mismatch problem. *Physics of Fluids under review* (2012).
- [96] WU, P., AND MEYERS, J. An improved blending formulation for wall-modeled large-eddy simulations. In *Progress in Hybrid RANS-LES Modelling* (2012), Springer, ISBN 978-3-642-31817-7.
- [97] WU, P., AND MEYERS, J. Wall-modeled large-eddy simulation of a square duct at high reynolds number. In *the 12th International Conference on Noise and Vibration Engineering (ISMA12)* (2012).

- [98] XU, H. Direct numerical simulation of turbulence in a square annular duct. *Journal of Fluid Mechanics* 621 (2010), 23.
- [99] XU, H., AND POLLARD, A. Large eddy simulation of turbulent flow in a square annular duct. *Physics of Fluids* 13 (2001), 3321.
- [100] YANG, H., CHEN, T., AND ZHU, Z. Numerical study of forced turbulent heat convection in a straight square duct. *International Journal of Heat and Mass Transfer* 52, 13-14 (2009), 3128–3136.
- [101] ZHU, Z., YANG, H., AND CHEN, T. Direct numerical simulation of turbulent flow in a straight square duct at reynolds number 600. *Journal of Hydrodynamics, Ser. B* 21, 5 (2009), 600–607.

Curriculum vitae

Peng Wu was born in Junan, Shandong province, China in 1982. He got his Bachelor's degree in Mechanical Engineering in 2003 from Beihang University (BUAA) in Beijing. Within the framework of his Bachelor, he worked as a intern at Chengdu Aircraft Industry Group (CAC) in Chengdu, China in August, 2002. He then moved to School of Aerospace, Tsinghua University and followed a research master's program in mechanics, with a topic of 'The prediction of complex turbulent flows in a compressor stage using CFD technique'. He was awarded the Takada Scholarship in 2004, 2005 and got his master's degree in 2006. In the last year of his master's study, he stayed at the Interdisciplinary Center for Scientific Computing (IWR) of Universität Heidelberg (Germany) for two months as a visiting student.

From August 2006 till December 2007, he worked at the Interdisciplinary Center for Scientific Computing (IWR) of Universität Heidelberg (Germany) as a research assistant. The research topic during this period is 'Modeling and simulation of spray process in turbulent two-phase flows'. He was awarded the DFG (German Science Foundation) fellowship under the International Graduiertenkolleg IGK 710 "Complex processes: Modeling, Simulation and Optimization".

In February 2008, he started his PhD at the Division of Applied Mechanics and Energy Conversion (TME) of the Mechanical Engineering Department at the KU Leuven. The PhD was supervised by Prof. dr. ir. Johan Meyers. From 2008 till 2010, he was involved in a FWO-project CAPRICORN - Simulation and design tools towards the reduction of aerodynamic noise in confined flows.

List of Publications

International peer reviewed journal articles

1. P. Wu, J. Meyers. A constraint for the subgrid-scale stresses in the logarithmic region of high Reynolds number turbulent boundary layers: a solution to the log-layer mismatch problem. *Physics of Fluids*, under review, 2012.
2. P. Wu, J. Meyers. Globally conservative high-order filters for large-eddy simulation and computational aero-acoustics. *Computers & Fluids*, 48(5):150-162, 2011.

Full papers in international conference proceedings

1. P. Wu, J. Meyers. Wall-modeled large-eddy simulation of a square duct at high Reynolds number, *the 12th International Conference on Noise and Vibration Engineering (ISMA12)*, Leuven, Belgium, 2012.
2. P. Wu, J. Meyers. An improved blending formulation for wall-modeled large-eddy simulations, *Progress in Hybrid RANS-LES Modelling (Editors: S. Fu, W. Haase, S.-H. Peng and D. Schwamborn)*, Springer, ISBN 978-3-642-31817-7, 111-120, 2012.
3. A. Onder, P. Wu, J. Meyers. Improving speed-up and efficiency in simulation of stationary turbulent flows by parallelization of statistical averaging, *Proceedings of the 9th international ERCOFTAC symposium on engineering turbulence modeling and measurements*, Thessaloniki, Greece, 2012.
4. P. Wu, J. Meyers. On the construction of globally conservative high-pass filters for computational aero-acoustics, *Proceedings of the 17th*

international congress on sound and vibration (ICSV17), Cairo, Egypt, 2010.

5. P. Wu, E. Gutheil. Modeling of turbulent spray flows using an improved model of droplet motion, *Proceedings of the 22nd ILASS Europe conference*, Como Lake, Italy, 2008.
6. P. Wu, Y.-X. Ren, D. Wisler, A. Wadia. The Prediction of the turbulent flows in a transonic compressor rotor using CFD technique, *Proceedings of the first international symposium on jet propulsion and power Engineering (1st ISJPPE)*, Kunming, China, 2006.

Abstracts in international conference proceedings

1. P. Wu, J. Meyers. A self-adaptive wall model for large eddy simulation of channel flow at moderate Reynolds numbers, *the 9th EuroMech Fluid Mechanics Conference (EFMC9)*, Rome, Italy, 2012.

Arenberg Doctoral School of Science, Engineering & Technology

Faculty of Engineering

Department of Mechanical Engineering

Fluids Group

Celestijnenlaan 300A box 2421

B-3001 Heverlee

KU LEUVEN

